

**A DISTRIBUTED MULTI-LEVEL CURRENT MODELING
METHOD FOR DESIGN ANALYSIS AND OPTIMIZATION OF
PERMANENT MAGNET ELECTROMECHANICAL ACTUATORS**

A Dissertation
Presented to
The Academic Faculty

by

Jungyoul Lim

In Partial Fulfillment
of the Requirements for the Degree
Doctor of Philosophy in the
School of Mechanical Engineering

Georgia Institute of Technology
August 2014

Copyright © Jungyoul Lim 2014

**A DISTRIBUTED MULTI-LEVEL CURRENT MODELING
METHOD FOR DESIGN ANALYSIS AND OPTIMIZATION OF
PERMANENT MAGNET ELECTROMECHANICAL ACTUATORS**

Approved by:

Dr. Kok-Meng Lee, Advisor
School of Mechanical Engineering
Georgia Institute of Technology

Dr. Yang Wang
School of Civil & Environmental
Engineering
Georgia Institute of Technology

Dr. Jun Ueda
School of Mechanical Engineering
Georgia Institute of Technology

Dr. Xinyan Deng
School of Mechanical Engineering
Purdue University

Dr. Yan Wang
School of Mechanical Engineering
Georgia Institute of Technology

Date Approved: [April 24, 2014]

To my parents;

Saehong Lim and Soonyang Park

ACKNOWLEDGEMENTS

I would like to express my sincere gratitude to my advisor, Dr. Kok-Meng Lee for his patience, insightful guidance, and constant encouragement. His enthusiasms to understand fundamentals and to realize new practical ideas have always motivated me, and provided an important basis for the successful completion of this research. I would also like to thank my thesis committee members Dr. Jun Ueda, Dr. Yan Wang, Dr. Yang Wang, and Dr. Xinyan Deng for their valuable advices and comments on this thesis.

I want to acknowledge the suggestions and help from the former and current colleagues in the AIMRL group. To Dr. Hungsun Son: I appreciate your guide on my school life and initial research. To Dr. Jiajie Guo, Dr. Kun Bai, Dr. Shaohui Foong, Yang Xie, Chun-Yeon Lin, Min Li: Sincerely thank you for all of ideas and assistances on this research. To Xianmin Chen: I appreciate your PM-LSynM experimental data. To Ying Chen, Jingjing Ji, Donghai Wang: Thank you for your valuable comments and assistances.

With many colleagues Dr. Sangil Lee, Dr. Myeongsub Kim, Dr. Yongjin Kim, Michael D. Kim, and Minseok Ha, my school life become more enjoyable. I want to thank them for all their help and advice.

Finally, I wish to give my special thanks to my parents Saehong Lim and Soonyang Park who have provided endless love and encouragement throughtout my life. It is also my pleasure thank my brother Jungsung Lim, and my sisters Euna Lim and Chukang Lim for their help and encouragement.

This research was supported in part by National Basic Research Program of China (973 Program, Grant No. 2013CB035803), by U. S. National Science Foundation under

grant number CMMI-0928095, and by the Georgia Agriculture Technological Research Program (ATRP).

TABLE OF CONTENTS

ACKNOWLEDGEMENTS	iv
LIST OF TABLES	x
LIST OF FIGURES	xi
NOMENCLATURE	xv
SUMMARY	xviii
CHAPTER 1 INTRODUCTION	1
1.1 BACKGROUND AND MOTIVATION	1
1.2 REVIEW OF PRIOR AND RELATED WORKS	3
1.2.1 Analytic and magnetic circuit methods	3
1.2.2 Numerical methods for electromagnetic actuators	4
1.2.3 Electromagnetic source based magnetic field model	5
1.2.4 M-DOF actuators and spherical motors	6
1.2.5 Optimization of electromagnetic actuators	8
1.3 PHILOSOPHY OF DISTRIBUTED MULTI-LEVEL CURRENT	10
1.4 RESEARCH OBJECTIVE.....	14
1.5 OUTLINE AND ORGANIZATION OF THESIS	16
CHAPTER 2 DISTRIBUTED CURRENT-BASED MAGNETIC FIELD MODEL	18
2.1 ELECTROMAGNETIC EQUATIONS FOR ACTUATORS	18
2.1.1 Electromagnetic sources	20
2.1.2 Governing equations of electromagnetic field.....	22
2.1.3 Magnetic force and torque equation	23

2.2	DISTRIBUTED MULTI-LEVEL CURRENT MODEL	23
2.2.1	Multi-level local source approximation	25
2.2.2	DMC force and torque equations	31
2.3	DMC MODEL FOR MAGNETIC MATERIALS	31
2.4	DMC MODEL FOR EDDY CURRENT FORMULATION	34
2.5	ILLUSTRATIVE EXAMPLES AND VALIDATION	35
2.5.1	Volume and surface elements	36
2.5.2	Cylindrical PM and EM	38
2.5.3	Iron plate and cylindrical PM	45
2.5.4	Eddy current induced by EMs	46
2.6	SUMMARY	48
CHAPTER 3 DMC BASED ACTUATOR LAYOUT OPTIMIZATION		50
3.1	OVERVIEW OF LAYOUT OPTIMIZATION	50
3.1.1	Topology optimization of a PM actuator	51
3.1.2	Linearization of topology optimization	53
3.1.3	Layout Optimization	57
3.2	LINEAR TOPOLOGY OPTIMIZATION	59
3.2.1	Surface current equations	60
3.2.2	Force and torque equations	62
3.2.3	Rotor iron equation	63
3.3	ILLUSTRATIVE EXAMPLES	65
3.3.1	Electric input current specification	66
3.3.2	1-DOF rotary motor	69

3.3.3	2-DOF orientation stage.....	73
3.4	SUMMARY	78
CHAPTER 4 ILLUSTRATIVE DESIGN OPTIMIZATION APPLICATIONS		80
4.1	SPHERICAL MOTOR.....	81
4.1.1	Optimization Parameters and Formulations.....	83
4.1.2	Layout Optimization results.....	88
4.1.3	Iron boundary and external loads.....	94
4.1.4	Weight efficiency.....	97
4.2	LINEAR-ROTARY MOTOR.....	100
4.2.1	1-DOF rotary and linear motor	101
4.2.2	Linear-rotary motor.....	106
4.3	DISK-SHAPED SYNCHRONOUS MOTOR (DSSM).....	112
4.3.1	Layout Optimization	115
4.3.2	Torque simulation of CAD model	119
4.4	SUMMARY	123
CHAPTER 5 EXPERIMENTAL VALIDATION.....		124
5.1	DISK-SHAPED SYNCHRONOUS MOTOR (DSSM).....	124
5.1.1	Experimental setup for measurement.....	126
5.1.2	Model validation with experimental results.....	130
5.2	PM SPHERICAL-MOTOR (PMSM) ORIENTATION STAGE	132
5.2.1	Analysis of PMSM orientation stage	133
5.2.2	Magnetic field of rotor PMs.....	134
5.2.3	WCR and EM torques.....	137

5.3	MAGNETIC WHEELS OF A FLEXIBLE MOBILE NODE (FMN)	139
5.3.1	Magnetic wheel design and torque experiment	139
5.3.2	Torque simulation and validation	140
5.4	PM LINEAR SYNCHRONOUS MOTOR (PM-LSynM)	144
5.4.1	Identification of PM magnetization	145
5.4.2	Identification of EM coil positions	149
5.5	SUMMARY	151
CHAPTER 6 CONCLUSIONS AND FUTURE WORKS.....		153
6.1	CONCLUSIONS.....	153
6.2	FUTURE WORKS	156
APPENDIX A: BC'S OF MAGNETIC MATERIALS.....		159
APPENDIX B: PM DESIGN VARIABLE		162
REFERENCES		164

LIST OF TABLES

Table 2-1	Computation time and error for the volume and surface elements	38
Table 2-2	Simulation parameters for the magnetic field validation	41
Table 2-3	Computation time and error for the PM and EM	42
Table 2-4	Simulation parameters for the force validation	43
Table 2-5	Computation time and error for the force validation	44
Table 2-6	Computation time for the iron plate and cylindrical PM.....	46
Table 4-1	Stator and rotor design space for spherical motor	82
Table 4-2	Optimization parameters for rotor design spaces	86
Table 4-3	Torque comparison of optimized designs.....	94
Table 4-4	Torque comparison of the optimized designs with an iron boundary	95
Table 4-5	Optimization parameters for DSSM.....	114
Table 4-6	Output torques of optimized LD.....	116
Table 4-7	Output torques of optimized SD.....	118
Table 4-8	DMC parameters to simulate the CAD of DSSM	120
Table 4-9	Output torques of CAD model of LD.....	121
Table 4-10	Output torques of CAD model of SD	122
Table 5-1	Simulation parameters for PMSM orientation stage	134
Table 5-2	PM Geometry and sensor positions measuring air gap flux density	146
Table 5-3	MSE on the flux density of identified PMs	149

LIST OF FIGURES

Figure 1-1	Schematic illustration of electromagnetic point sources.....	10
Figure 1-2	DMC local sources for magnetic field computation	12
Figure 1-3	Linear force in terms of electromagnetic sources	13
Figure 2-1	Electromagnetic sources.....	20
Figure 2-2	Schematic of a source element i	24
Figure 2-3	Magnetic field errors around the i^{th} source element.....	25
Figure 2-4	Recursively defined local sources and its octree representation	26
Figure 2-5	Modified scalar kernel functions at $l=li$	28
Figure 2-6	Recursive function to find active local sources.....	29
Figure 2-7	Magnetic material effects explained by DMC surface elements	32
Figure 2-8	Eddy current formulation using DMC volume elements	34
Figure 2-9	Geometry and parameters of volume and surface sources.....	36
Figure 2-10	Comparison computed results by different li and exact solution.....	37
Figure 2-11	Geometry of cylindrical PM and EM.....	39
Figure 2-12	Decomposed geometries of cylindrical PM and EM	40
Figure 2-13	Computed magnetic fields nearby the cylindrical PM.....	41
Figure 2-14	Computed magnetic fields nearby the cylindrical EM.....	42
Figure 2-15	Experimental setup and parameters	43
Figure 2-16	Computed force and experimental data of cylindrical EM and PM.....	44
Figure 2-17	Iron test setup and parameters.....	45
Figure 2-18	Force comparison between cylindrical PM and iron plate.....	46
Figure 2-19	Eddy current test setup and parameters.....	47
Figure 2-20	Simulated levitation height and measured data.....	48
Figure 3-1	EM input currents defined by PM pole patterns	54
Figure 3-2	Solution set with nonlinear and linear constraints	56
Figure 3-3	Flow chart of Layout Optimization.....	57
Figure 3-4	Force and torque on a rotor PM surface at the orientation θ_p	62
Figure 3-5	Iron boundary magnetized by a PM surface current	65

Figure 3-6	Flowchart of 3-DOF spherical motor optimization.....	66
Figure 3-7	EM input current specifications of 2D design examples	67
Figure 3-8	Optimization parameters for the 1-DOF rotary motor	69
Figure 3-9	Two cases of 2-phase inputs for the 1-DOF rotary motor	70
Figure 3-10	T_{z0} of linearly optimized designs for the 1-DOF rotary motor.....	72
Figure 3-11	Integer programming for 8 and 10 EMs.....	73
Figure 3-12	Optimized rotor PM designs for the 1-DOF rotary motor	73
Figure 3-13	Optimization parameters for the 2-DOF orientation stage.....	74
Figure 3-14	Weight factors for the linear optimization	76
Figure 3-15	T_{x0} of optimized designs for the 2-DOF orientation stage	76
Figure 3-16	Integer programming for the design with 2 and 3 EMs	77
Figure 3-17	Optimized rotor designs for the 2-DOF orientation stage.....	78
Figure 4-1	Illustrative applications for the design optimization.....	81
Figure 4-2	Angle definition of EM and design space with two different PM layers..	84
Figure 4-3	EM current input for even poles ($N_{RL}=2$).....	84
Figure 4-4	EM current input for odd poles ($N_{RL}=3$)	84
Figure 4-5	τ_{x0} and τ_{z0} of linearly optimization designs for different ϕ_0	90
Figure 4-6	Chosen rotor designs of each design case	91
Figure 4-7	Evaluated torque characteristics of each design case.....	93
Figure 4-8	Optimized full rotor designs.....	94
Figure 4-9	External loads on the spherical motor	96
Figure 4-10	Performance of optimized designs subjected to an external loading	97
Figure 4-11	Torque output and volume efficiency	99
Figure 4-12	Optimized designs over the weight efficiency	100
Figure 4-13	Design optimizations for a 2-DOF linear-rotary motor	101
Figure 4-14	Optimization parameters for the 1-DOF rotary motor	101
Figure 4-15	Optimization parameters for the 1-DOF linear motor.....	102
Figure 4-16	T_{z0} of linearly optimized designs for the 1-DOF rotary motor.....	104
Figure 4-17	Optimized rotor PM designs of the 1-DOF rotary motor.....	104
Figure 4-18	F_{x0} of optimized designs for the linear motor	105
Figure 4-19	Integer programming for the design with 8 and 10 EMs	105

Figure 4-20	Optimized rotor designs for the linear motor	106
Figure 4-21	Stator and rotor design space for the linear-rotary motor optimization ..	107
Figure 4-22	EM current input for the linear-rotary motor optimization	108
Figure 4-23	Evaluated minimum torque for different axial loads	111
Figure 4-24	Optimized rotor designs for the linear-rotary motor	111
Figure 4-25	Torque output of the optimized designs for axial loadings	112
Figure 4-26	Design layouts for DSSM optimization	113
Figure 4-27	Two types of 3-phase EM inputs	115
Figure 4-28	Optimized rotor designs for optimized LD	117
Figure 4-29	Simulated torque for optimized LD	117
Figure 4-30	Optimized rotor designs for optimized SD	118
Figure 4-31	Simulated torque for optimized SD.....	119
Figure 4-32	Bar-shaped PMs to design DSSM rotors	120
Figure 4-33	CAD model of optimized DSSM rotor	120
Figure 4-34	Torque response of CAD model of LD.....	121
Figure 4-35	Torque response of CAD model of SD	122
Figure 5-1	CAD experimental setup of DSSM.....	125
Figure 5-2	Experimental setup of DSSM.....	126
Figure 5-3	Precision rotational stage for DSSM experiment.....	127
Figure 5-4	CAD mechanical assembly to measure DSSM torque.....	129
Figure 5-5	CAD torque measurement setup and its parameters	129
Figure 5-6	Spring calibration with external weights.....	129
Figure 5-7	Spring calibration by a linear least-square fit	130
Figure 5-8	Comparison of DSSM flux density	131
Figure 5-9	Comparison of DSSM torque.....	132
Figure 5-10	CAD model of existing PMSM orientation stage	133
Figure 5-11	Hall-effect sensors to measure magnetic field of the rotor PMs.....	134
Figure 5-12	Flux density comparison of rotor PMs.....	136
Figure 5-13	Flux density comparison of the rotor PMs at $\phi = 0^\circ$ and $\pm 20.16^\circ$	136
Figure 5-14	Torque comparison of WCR	137
Figure 5-15	EM torque comparison of spherical motor.....	138

Figure 5-16	Design of the magnetic wheel	140
Figure 5-17	Torque measuring setup for magnetic wheel	140
Figure 5-18	DMC assemblies for various wheel orientations	142
Figure 5-19	Torque comparison of the magnet wheel on an iron bridge.....	143
Figure 5-20	CAD PM-LSynM.....	144
Figure 5-21	Air gap flux density measurement	146
Figure 5-22	Identified magnetizations of PMs	148
Figure 5-23	Flux density comparison with measured data	149
Figure 5-24	Identified coil positions.....	151
Figure 5-25	Force comparison of the PM-LSynM	151
Figure B-1	Definition of a PM design variable	163

LIST OF SYMBOLS AND ABBREVIATIONS

Capital Symbols

A	Magnetic vector potential
B	Magnetic field or flux density
D	Displacement current
E	Electric field
H	Magnetic field intensity
J	Volume current density
J_c	Electric input current density
J_e	Eddy (or induced) current density
J_{max}	Maximum electric input current
K	Surface current density
K_p	Equivalent magnetizing current on PM
K_p	Equivalent magnetizing current on magnetic material
M	Material magnetization vector
M_{max}	Maximum PM magnetization
N_{PM}	Number of PMs
N_{EM}	Number of EMs
N_{inp}	Number of independent EM inputs
N_v, N_s, N_M	Number of PM volume, and PM and iron surface elements
M_r, M_θ, M_φ	PM magnetization in spherical coordinates
P	Number of rotor positions or orientations
T_{x0}, T_{z0}	Minimum torque about x or z axis
T₀	Minimum torque about x and z axes
V_r	Volume ratio constraint

Lower Case Symbols

b_i	Bounding radius of i^{th} DMC element
d_i	Dividing radius of i^{th} DMC element
$\mathbf{e}_x, \mathbf{e}_y, \mathbf{e}_z$	Unit directional vectors in xyz coordinates
\mathbf{j}_i	DMC current of i^{th} element
k_i	Division number of i^{th} DMC element
l_i	Maximum division level of i^{th} DMC element
l_{pole}	Length of PM poles
$\mathbf{n}, \mathbf{t}, \mathbf{b}$	Surface normal, tangent and binormal vectors
n_c	Number of DMC elements at Level 0
n_{pole}	Number of PM poles
n_{PM}	Number of n_{pole} cases for Layout Optimization
n_{EM}	Number of N_{EM} cases for Layout Optimization
w	Optimization weight factor

Greek

μ_0	Permeability of free space (air)
μ	Permeability of magnetic material
ρ_i	Material density vector
$\bar{\rho}$	Positive material density variables
Ω	Domain of electromagnetic component

Abbreviations

(1,2,3)D	One, two or three dimensional
DMC	Distributed Multi-Level Current model
(M-)DOF	(Multi-) Degree of Freedom
DMP	Distributed Multi-Pole model
DSSR	Disk-shaped synchronous motor
EM(s)	Electromagnet(s)

EMC	Equivalent Magnetizing Current
FDM	Finite Difference Methods
FEM, FEA	Finite Element Methods, Analysis
FMN	Flexible Mobile Node
LR	Linear-rotary
MLM	Meshless Methods
MSE	Mean Square Errr
OMD	Optimized Material Distribution
PDE	Partial Differential Equation
PM(s)	Permanent magnet(s)
PMSM	PM Spherical Motor
PM-LSynM	PM linear synchronous motor
WCR	Weight Compensating Regulator

SUMMARY

This thesis has been motivated by the growing needs for multi-degree of freedom (M-DOF) electromagnetic actuators capable of smooth and accurate multi-dimensional driving motions. Because high coercive rare-earth permanent-magnets (PMs) are widely available at low cost, their uses for developing compact, energy-efficient M-DOF actuators have been widely researched. To facilitate design analysis and optimization, this thesis research seeks to develop a general method based on distributed source models to characterize M-DOF PM-based actuators and optimize their designs to achieve high torque-to-weight performance with compact structures.

To achieve the above stated objective, a new method that is referred to here as distributed multi-level current (DMC) utilizes geometrically defined point sources has been developed to model electromagnetic components and phenomena, which include PMs, electromagnets (EMs), iron paths and induced eddy current. Unlike existing numerical methods (such as FEM, FDM, or MLM) which solve for the magnetic fields from Maxwell's equations and boundary conditions, the DMC-based method develops closed-form solutions to the magnetic field and force problems on the basis of electromagnetic point currents in a multi-level structure while allowing trade-off between computational speed and accuracy. Since the multi-level currents can be directly defined at the geometrically decomposed volumes and surfaces of the components (such as electric conductors and magnetic materials) that make up of the electromagnetic system, the DMC model has been effectively incorporated in topology optimization to maximize the torque-to-weight ratio of an electromechanical actuator. To demonstrate the above

advantages, the DMC optimization has been employed to optimize the several designs ranging from conventional single-axis actuators, 2-DOF linear-rotary motors to 3-DOF spherical motors.

The DMC modeling method has been experimentally validated and compared against published data. While the DMC model offers an efficient means for the design analysis and optimization of electromechanical systems with improved computational accuracy and speed, it can be extended to a broad spectrum of emerging and creative applications involving electromagnetic systems.

CHAPTER 1

INTRODUCTION

1.1 BACKGROUND AND MOTIVATION

Electromagnetic actuators are electrically powered devices (that convert magnetic energy into mechanical energy) and are widely used for various applications ranging from industrial machine drives, robotics, to household appliances. In recent years, the growing needs for precision multi-degree of freedom (M-DOF) actuators capable of dexterous smooth motions have attracted the attention of many researchers. Based upon new topologies (such as planar, rotary-linear and ball-joint-like spherical mechanisms), M-DOF actuators are often designed to take advantages of the high coerciveness of rare-earth permanent magnets (PMs), which are widely available at low cost. However, the modeling and analysis of M-DOF motion in three dimensional (3D) space is often difficult because it involves complex geometry, and improving the design through optimization processes is also challenging. The modeling and analysis of a single-DOF actuators system often rely on either formulated as a lumped-parameter magnetic circuit for solving it in closed form or numerically using a commercially available software. The magnetic circuit analysis which yields only first-order accuracy is inadequate for analyzing sophisticate system like M-DOF actuators. Also, the magnetic solutions computed by numerical methods are often quasi-static in nature, and require relatively high computational cost for characterizing material boundary and enclosed space; it is inefficient for analyzing the rotor motion which changes in 3D space.

In this research, a distributed multi-level current (DMC) model is developed as an alternative method for analyzing M-DOF actuators to improve design efficiency, particularly for design optimization. The DMC model, which enables fast computation by relocating effective sources, inherits many advantages from the distributed multi-pole (DMP) model [1]. As its previous counterpart, the DMC offers intuitive force/torque solutions in closed-form. Additionally the current-based description describes the electromagnetic source effects (including magnetic material and eddy current) from the quantitative definition of Maxwell's equations. As will be shown, the main drawback of such point-wise description (which may lead to erroneous results around their nearby points) can be fixed with a fine division of the local sources to guaranty desired accuracy of the model. Also, the local source division improves optimization efficiencies with an additional accuracy control over the resolution of the domain decomposition.

This thesis research has been motivated by an existing electromagnetic spherical motor [2] developed at Georgia Tech, which operates the 3-DOF motion in a single ball-joint-like joint. To overcome difficulties on modeling electromagnetic effects, the DMP method has been applied to orientation sensing and control [3] of a spherical motor. Although the parametric effects in terms of the pole (stator and rotor) number were simulated during initial design, little efforts have been directed towards the design optimization of the spherical motor in terms of the overall torque-to-weight ratio. For this reason, this thesis research aims at developing a DMC-based topological optimization method for maximizing the overall torque-to-weight ratio of electromagnetic actuators including a spherical motor. While optimizing with compromising performance

specifications, the numbers and rotor/stator pole shapes will be further investigated to simplify design complexity and control efforts of the M-DOF actuator.

1.2 REVIEW OF PRIOR AND RELATED WORKS

Electromagnetic field analyses rely on the classical electromagnetism theory represented by Maxwell's equations. Existing analysis techniques can be categorized into analytic and general numerical methods, magnetic circuit, and electromagnetic source models; each begins with a review of these methods followed by surveys on electromagnetic system, M-DOF actuators and related research topics.

1.2.1 Analytic and magnetic circuit methods

Analytic methods solve the governing equations as a boundary value problem to obtain solutions in analytical form so that the designed systems can be easily simulated and realized with a simple control model. Most analytic methods assume idealized shapes to simplify the steps of complex derivation and forms of solutions [4]; the solutions, however, generally include a series of space harmonics of non-elementary functions [5] to be numerically computed. Also non-ideal fields such as fringing effect and/or flux leakage are often necessary to be corrected by additional models [6].

The concept of magnetic circuits utilizes ferromagnetic materials analogous to electric circuits to form closed flux paths, and models the system with lumped parameter elements. In many industrial applications, the magnetic circuit offers simple models enabling fast computation for solving the solutions to analyze the system problems.

However, its closed flux path, confined by the iron structure, and first-order accuracy are inadequate to achieve optimized M-DOF design.

1.2.2 Numerical methods for electromagnetic actuators

Numerical methods are commonly utilized to solve electromagnetic fields from simple static to dynamic problems using digital computers with high computational power. As a general partial differential equation (PDE) solver, these methods solve for the magnetic fields from Maxwell's equations with an appropriate set of boundary conditions. Finite element method (FEM) [7] [8] [9] is one of the most general methods offering standard analysis routines for solving various engineering problems. While FEM is necessary to solve the field of overall design and enclosing space, boundary element method (BEM) [10] [11] discretizes only boundaries of source domains. BEM could reduce computational loads for some applications, but it becomes inefficient when the surface-to-volume ratio (as commonly encountered in magnetic actuators) becomes large. Finite difference method (FDM) [12] is another method that discretizes and solves the governing equations in a straight forward way, but it is difficult to apply boundary conditions with complex geometry. Recently adaptive meshes for FEM [13] [14] have been applied for improving solution accuracy in the neighborhoods of air-gaps and the material boundary where magnetic fields drastically change. Also, meshless methods (MLM) [15] [16] similar to FEM but requiring no mesh offer an alternative method for accurately controlling the distribution of kernel sources. However, these general PDE solvers demand much effort on solving material boundary and enclosing space. Also, these methods only yield the field solutions of a specific design assembly at static rotor

position, which demands additional computations costs when the effects of small changes in a design parameter or rotor position must be analyzed during the process of design optimization.

1.2.3 Electromagnetic Source based Magnetic Field Model

In classical electromagnetisms, the actuator magnetic field is generated either by electric current flow due to the voltage difference or material magnetization. The latter, which can be interpreted as electrons circulating around a nucleus, can be modeled by means of fictitious magnetic charges (or equivalent current) such as a magnetic dipole moment of a small current loop [17].

Craik [18] discussed the pole and dipole (doublet) models based on magnetic charges for calculating the magnetic field of simple cylinder shaped magnets. With compact and intuitive formulation, these models have been used for analyzing the effects of PM on actuators [19] [20]. Kabashima *et al.* [21] and Henneberger *et al.* [22] illustrated the equivalent magnetizing current (EMC) for modeling the boundary effects of magnetic materials and calculate forces. Quantitative definition of EMC has offered a unified current description of electromagnetic sources, and is often applied to analyze electromagnetic systems involving ferromagnetic materials [23].

Rokhlin and Greengard [24] [25] have developed a fast multi-pole method (FMM) to solve large scaled electromagnetic phenomena (like radiation and scattering problems). While FMM models an electromagnetic system with clustering electric and magnetic poles described by Green's function and multi-pole expansion, hierarchical refinement of meshes and multi-level approximation [26] could dramatically reduce the

computational complexity depending on the particle distances. Although it is hard to expect high efficiency on a small scaled system (like a magnetic actuator), the clustered source description and hierarchical multi-level approximation can be adopted on improving the DMC model on this research.

At Georgia Tech, Lee and Son [1] introduced a DMP method for deriving a magnetic field solution of PM and EM in closed-form. Distributed dipoles, a pair of source and sink separated by a distance, are optimally located in PM and EM, and efficiently analyze the 3D magnetic field of a spherical motor for its design and control problems [3]. The closed-form force equation using DMP models have been developed by Lee *et al.* [27] followed by an image method on the characterization of iron boundary [28]. This method can intuitively explain the component-wise effects of magnetic actuators with a set of point sources, but its usage to topology optimization is limited when shape and magnetic field data of the components are not available. Also, it shows several problems on design analyses (such as large errors inside magnetic sources, hard to handle general material shape and current induction). This research will extend and generalize the DMP model by introducing multi-level approximation of point current sources, and apply it to design optimization and analysis of M-DOF actuators.

1.2.4 M-DOF Actuators and Spherical Motors

Many industrial and research applications (such as industrial machining tools, mobile robots, haptic device, wheel and propeller driving) require M-DOF actuators to achieve dexterous and precise motion with a compact size. Many MDOF actuators have been designed for extremely fine motion with piezoelectric technology since 3-DOF

micro-motion in-parallel mechanism using piezoelectric elements have been presented by Lee and Arjunan [70]. 3-axis micro positioners have developed by Erlandsson and Olsson [29] using frictional drive of piezoelectric elements and Chang *et al.* [30] with the aid of mechanical motion amplifier. Also, Toyoma *et al.* [31] and Amano *et al.* [32] have researched on ultrasonic spherical motors, and followed by Mashimo *et al.* [33] [34] and Bo *et al.* [35]. Although piezoelectric elements allows the advantage of fine motion resolution in small size, it has several disadvantages such as low speed output, wear and high cost which limit its effectiveness on M-DOF designs.

Electromagnetics offers an alternative method to achieve M-DOF design with low cost, high speed and reliability. A levitated planar motor with short-stroke moving PM was developed by Trumper, Kim and Lang [36] [37] and Compter [38] suggested the long stroke type with moving EM. Jansen *et al.* [39] discussed design and optimization of the 6-DOF levitated planar actuator that is capable of large horizontal moving and small rotation. Also rotary-linear motor that combines spinning and translational motion along a same axis have designed by Krebs *et al.* [40] and Bolognesi *et al.* [41]. Many of these actuators are simply designed by combinations of actuator designs along each motional direction; researches are focused on improving levitation performance of the moving part rather than optimizing actuator designs.

Spherical motor motivated by realizing 3-DOF motion in a ball-joint-like actuator have attracted many researchers. Williams *et al.* [42] proposed a single-axis induction motor with a spherical rotor to allow for speed control by mechanically orienting the axis of the rotor with respect to the stator. Three decades later, various forms including induction [43] [44], direct current (DC) [45] and stepper [46] motors are developed.

Since the work of Lee and Kwan [47] on spherical steppers and the subsequent extension to variable reluctance spherical motor (VRSM) which achieves high-resolution motion with relative small number of magnets, several different versions of spherical motors have been developed. Among them, Wang et al. [48] [49] developed a similar actuator with simple rare-earth PM and coil-arrangement. More recently, Lee et al. [2] have developed a spherical wheel motor (SWM) to achieve continuous spinning motion with inclination regulation, and a similar design was investigated by Yan et al. [50] [4]. Although the main objective of spherical motors that operate 3-DOF motion in a single joint has been realized in recent designs, several difficulties still exist such as relatively low output performance with large and complex designs.

1.2.5 Optimization of Electromagnetic Actuators

The designs of M-DOF actuators have often been accomplished by designers' intuition or motivated by applications. Based on an initial concept and existing design, several key geometric or input parameters are optimized to improve performance. These optimization processes are usually referred to as shape or parameter optimization, which have been widely used to improve specific design features with various objectives such as the rotor PM shape [51] and stator iron tooth shape [52] optimization over efficiency and cogging force reduction [53]. However, the range of the feasible solution is limited since it only handles small numbers of optimization parameters with the designer's intuition and simple geometries.

Recently, topology optimization has gained attention in the design of magnetic actuators since it can be applied for initial design steps and often makes optimized result

beyond designer's expectation. Topology optimization is originated from structure engineering researches. Optimized material distribution (OMD) based on FEM has been widely used for designing actuators since Dyck et al. [54] [55] described the ideas based on sensitivity analysis and material penalization. Later Labbe and Dehez [56] [57] have combined OMD scheme with convexity mapping to improve global convergence of iron stator. Some researchers have adopted a level set method to represent clear and flexible boundary in topology optimization while minimizing gradual change of material mixtures. Okamoto et al. [58] [59] suggested simple on/off method and applied it to 3D optimization later. Park et al. [60] and Lim et al. [61] applied a level set-based method to optimize the shapes of iron yoke.

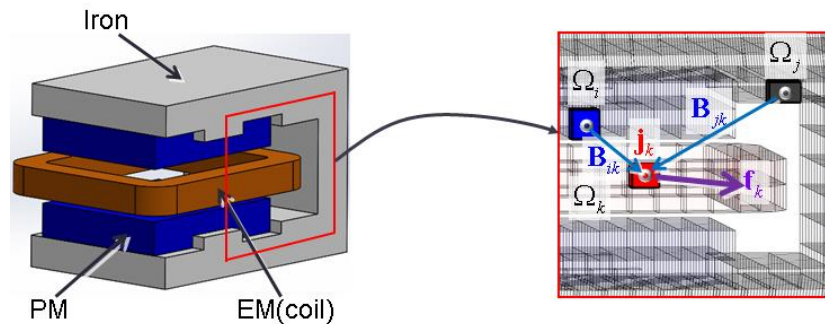
Generally, topology optimization employs FEM for analyses in most of engineering problems. However, material boundary discontinuity tends to yield large errors on the design of magnetic actuators while improving accuracy with fine-resolution meshes or adaptive meshing in whole design domain will increase computational effort. Instead of FEM, the use of DMC models in topology optimization can improve computational efficiency in designs since fixed material volume and boundaries are represented by point sources. Additionally their field accuracy can be regulated by local source division during the optimization process.

In this research, DMC based optimization of a spherical motor is investigated to improve an existing spherical orientation stage [27] and newly design linear-rotary motor. Also, disk-shaped synchronous motor, as a kind of flat electric motors (or axial-flux motor), is optimized to achieve higher torque-to-weight ratio and lower vibration [67] [68] comparing with a conventional radial-flux PM motor.

1.3 PHILOSOPHY OF DISTRIBUTED MULTI-LEVEL CURRENT

Distributed multi-level current

On the analysis of actuators, dipoles and magnetizing currents explain material boundary conditions with fictitious magnetic charges and current respectively. Comparing with general numerical methods (such as FEM), magnetic field can be intuitively explained by integrating effects of magnetic sources only along material boundary. Instead of using numerical integration along continuous domain, the concept of point electric and magnetizing current sources which can significantly reduce computation speed when characterizing of the magnetic fields and forces using a unified current notation.



(a) CAD model of a linear motor (b) point sources on decomposed geometry

Figure 1-1 Schematic illustration of electromagnetic point sources

A general 3D geometry of an electromagnetic actuator (containing PM, EM, and iron) can be decomposed into small volumes, and then point currents can be located on the geometric center of each volume or surface as shown in Figure 1-1. Since the magnetic fields from point sources can be described by multiplying the point source

strength to the scalar kernel function, the magnetic field and force equations can be written in closed forms. As a simple illustration of computing magnetic field and force, the point sources defined by the decomposed volumes (Ω_i , Ω_j , and Ω_k on the rectangular PM, iron stator frame and EM) are highlighted in Figure 1-1(b). The magnetic field formed on Ω_k by Ω_i and Ω_j becomes $\mathbf{B}_{ik} + \mathbf{B}_{jk}$; and the thrust force \mathbf{f}_k can be simply evaluated by multiplication of $(\mathbf{B}_{ik} + \mathbf{B}_{jk})$ and the point current \mathbf{j}_k located on Ω_k using the Lorentz force equation.

The main drawback of using point sources is that their representations of electromagnetic material geometry are inaccurate around the region near the source position where the magnetic field error becomes large. To minimize such errors, DMP models relocate the dipoles inside the material geometry; but it needs an additional optimization using accurate magnetic field distribution determined by another methods. To avoid such identification steps, multi-level structured point currents (referred to as DMC local sources here), control computational accuracy and speed of the magnetic fields with respect to a distance. The local source concepts is illustrated by 4 point currents located on decomposed geometries in Figure 1-2; and dotted circles denote the boundary where magnetic field error becomes intolerable. To evaluate the magnetic field on a far-away space point \mathbf{r} , Figure 1-2(a) only uses 4 initial point currents for better computational speed. For nearby \mathbf{r} in Figure 1-2(b), closely located sources are replaced with a set of local sources defined by recursively decomposed source geometry, and improve the field accuracy with minimal additional computational efforts. With unlimited local source division, the magnetic field can converge to a true solution. However, as computational efficiency is important in practical implementation, the number of source

decomposition is limited, and scalar function nearby point sources is modified to effectively represent field cancellation inside the material geometry. In Chapter 2, the magnetic field and force equations of point currents are derived in closed form, and local source and its field approximation are developed to improve computational efficiency.

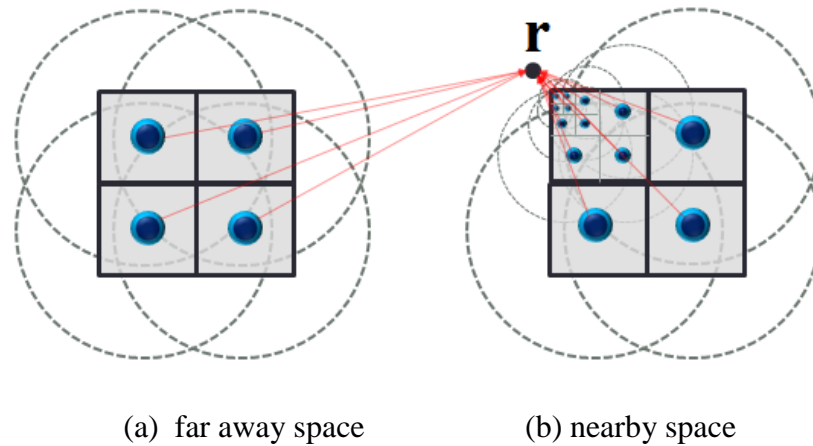


Figure 1-2 DMC local sources for magnetic field computation

Layout optimization by DMC

The initial design of a PM-based electromagnetic actuator begins with a specified number and shape of EM and PM, which meets a given size specification. This is a critical step since it outlines an overall output characteristics of actuator performance. However, many designs are based on modifying magnets from existing designs or comparing several combinations of magnets. The main reason why initial designs only handle limited design cases is mainly related to high computation cost on analyzing electromagnetic effects. For the design of a M-DOF actuator, such computational load can be significantly increased by multi-dimensional motions.

As shown in Figure 1-3, the DMC model can linearly represent magnetic field and force in terms of electromagnetic sources such as electric current or material magnetization. It can be utilized to systematically convert the initial design step into an efficient optimization problem. The design problems are simplified with reasonable conditions, followed by formulating a set of linear topology optimization problems for various combinations of repetitive PMs and EMs. Then, the net force and/or torque are evaluated for each of the linearly optimized designs; and the best combination of PM and EM is chosen by an optimized design layout. Here, this optimization strategy is referred to as a layout optimization which can be an efficient tool for initial designs of actuators. Detailed concept and formulation of the Layout Optimization will be described in Chapter 3.

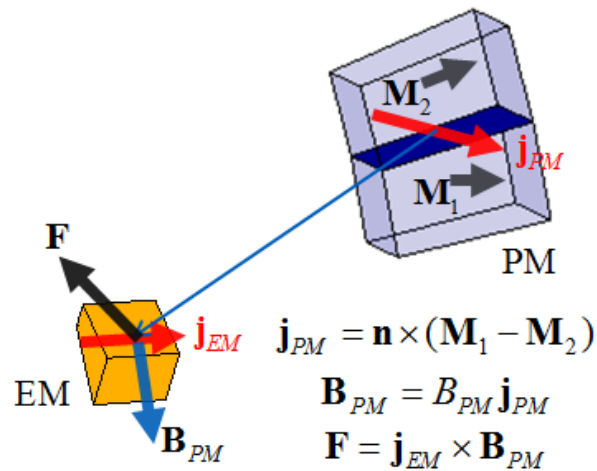


Figure 1-3 Linear force in terms of electromagnetic sources

1.4 RESEARCH OBJECTIVE

This research aims at developing a modeling method for design and analyses of a 3D electromagnetic actuator capable of M-DOF motions in a single joint. This thesis research comprises of three objectives:

The first is the development of a modeling method to characterize the magnetic field and force of an electromagnetic system for the design of electromechanical actuators.

The multi-level source model, referred to here as a DMC model, represents the decomposed geometry of electromagnetic materials with a set of point currents in a multi-level structure. This method formulates the magnetic field and force of the electromagnetic elements which may be a PM, an EM, iron and/or eddy current. This model offers an efficient way to analyze electromagnetic actuators and an effective basis for developing a design optimization model.

The second is to develop a topology optimization model to maximize the torque-to-weight ratio of M-DOF electromagnetic actuators based on the geometry-based modeling approach of the DMC.

The DMC model defined at the geometrically decomposed volumes and surfaces is used to represent set decomposed rotor design space with PM material density variables,

and efficiently incorporated in topology optimization of an electromagnetic actuator to maximize torque-to-weight ratio. To avoid expected problems caused by nonlinear force/torque equations and constraints, a general topology optimization is converted into a number of the linear topology optimizations, and then the optimalities of the linearly optimized designs are evaluated by output torque and design compactness during a integer programming step. The Layout Optimization covers a broader range of design cases combined with geometry-based DMC model, and its efficient computational approach facilitates design optimization of a M-DOF actuators. To demonstrate this optimization approach, several designs including a spherical motor and a linear-rotary motor are illustrated; the layouts of each moving direction are separately optimized, and then the combined 3D layouts are optimized to maximize desired output performances.

The final objective is to experimentally investigate the effectiveness of DMC models for electromagnetic actuator related applications, and validate simulated results against known solutions or experimental data.

To validate the DMC model against experimental data, a DMC-based optimized motor that has been fabricated and an existing M-DOF actuator are analyzed. To analyze these actuators consisting of many similar sized EM, PM and iron, each of these components is modeled, and reassembled in 3D space, the magnetic field and output performance of which can be efficiently simulated for different orientations. Several researches related electromagnetic systems are used to demonstrate and validate the effectiveness of the DMC models.

1.5 OUTLINE AND ORGANIZATION OF THESIS

The remainder of the dissertation is outlined as follows.

Chapter 2 starts with a brief review of general electromagnetic equations in the view of electromagnetic current sources, upon which the DMC model is developed. The DMC model that represents the decomposed geometry of electromagnetic material as point current sources is derived for describing the magnetic field and force in closed form. Also, local source approximations are described using multi-level structure and local field correction, which improve the accuracy around point sources. For magnetic material and eddy current, a detailed formulation is described in terms of DMC model. Finally, several examples modeled by the DMC are illustrated, and validated against available analytic solution or published experimental data.

Chapter 3 develops the design optimization of electromagnetic actuators based on DMC models, referred to here layout optimization. To avoid non-linearity and local convergence during design optimization, this chapter starts with schematic illustration of the layout optimization consisting of linear topology and integer programming. To formulate linear optimization problems for each combination of EM and PM poles, desired current inputs of an EM is described, and then DMC model is used to topologically optimize design space with PMs. In the last part of this chapter, two examples are presented to illustrate the DMC model for optimizing 1-DOF rotary motor and 2-DOF orientation stage, the results of which are subsequently used to optimize 3-DOF spherical motor design in the following chapters.

Chapter 4 illustrates the DMC optimization applications for designing three electromagnetic actuators; spherical, linear-rotary and disk-shaped synchronous motors. On the spherical motor design, a ball-joint-like 3-DOF motor is optimized based on an existing design to improve the output torque and design compactness. To optimize tubular-shaped linear-rotary motor, 2D designs for linear and spinning motions are separately optimized, and then the design layouts are further optimized in 3D. Finally, single-axis disk-shaped synchronous motors are optimized for small and large sizes using 3-phase electric current inputs.

In the Chapter 5, simulated results of the DMC models for a fabricated DSSM, spherical motor, magnet-car and iron PMLSM are validated against experimental results. As an experimental investigation of the DMC model, one of optimized DSSM designs is fabricated for validating the optimized design. To validate the DMC model for analyzing of the M-DOF actuators, analytical results of an existing 3-DOF spherical orientation stage are compared against experimental data. Finally, the DMC model is used to analyze a magnet car moving on bridge iron and identify design parameters of ironless PMLSM, which are validated against available experimental data.

Finally, Chapter 6 presents the conclusions and contributions of this thesis and offers recommendations of future researches on DMC model and its applications.

CHAPTER 2

DISTRIBUTED CURRENT-BASED MAGNETIC FIELD MODEL

Motivated by the needs to develop efficient methods for designing general electromagnetic actuators consisting of PMs, EMs and ferromagnetic materials, DMC model is developed to facilitate magnetic field analysis and improve design optimization. This chapter begins with a brief review of general equations from the perspective of electromagnetic current sources to provide the subsequent derivation of the closed-form magnetic field/force equations which are formulated on the basis of point current sources representing decomposed electromagnetic materials. To improve the accuracy around the point sources, the methods of local source approximation and field correction based on multi-level structure are described next. Finally, electromagnetic components that include PM, EM, iron and eddy current commonly used in actuators are characterized using DMC models as illustrative examples, which have been validated by comparing against known solutions or published experimental data.

2.1 ELECTROMAGNETIC EQUATIONS FOR ACTUATORS

The following assumptions are made in developing the electromagnetic field model:

- (1) The electromagnetic materials are isotropic and homogeneous. This assumption enables the macroscopic continuum approximation of electromagnetic field described by following continuity equations:

$$\nabla \cdot \mathbf{B} = 0 \text{ and } \nabla \cdot \mathbf{E} = \frac{\rho}{\epsilon_0} \quad (2.1 \text{ a,b})$$

where \mathbf{B} is magnetic flux density (or magnetic field); \mathbf{E} is the electric field; ϵ_0 is the permittivity of free space; and ρ is the electric charge density.

- (2) The magnetic material is soft or operates within a linear region with negligible hysteresis effects. This assumption implies that the relation between magnetic flux density \mathbf{B} and magnetic field intensity \mathbf{H} of the magnetic material is linear with a constant permeability μ :

$$\mathbf{B} = \mu \mathbf{H} \quad (2.2)$$

- (3) The electric conductors obey Ohm's law:

$$\mathbf{J} = \sigma \mathbf{E} \quad (2.3)$$

where \mathbf{J} is the electric current density; \mathbf{E} is the electric field; and σ is the bulk electrical conductivity.

- (4) The operating frequencies are low enough and/or actuator size is relatively small to satisfy magneto quasi-static (MQS) conditions, which enables to neglect the effects of displacement current \mathbf{D} . Haus and Melcher [62] have described a valid condition for MQS approximation by $2\pi fL \ll 1/\sqrt{\mu\epsilon} \approx 3 \times 10^8$ in terms of operating frequency f , actuator characteristic length L , material permittivity ϵ , and permeability μ . Considering an actuator ($L=0.01\text{m}$) as an example, the electromagnetic field analysis can be simplified by the MQS approximation for operating up to $f = 10^6 \text{ Hz}$ (since it satisfies the condition $2\pi \times 10^4 \ll 3 \times 10^8$).

In short, the electromagnetic actuator analysis will be based on linear electric and magnetic material properties and MQS condition.

2.1.1 Electromagnetic Sources

An electromagnetic field is generated in space due to the electric current flowing into a conductor and/or due to the boundary effect of magnetic material. For the purpose of analyzing an actuator, these electric current and boundary effect are referred to here as electromagnetic sources which are broadly categorized into four types as illustrated in Fig. 2-1 where the displacement current effect is excluded because of the MQS approximation:

- free electric current, \mathbf{J}_c
- eddy (or induced) current, \mathbf{J}_e
- equivalent magnetizing current on PM, \mathbf{K}_p
- equivalent magnetic material current, \mathbf{K}_m

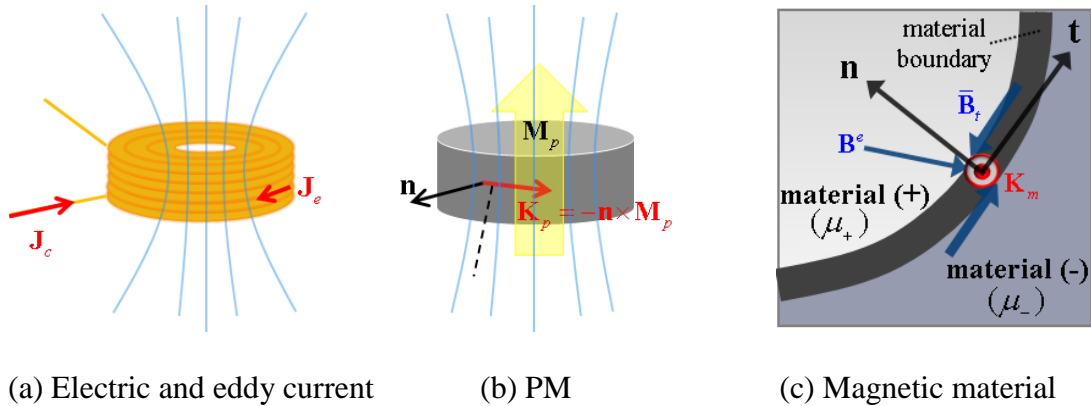


Figure 2-1 Electromagnetic sources

As shown above, the surface current density \mathbf{K} represents a conceptual magnetizing current for explaining the boundary effect of a magnetic material, whereas the volume current density \mathbf{J} denotes an actual flowing electric current through a

conductor. An input electric current that flows along an EM coil winding can be directly converted into \mathbf{J}_c . Similarly, \mathbf{K}_p of a PM is determined from the cross-product of the surface normal vector \mathbf{n} and constant magnetization \mathbf{M}_p with respect to air magnetization $\mathbf{M}_{air}=0$:

$$\mathbf{K}_p = \mathbf{n} \times (\mathbf{M}_{air} - \mathbf{M}_p) \quad (2.4)$$

or

$$\mathbf{K}_p = -\mathbf{n} \times \mathbf{M}_p \quad (2.5)$$

Unlike an EM or a PM, the material magnetizing current \mathbf{K}_m and the eddy current \mathbf{J}_e depend on an existing and a time-varying electromagnetic field respectively. The boundary condition of the magnetic material (described in APPENDIX A), which defines \mathbf{K}_m , is given by

$$\mathbf{K}_m(\mathbf{r}_i) = -\mu_i \left[\mathbf{B}^e(\mathbf{r}_i) \bullet \mathbf{t}_i \right] (\mathbf{n}_i \times \mathbf{t}_i) \quad (2.6)$$

where \mathbf{n} and \mathbf{t} are unit surface normal vector \mathbf{n} and tangent vector \mathbf{t} ;

$\mu_i = \frac{2}{\mu_0} \left(\frac{\mu_- - \mu_+}{\mu_- + \mu_+} \right)$ for two different magnetic permeability μ_+ and μ_- ; and $\mathbf{B}^e(\mathbf{r}_i)$ denotes

an external flux density on the boundary surface \mathbf{r}_i . Also, Faraday's law (detailed descriptions are in following section) describes \mathbf{J}_e in terms of the vector potential \mathbf{A} :

$$\mathbf{J}_e = -\sigma \frac{\partial \mathbf{A}}{\partial t} \quad (2.7)$$

$$\mathbf{B} = \nabla \times \mathbf{A} \quad (2.8)$$

Once all the electromagnetic sources are represented in the form of current density, the magnetic field and force can be directly formulated by the Biot-Savart law

and the Lorentz force equation. The governing equations using the above defined sources are described on the next sections based on Maxwell's equations.

2.1.2 Governing Equations of Electromagnetic Field

In classical electromagnetism, Maxwell's equations describe the magnetic flux density \mathbf{B} , magnetic field intensity \mathbf{H} , and electric field \mathbf{E} in terms of electric magnetic material effects including electric current density \mathbf{J} , material magnetization \mathbf{M} , and electric displacements \mathbf{D} :

$$\nabla \times \mathbf{H} = \mathbf{J} + \frac{\partial \mathbf{D}}{\partial t} \quad (2.9)$$

$$\nabla \times \mathbf{E} = -\frac{\partial \mathbf{B}}{\partial t} \text{ where } \mathbf{B} = \mu_0(\mathbf{H} + \mathbf{M}) \quad (2.10a,b)$$

To find an explicit representation for the eddy current \mathbf{J}_e , equations (2.3) and (2.8), along with Coulomb gauge $\nabla \cdot \mathbf{A} = 0$, are substituted into (2.10a), which becomes

$$\mathbf{J} = \mathbf{J}_c + \mathbf{J}_e \text{ where } \mathbf{J}_c = -\sigma \nabla \phi \text{ and } \mathbf{J}_e = -\sigma \frac{\partial \mathbf{A}}{\partial t}. \quad (2.11)$$

From (2.8b), $\nabla \times \mathbf{B} = \mu_0(\nabla \times \mathbf{H} + \nabla \times \mathbf{M})$ where $\nabla \times \mathbf{H} = \mathbf{J}$ since the 2nd term on the RHS of (2.9) is neglected for the MQS condition and $\mathbf{n} \times \mathbf{M} = \mathbf{K}$ on the material boundary, the magnetic flux density can be expressed in terms of a volume current density source and a surface current density source, $\mathbf{J} = \mathbf{J}_c + \mathbf{J}_e$ and $\mathbf{K} = \mathbf{K}_p + \mathbf{K}_m$, respectively:

$$\nabla \times \mathbf{B} = \mu_0 \mathbf{J}, \quad \mathbf{n} \times \mathbf{B} = \mu_0 \mathbf{K} \quad (2.12a,b)$$

Using the two fundamental formulations of magneto-statics that specify the divergence and the curl of \mathbf{B} in (2.1a) and (2.12) respectively, the effects of the sources can be formulated in terms of the vector magnetic potential \mathbf{A} in (2.8), the solution to which can be shown to have the integral form:

$$\mathbf{A}(\mathbf{r}) = \frac{\mu_0}{4\pi} \left[\int_{\Omega} \frac{\mathbf{J}(\mathbf{r}')}{R} dV + \int_{\Gamma} \frac{\mathbf{K}(\mathbf{r}')}{R} dS \right] \quad (2.13)$$

where Ω denotes electric conductor; Γ is the boundary surface of magnetic material; \mathbf{r}' and \mathbf{r} represent electromagnetic source position and evaluation point; and $R = |\mathbf{r} - \mathbf{r}'|$.

Using (2.8) and (2.13), the flux density \mathbf{B} can be derived leading to the Biot-Savart Law:

$$\mathbf{B}(\mathbf{r}) = \frac{\mu_0}{4\pi} \left[\int_{\Omega} \frac{\mathbf{J}(\mathbf{r}') \times (\mathbf{r} - \mathbf{r}')}{R^3} dV + \int_{\Gamma} \frac{\mathbf{K}(\mathbf{r}') \times (\mathbf{r} - \mathbf{r}')}{R^3} dS \right] \quad (2.14)$$

2.1.3 Magnetic Force and Torque Equation

For the electromagnetic sources (\mathbf{J} and \mathbf{K}), the MQS magnetic force can be directly computed by the Lorentz force equation:

$$\mathbf{F} = \int_{\Omega} \mathbf{J}(\mathbf{r}_m) \times \mathbf{B}(\mathbf{r}_m) dV + \int_{\Gamma} \mathbf{K}(\mathbf{r}_m) \times \mathbf{B}(\mathbf{r}_m) dS \quad (2.15)$$

where \mathbf{r}_m denotes the source position in moving parts; \mathbf{B} is flux density formed by stationary parts. Also for a rotational center \mathbf{r}_o , torque can be computed in a similar way:

$$\mathbf{T} = \int_{\Omega} (\mathbf{r}_m - \mathbf{r}_o) \times \mathbf{J}(\mathbf{r}_m) \times \mathbf{B}(\mathbf{r}_m) dV + \int_{\Gamma} (\mathbf{r}_m - \mathbf{r}_o) \times \mathbf{K}(\mathbf{r}_m) \times \mathbf{B}(\mathbf{r}_m) dS \quad (2.16)$$

2.2 DISTRIBUTED MULTI-LEVEL CURRENT MODEL

Consider an elemental current source (volume V_i and boundary surface S_i) with constant volume current density \mathbf{J}_i and surface current density \mathbf{K}_i , where the subscript “ i ” denotes the i^{th} element in the source domain as shown in Figure 2-2. In the following formulation, the space point \mathbf{r} being evaluated is assumed to be far from the geometric center $\bar{\mathbf{r}}_i$ and the source point \mathbf{r}_i of the i^{th} element; $|\mathbf{r}_i - \bar{\mathbf{r}}_i| \ll |\mathbf{r} - \bar{\mathbf{r}}_i|$ where \mathbf{r} , $\bar{\mathbf{r}}_i$ and \mathbf{r}_i are the position vectors illustrated in Fig. 2-2.

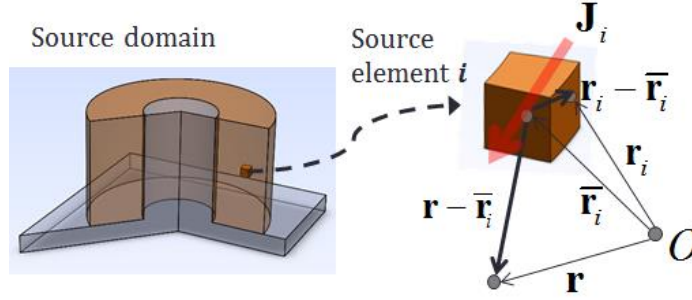


Figure 2-2 Schematic of a source element i

For uniform \mathbf{J}_i and \mathbf{K}_i , the integrands of (2.13) becomes of $1/|\mathbf{r}-\mathbf{r}_i|$ which can be treated as a function of \mathbf{r}_i ; it can be approximated by a Taylor series expansion about $\bar{\mathbf{r}}_i$ with higher order terms neglected:

$$\frac{1}{|\mathbf{r}-\mathbf{r}_i|} \approx \frac{1}{R_i} + \frac{\mathbf{e}_i \cdot (\mathbf{r}_i - \bar{\mathbf{r}}_i)}{R_i^2} \quad (2.17)$$

where $R_i = |\mathbf{r} - \bar{\mathbf{r}}_i|$ and $\mathbf{e}_i = (\mathbf{r} - \bar{\mathbf{r}}_i)/R_i$. Since the integration of the 2nd term on the RHS of (2.17) approaches zero as assumed earlier, the vector potential (2.13) is simplified to

$$\mathbf{A}_i(\mathbf{r}) = \mathbf{j}_i f_a(R_i) \text{ where } f_a(R_i) = \frac{\mu_0}{4\pi R_i} \quad (2.18a,b)$$

and substituting (2.18a) into (2.8) gives magnetic field of a point source i :

$$\mathbf{B}_i(\mathbf{r}) = \mathbf{j}_i \times \mathbf{e}_i f_b(R_i) \text{ where } f_b(R_i) = \frac{\mu_0}{4\pi R_i^2} = \frac{1}{R_i} f_a(R_i) \quad (2.19a,b)$$

where $\mathbf{j}_i = \mathbf{J}_i V_i + \mathbf{K}_i S_i$; f_b and f_a are the scalar kernel functions of the vector potential and magnetic field of a point source. The magnetic field of a source element can be intuitively characterized by the product of the current density (\mathbf{J}_i or \mathbf{K}_i at the geometric center $\bar{\mathbf{r}}_i$) and element size (V_i or S_i) using (2-18a) and (2-19a), but they tend to be erroneous around the source element (as illustrated in Figure 2-3 where the magnetic field is compared to analytical solutions for a point source) because of the following two facts.

- 1) A point source fails to accurately represent the actual geometry in nearby space.
- 2) The magnetic field inside the geometry element linearly decreases as the evaluation point approaches the geometric center where the magnetic field tends to be cancelled out as opposed to rapidly increasing modeled by (2.19a).

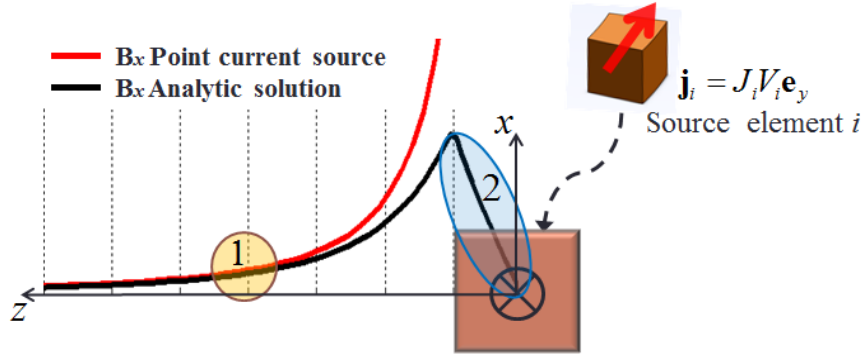


Figure 2-3 Magnetic field errors around the i^{th} source element

2.2.1 Multi-level local source approximation

To improve the accuracy of the point source model, the above problems are handled with the method of recursive local source divisions over the element geometry and modification of the scalar kernel functions, (2.18b) and (2.19b), inside the element.

Recursive local source divisions

The source domain is recursively divided into a number of local point sources to reduce $|\mathbf{r}_i - \bar{\mathbf{r}}_i|$; in other words, the source geometry can be more accurately represented in its nearby space when $|\mathbf{r}_i - \bar{\mathbf{r}}_i| \ll |\mathbf{r} - \bar{\mathbf{r}}_i|$ remains valid. As schematically illustrated in Figure 2-4, the local sources have multi-level structures, which can be effectively represented by octree (or quadtree) data structure.

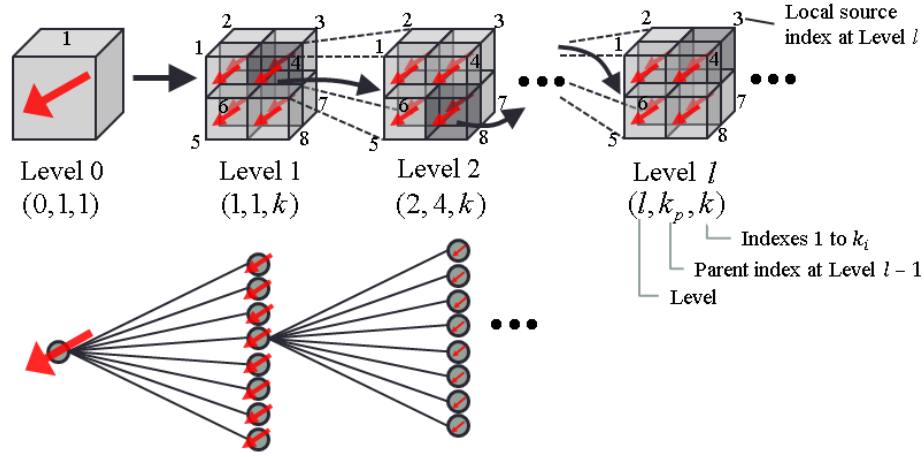


Figure 2-4 Recursively defined local sources and its octree representation

The domain shape can be stored in various ways like a bounding box in certain local coordinates. In this description, a bounding sphere that encloses the element domain with the minimum radius b_i is used. When the distance to the evaluating point is less than a dividing radius d_i , the element domain is equally split into k_i volumes (or surfaces) until a division Level l reaches the maximum division Level l_i . During the source division process, d_i and b_i of the divided domain decrease as its size shrinks, the values of which are determined by the geometric sequences:

$$\begin{aligned} d_i^{(l, k_p, k)} &= d_i^{(l-1, \bullet, k_p)} / 2, \\ b_i^{(l, k_p, k)} &= b_i^{(l-1, \bullet, k_p)} / 2 \quad \text{for } k=1, \dots, k_i; l=1, \dots, l_i \end{aligned} \quad (2.20)$$

where the superscript (l, k_p, k) denotes (division level, parent index at Level $l-1$, local source index in that level); the “ \bullet ” symbol in the superscript means a parent index, i.e. $k=1, \dots, k_i$; k_i represents the element division number for each level (such as 8 for volume and 4 for surface element in Figure 2-4); and k is a divided element of k_p (the parent element in the previous level being divided). Also, if all \mathbf{j}_i at the l^{th} Level can be

determined by the current inputs to EMs, a PM design configuration, or specified iron boundary conditions, \mathbf{j}_i at other levels are determined by following geometric sequences:

$$\begin{aligned} \text{(Upward)} \quad \mathbf{j}_i^{(l-1, \cdot, k_p)} &= \sum_{k=1}^{k_i} \mathbf{j}_i^{(l, k_p, k)} \quad \text{for } l = l-1, \dots, 1 \\ \text{(Downward)} \quad \mathbf{j}_i^{(l, k_p, k)} &= \mathbf{j}_i^{(l-1, \cdot, k_p)} / k_i \quad \text{for } l = l+1, \dots, l_i. \end{aligned} \quad (2.21)$$

When the l^{th} source division level reaches its maximum level l_i , the space point \mathbf{r} being evaluated can be located inside of the bounding radius b_i .

Modification of scalar kernel functions

To improve the accuracy of point sources inside an element, the kernel functions f_b and f_a in (2.19b) and (2.18b) are modified using linear and quadratic polynomials based on the analytical flux density pattern in Figure 2-3. With the following two conditions, the kernel functions are respectively modified into f_B and f_A in equations (2.22) and (2.23):

- 1) $\mathbf{B}_i^{(*)}(R_i^{(*)})$ and $\mathbf{A}_i^{(*)}(R_i^{(*)})$ are continuous at $R_i^{(*)} = b_i^{(*)}$ where the superscript $(*)$ substitutes (l, k_p, k) for simplicity and that
- 2) the magnetic field at the source point is zero, $\mathbf{B}_i^{(*)}(0) = 0$,

$$f_A^{(*)} = \frac{\mu_0}{4\pi} \begin{cases} 1/R_i^{(*)} & \text{if } b_i^{(*)} < R_i^{(*)} \\ \frac{3(b_i^{(*)})^2 - (R_i^{(*)})^2}{2(b_i^{(*)})^3} & \text{if } b_i^{(*)} \geq R_i^{(*)} \end{cases} \quad (2.22)$$

$$f_B^{(*)} = \frac{\mu_0}{4\pi} \begin{cases} 1/(R_i^{(*)})^2 & \text{if } b_i^{(*)} < R_i^{(*)} \\ R_i^{(*)}/(b_i^{(*)})^3 & \text{if } b_i^{(*)} \geq R_i^{(*)} \end{cases} \quad (2.23)$$

The vector potential and magnetic field of a local point source can then be represented in terms of the modified kernel functions as shown in Figure 2-5, by

$$\mathbf{A}_i^{(*)}(\mathbf{r}) = f_A^{(*)} \mathbf{j}_i^{(*)} \quad (2.24)$$

$$\mathbf{B}_i^{(*)}(\mathbf{r}) = \mathbf{j}_i^{(*)} \times \mathbf{e}_i^{(*)} f_B^{(*)} \quad (2.25)$$

where $\mathbf{e}_i^{(*)} = (\mathbf{r} - \mathbf{r}_i^{(*)}) / R_i^{(*)}$ is a unit direction vector from the local source.

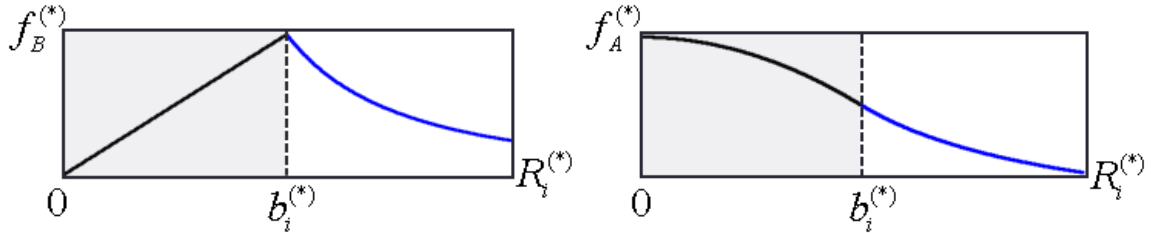


Figure 2-5 Modified scalar kernel functions at $l=l_i$

Finding active local sources

In order to characterize magnetic field efficiently, a different subset G_i of the local sources are chosen by a distance to the evaluating point \mathbf{r} and the dividing radius $d_i^{(*)}$. One of the simply ways to determine an active subset G_i is to utilize a recursive function *subsetG* with three arguments (the evaluating point \mathbf{r} , local source data structure *node*, and active subset information \mathbf{G}) to find the minimal number of local sources based on the multi-level data structure. In Figure 2.6, the *node* is a structured data related to the local source (such as $r_i^{(*)}$, $\mathbf{j}_i^{(*)}$, $d_i^{(*)}$, $b_i^{(*)}$, $l^{(*)}$, l_i and k_i) being evaluated. The process is illustrated as shown in Figure 2-6:

- The initial *subsetG* begins with desired space point \mathbf{r} , *node* at Level $l = 0$, and empty \mathbf{G} .

- At each execution, the function *subsetG* first checks for the conditions whether the distance to \mathbf{r} is larger than division radius $d_i^{(*)}$ ($|r - r_i^{(*)}| > d_i^{(*)}$) or reaches to the final division level (Level $l^{(*)} == l_i$).
 - If it is true, then the subroutine *add(G, node)* add the *node* to G .
 - If not, the subroutine *nextnode(node, k)* for $k = 1, \dots, k_i$ searches for the linked local source (denoted as *childnode*) using the data structure in Figure 2-4, and then recursively calls *subsetG* to keep adding the active local sources to the next level, Level $l^{(*)} + 1$.

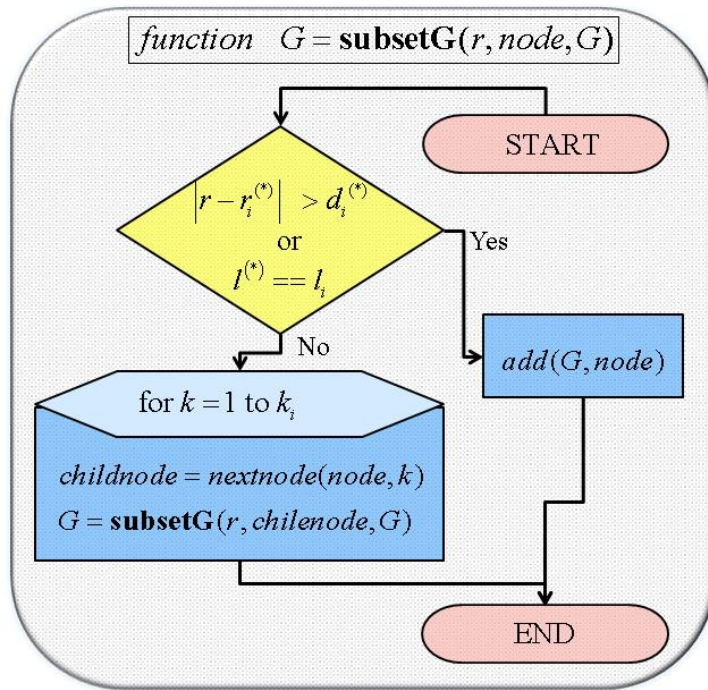


Figure 2-6 Recursive function to find active local sources

Using the local point source equations (2.24) and (2.25), the evaluation of \mathbf{B}_i and \mathbf{A}_i becomes a simple summation of $\mathbf{B}_i^{(*)}$ and $\mathbf{A}_i^{(*)}$ of local sources that belong to the active subset G_i :

$$\mathbf{A}_i(\mathbf{r}) = \sum_{(*) \in G_i} \mathbf{A}_i^{(*)}(\mathbf{r}) = \sum_{(*) \in G_i} f_A^{(*)} \mathbf{j}_i^{(*)} \quad (2.26)$$

$$\mathbf{B}_i(\mathbf{r}) = \sum_{(*) \in G_i} \mathbf{B}_i^{(*)}(\mathbf{r}) = \sum_{(*) \in G_i} \mathbf{j}_i^{(*)} \times \mathbf{e}_i^{(*)} f_B^{(*)} \quad (2.27)$$

With the point sources defined by the downward relation in (2.21), the equations of \mathbf{B}_i and \mathbf{A}_i can be written in matrix forms with only \mathbf{j}_i at Level 0:

$$\mathbf{A}_i(\mathbf{r}) = \bar{\mathbf{A}}_i(\mathbf{r}) \mathbf{j}_i \quad \text{where} \quad \bar{\mathbf{A}}_i(\mathbf{r}) = \sum_{(*) \in G_i} f_A^{(*)} s_i^{(*)} \quad (2.26)$$

$$\mathbf{B}_i(\mathbf{r}) = -[\bar{\mathbf{B}}_i(\mathbf{r})]_{\times} \mathbf{j}_i \quad \text{where} \quad \bar{\mathbf{B}}_i(\mathbf{r}) = \sum_{(*) \in G_i} \mathbf{e}_i^{(*)} f_B^{(*)} s_i^{(*)} \quad (2.27)$$

where $skew[\mathbf{a}] \triangleq \begin{bmatrix} 0 & -a_3 & a_2 \\ a_3 & 0 & -a_1 \\ -a_2 & a_1 & 0 \end{bmatrix}$ for $\mathbf{a} = [a_1 \ a_2 \ a_3]^T$; and $s_i^{(*)}$ is scalar source strength

defined by the relative ratio of source volumes or areas:

$$s_i^{(l, k_p, k)} = s_i^{(l-1, *, k_p)} / k_i \quad \text{for} \quad l = 1, \dots, l_i, \quad s_i^{(0, 1, 1)} = 1 \quad (2.28)$$

The general steps to characterize magnetic field of electro-magnetic components using the DMC are as follows.

Step 1: Decompose an electromagnetic component Ω_a into a volume (EM) or a surface (PM, iron) element.

Step 2: Determine the DMC model for all decomposed elements. For the i^{th} element, the detailed procedures are given by

- 1) choose l_i and k_i ,
- 2) choose or find the DMC geometric values $(b_i, d_i, \bar{\mathbf{r}}_i)$ from (2.20), and
- 3) find the DMC source \mathbf{j}_i at Level l , and other level values from (2.21).

Step 3: Evaluate the vector potential \mathbf{A} or magnetic field \mathbf{B} for the evaluation point \mathbf{r} by the sum of the \mathbf{A}_i and \mathbf{B}_i of all elements in Ω_a :

$$\mathbf{A}(\mathbf{r}) = \sum_{i \in \Omega_a} \mathbf{A}_i(\mathbf{r}) \quad (2.29)$$

$$\mathbf{B}(\mathbf{r}) = \sum_{i \in \Omega_a} \mathbf{B}_i(\mathbf{r}) \quad (2.30)$$

2.2.2 DMC force and torque equations

The MQS electromagnetic force \mathbf{F}_j and torque \mathbf{T}_j acting on the j^{th} element of the DMC model can be written by the Lorentz force law:

$$\mathbf{F}_j = \mathbf{j}_j \times \mathbf{B}(\bar{\mathbf{r}}_j) \quad (2.33)$$

$$\mathbf{T}_j = (\mathbf{r}_j - \mathbf{r}_0) \times \mathbf{F}_j \quad (2.34)$$

where \mathbf{B} is external magnetic field; \mathbf{j}_j and $\bar{\mathbf{r}}_j$ are the DMC source and the position of j^{th} element at Level 0; and \mathbf{r}_0 denotes the rotational center of the system. The net force \mathbf{F} and torque \mathbf{T} acting on the electromagnetic component Ω_b is the sum of distributed forces and torques:

$$\mathbf{F}(\mathbf{r}) = \sum_{j \in \Omega_b} \mathbf{F}_j, \quad \mathbf{T}(\mathbf{r}) = \sum_{j \in \Omega_b} \mathbf{T}_j \quad (2.35 \text{ a,b})$$

2.3 DMC MODEL FOR MAGNETIC MATERIALS

A DMC iron model is formulated for characterizing the effects caused by the magnetic material boundary on the electromagnetic field. Based on the decomposed surface on the material boundary, a DMC iron model can be formulated to solve for

unknown iron sources. After separating external magnetic field $\mathbf{B}^e(\mathbf{r}_i)$ into the effects caused by other iron elements $\mathbf{B}_j(\bar{\mathbf{r}}_i)$ and external sources $\mathbf{B}_{r_i}^e$ as shown in Fig 2-7, the boundary conditions (A.12) and (A.13) can be represented in the DMC form:

$$\mathbf{n}_i \bullet \mathbf{j}_i = 0 \quad (2.36)$$

$$\frac{1}{S_i \mu_i} \mathbf{T}_i [\mathbf{n}_i]_{\times} \mathbf{T}_i^T \mathbf{j}_{i*} + \mathbf{T}_i \sum_j [\bar{\mathbf{B}}_j(\bar{\mathbf{r}}_i)]_{\times} \mathbf{T}_j^T \mathbf{j}_{j*} = \mathbf{T}_i \mathbf{B}_{r_i}^e \quad (2.37)$$

where $\mathbf{j}_i = S_i \mathbf{K}_i$ from the DMC definition; coordinate transform $\mathbf{T}_i = [\mathbf{t}_{i1} \ \mathbf{t}_{i2}]^T$ is used for $\mathbf{j}_{i*} = \mathbf{T}_i \mathbf{j}_i$. For n chosen iron elements, $2n$ linear equations can be formulated using (2.37) in matrix form:

$$(\mathbf{D} + \mathbf{S}) \mathbf{j}_* = \mathbf{b}_e \quad (2.38)$$

where $\mathbf{D} = \mathbf{T} \text{Diag}(\mathbf{d}_1, \dots, \mathbf{d}_n) \mathbf{T}^T$, $\mathbf{d}_i = (S_i \mu_i)^{-1} [\mathbf{n}_i]_{\times}$, $\mathbf{T} = \text{Diag}(\mathbf{T}_1, \dots, \mathbf{T}_n)$,

$\mathbf{S} = \mathbf{T} [\mathbf{s}_1^T, \dots, \mathbf{s}_n^T]^T \mathbf{T}^T$, $\mathbf{s}_i = [[\bar{\mathbf{B}}_1(\bar{\mathbf{r}}_i)]_{\times}, \dots, [\bar{\mathbf{B}}_n(\bar{\mathbf{r}}_i)]_{\times}]$, $\mathbf{j}_* = [\mathbf{j}_{1*}^T, \dots, \mathbf{j}_{n*}^T]^T$,

$\mathbf{b}_e = \mathbf{T} [(\mathbf{B}_{r1}^e)^T, \dots, (\mathbf{B}_{rn}^e)^T]^T$, and $\text{Diag}(\bullet)$ represents a block diagonal matrix.

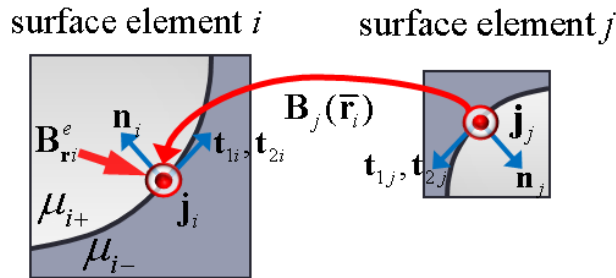


Figure 2-7 Magnetic material effects explained by DMC surface elements

With the DMC formulation for a magnetic material boundary, the overall computational load is much reduced by an order of $(2N)^2$ where N is the number of decomposed surface on the boundary. After solving (2.38) for \mathbf{j}^* , the DMC iron model in global coordinates is determined by $\mathbf{j}_i = \mathbf{T}_i^T \mathbf{j}_{i^*}$. In order to improve accuracy, modifying the resolution of geometric decomposition for every system configuration can be a tedious job. Alternatively, an element can be replaced with local sources at Level l using multi-level hierarchy. Since iron magnetization is highly dependent to external sources, one of the simple rules can be applied to choose a proper level l in terms of division radius d_i to the closest external source point \mathbf{r}_e for geometric center of the iron element $\bar{\mathbf{r}}_i$:

$$\min_l: l \geq \log_2 \frac{d_i}{|\mathbf{r}_e - \bar{\mathbf{r}}_i|} \quad (2.39)$$

In some application involving small or thin iron components, the effects caused by iron saturation need to be included in the model. Generally, the permeability of a ferromagnetic material is described by a nonlinear B-H curve (or hysteresis loop). To minimize computational load, the ferromagnetic material is assumed mainly operating near the linear region (with constant μ_i). In the case of a thin ferromagnetic material, iterative steps are conducted during analysis while treating nonlinear regions as saturated state ($\mu_{\text{sati}}=0$) which can be represented by:

$$\mathbf{j}_{\text{max}i} = (j_{\text{max}i} / j_i) \mathbf{j}_i \quad \text{if } j_i > j_{\text{max}i} \quad (2.40)$$

where $j_{\text{max}i} = S_i \mu_i B_{\text{max}}$ from (A.11); B_{max} is upper bound of magnetic field strength in the linear region; j_i denotes the magnitude of \mathbf{j}_i . During the iteration, whenever new saturation points are found, the effective strength j_i of the points is set as the maximum value (2.38), and then solved for other sources again.

2.4 DMC MODEL FOR EDDY CURRENT FORMULATION

The characterization of eddy current or current induction effects is often essential when designing electric generators, induction motors, or evaluating energy efficiency on electromagnetic actuators. Based on (2.7), a DMC model for eddy current is formulated using DMC volume elements, where the unknown eddy current can be accounted for by the decomposed volumes of the electric conductor. For an electric conductor decomposed into N volume segments, consider the i^{th} volume segment as shown on Figure 2-8 where the magnetic vector potentials of the known electromagnetic sources and the unknown eddy current on the j^{th} volume on the geometric center $\bar{\mathbf{r}}_i$ is separately represented by $\mathbf{A}_{ext}(\bar{\mathbf{r}}_i)$ and $\mathbf{A}_j(\bar{\mathbf{r}}_i)$; then, (2.7) can be written as

$$\mathbf{j}_{Ei} = -\sigma_i V_i \frac{\partial}{\partial t} \left(\mathbf{A}_{ext}(\bar{\mathbf{r}}_i) + \sum_{j=1}^N \mathbf{A}_j(\bar{\mathbf{r}}_i) \right) \quad (2.41)$$

where σ_i and V_i are the electrical conductivity and volume of the i^{th} segment.

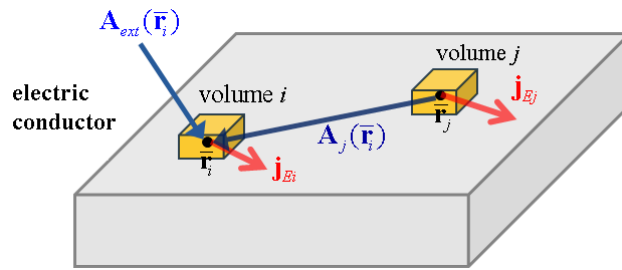


Figure 2-8 Eddy current formulation using DMC volume elements

Since the magnetic vector potential is parallel to the direction of current sources, (2.41) can be separately written by decoupled equations for orthonormal vectors. Also, using (2.28), it can be further explicitly represented by

$$\sum_{j=1}^N \left(\bar{A}_j(\bar{\mathbf{r}}_i) \frac{\partial \mathbf{j}_{Ej} \bullet \mathbf{e}_d}{\partial t} \right) = - \frac{\mathbf{j}_{Ei} \bullet \mathbf{e}_d}{\sigma_i V_i} - \sum_{j=1}^N \left(\mathbf{j}_{Ej} \bullet \mathbf{e}_d \frac{\partial \bar{A}_j(\bar{\mathbf{r}}_i)}{\partial t} \right) - \frac{\partial \mathbf{A}_{ext}(\bar{\mathbf{r}}_i) \bullet \mathbf{e}_d}{\partial t} \quad (2.42)$$

which has $3N$ unknown eddy current elements and $3N$ ODEs for $i = 1, \dots, N$ and $\mathbf{e}_d = \mathbf{e}_x, \mathbf{e}_y,$ or \mathbf{e}_z . For unknown eddy currents along \mathbf{e}_d , (2.42) can be written in matrix form:

$$\mathbf{A}\dot{\mathbf{J}} = -\mathbf{P}\mathbf{J} - \dot{\mathbf{A}}\mathbf{J} - \dot{\mathbf{A}}_{ext} \quad (2.43)$$

where $\mathbf{J} = [\mathbf{j}_{E1} \bullet \mathbf{e}_d, \dots, \mathbf{j}_{EN} \bullet \mathbf{e}_d]^T$; $\mathbf{A} = [\bar{A}_1, \dots, \bar{A}_N]$ and $\bar{A}_j = [\bar{A}_j(\bar{\mathbf{r}}_1), \dots, \bar{A}_j(\bar{\mathbf{r}}_N)]^T$; $\mathbf{P} = \text{diag}(\sigma_1 V_1, \dots, \sigma_N V_N)^{-1}$; $\mathbf{A}_{ext} = [\mathbf{A}_{ext}(\bar{\mathbf{r}}_1) \bullet \mathbf{e}_d, \dots, \mathbf{A}_{ext}(\bar{\mathbf{r}}_N) \bullet \mathbf{e}_d]^T$; $\text{diag}(\mathbf{v})$ represents a diagonal matrix formed by vector \mathbf{v} . The matrix \mathbf{A} defined by the geometric relation between decomposed volumes of electric conductors is invertible and symmetric; $\dot{\mathbf{A}}$ and $\dot{\mathbf{A}}_{ext}$ depend on the relative motion of the conductors and other sources. Generally, on the eddy current analysis of an actuator, the motion equations of a moving part can be additionally involved, which should be simultaneously solved with (2.43).

2.5 ILLUSTRATIVE EXAMPLES AND VALIDATION

For illustration, the DMC models are derived for the following four examples:

- 1) DMC volume and surface elements
- 2) Cylindrical PM and EM
- 3) Iron plate magnetized by a cylindrical PM
- 4) Eddy current induced by EMs

For all the cases, the error E evaluated at n different positions is defined by

$$E = \sum_{i=1}^n |b_i - a_i| / \sum_{i=1}^n |a_i| \quad (2.44)$$

where b_i is the data evaluated by the DMC model; and a_i represents a known value (that could be an exact solution or data obtained experimentally) as a basis for comparison. Also, the time required for computing the results using a PC (with Quad Core 2.80GHz CPU and 4G RAM) is compared against several known methods. Detailed test setups and results are discussed in each of following subsection.

2.5.1 Volume and surface elements

The DMC volume and surface element of a cubic volume source and a square surface source as shown in Figure 2-9 are simulated to illustrate trade-off between computational speed and accuracy using the local source division method, where \mathbf{e}_y denotes y-directional unit vector; J and K represent the magnitude of volume and surface current density; and j , b and d are the DMC data at Level 0.

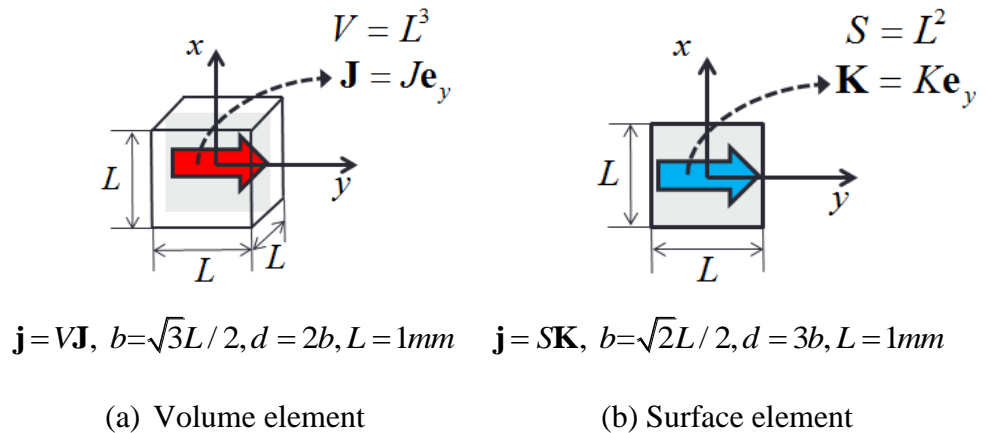


Figure 2-9 Geometry and parameters of volume and surface sources

Figure 2-10 compares the effects of the maximum division level l_i on the magnetic field B_x and the vector potential A_y of the DMC model against the exact solution using (2.14) and (2.13) over the defined 3D geometry of source domains. For each case, the magnetic field and vector potential B_x and A_y are evaluated at 41 data points on the z -axis where other directional components become zero; the error and computation time are compared in Table 2-1.

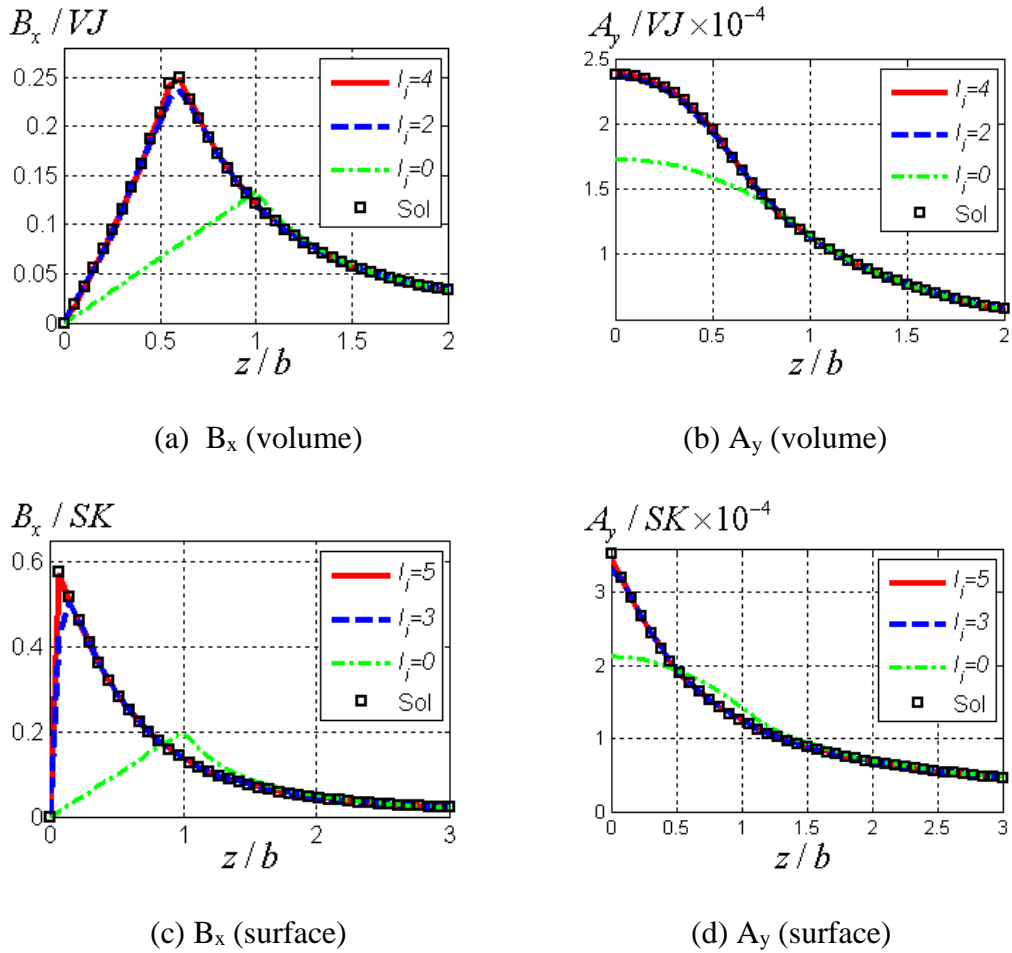


Figure 2-10 Comparison computed results by different l_i and exact solution

Table 2-1 Computation time and error for the volume and surface elements

	Maximum division level (l_i)	Error (%)		Computation Time* (sec)	
		B_x	A_y	B_x	A_y
Volume Element	0	38.58	12.96	0.0081	0.0054
	2	1.585	0.4096	0.0138	0.0108
	4	0.2289	0.0399	0.0210	0.0171
	Exact solution as basis for comparison:			2005.0	58.22
Surface element	0	57.691	13.818	0.0077	0.0128
	3	3.745	0.921	0.0139	0.0184
	5	1.239	0.635	0.0153	0.0197
	Exact solution as basis for comparison:			6.9793	1.3943

* Average computation time for 200 repetitive simulations

As the closed-form DMC field and potential equations support fast point-wise summation for all the cases as opposed to the exact solutions which are volume or surface integrals that require tedious computation. In contrast to the case without local source division ($l_i=0$) where B_x and A_y exhibit large errors within the source domains, and it clearly weakens the magnetic field inside large bounding radius using the modified kernel functions (2-23) and (2-22), the DMC-computed B_x and A_y closely match the exact solutions as the maximum division level l_i increases from 2 to 5; and within 1.25% difference with $l_i=4$ and 5. The maximum division level is a trade-off between desired computational accuracy and speed. In this research, the different maximum division levels, $l_i = 2, 3, 4$ for DMC volume and $l_i = 3, 4, 5$ for DMC surface, will be chosen.

2.5.2 Cylindrical PM and EM

For validation, the DMC models are derived for cylindrical PM and EM (commonly used in designing electromagnetic actuators). The simulated magnetic field and force using the DMC models are compared against with the results computed from

known solutions.

The geometrical properties of the PM and EM used in the simulation are shown in Figure 2-11 where l and a are the length and outer radius respectively; and c is core radius of the EM. In local cylindrical coordinates (with the origin assigned at their respective geometric center), the magnetization vector of PM and current density of EM are defined by $\mathbf{M} = M_0 \mathbf{e}_z$ and $\mathbf{J} = J_0 \mathbf{e}_\theta$ where \mathbf{e}_θ and \mathbf{e}_z represent unit vector along θ and z direction; M_0 is PM magnetization; $J_0 = NI_0 / [l(a-c)]$ is the electric current density defined by number of turns N and input current I_0 .

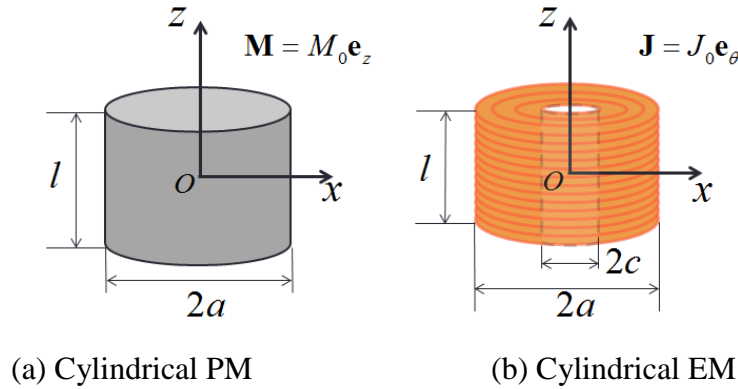
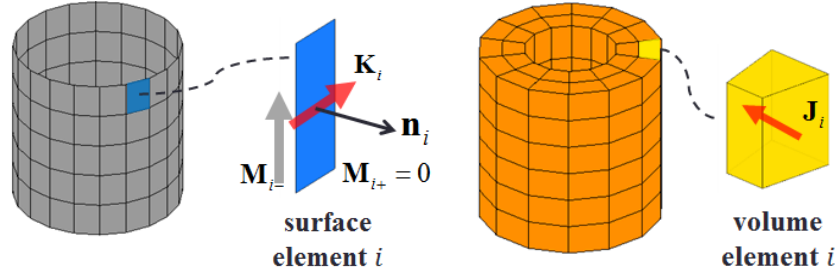


Figure 2-11 Geometry of cylindrical PM and EM

The DMC modeling starts with decomposing the geometry of PM and EM into source elements. We prefer to approximate the source domain with hexahedron volume and quadrilateral surface elements. For a constant z -magnetization, the surface current only exists on the side wall of the PM where rectangular surfaces can be used; and the EM is directly decomposed with hexahedron volumes as shown in Figure 2-12.



(a) Surface sources in a cylindrical PM (b) Volume source in a cylindrical EM

Figure 2-12 Decomposed geometries of cylindrical PM and EM

After decomposing source domain into a number of elements, the DMC sources of each element are determined by (2.45) and (2.46) and the center of hexahedron volume and quadrilateral surface can be calculated using the tetrahedron and triangle decomposition:

$$\text{(PM)} \mathbf{j}_i = \mathbf{n}_i \times (\mathbf{M}_{i+} - \mathbf{M}_{i-}) S_i = M_0 S_i \mathbf{e}_\theta \quad (2.45)$$

$$\text{(EM)} \mathbf{j}_i = J_0 V_i \mathbf{e}_\theta \quad (2.46)$$

First, the magnetic fields of the DMC PM and EM models are validated against those computed using DMP model and the exact solution (2.14). The parametric values used in this simulation are summarized in Table 2-2 where n_c and n_p denote the number of DMC at Level 0 and dipoles. For each model, B_x and B_z are evaluated at 102 data points above the top ($y=0, z=l/2+\varepsilon$) and side surfaces ($x=a+\varepsilon, y=0$). Figure 2-13 and 2-14 compare the computed B_x and B_z , and Table 2-3 compares the error against the solution and the required computational time for each model.

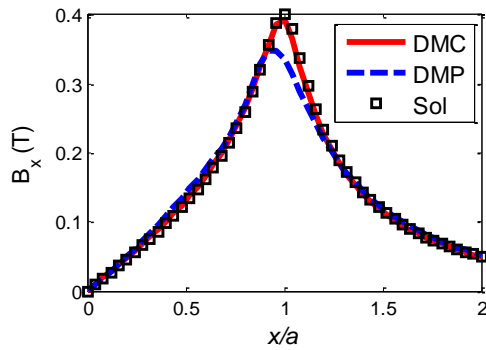
For all the cases, the DMC-based magnetic fields agree well with the solutions. Due to the modified dipole distance, some errors around side surface were found in the DMP model. Both the DMC and DMP models support fast computation with the field

equations in closed form; but the DMC model takes a bit more computation time than the DMP model due to the addition of local sources.

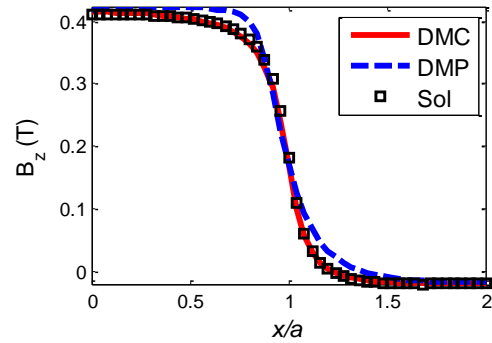
Table 2-2 Simulation parameters for the magnetic field validation

	Geometry (mm)				DMC			DMP		
	$l(\text{mm})$	$2a/l$	c/a	$\varepsilon(\text{mm})$	n_c	l_i	d_i/b_i	n_p	n	K
PM	12.77	1	0	0.5	100	4	3	19	6	3
EM	9.53	1	0.5	0.5	112	3	2	73	12	6

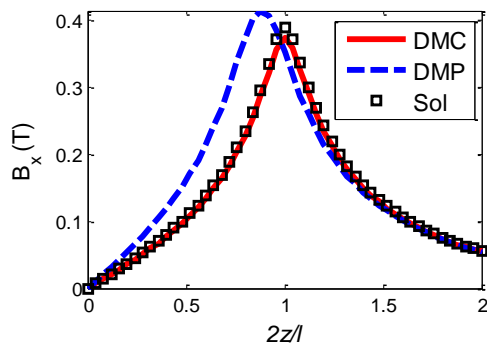
* $\mu_0 M_0 = 1\text{T}$, 221 turns with 1A Current



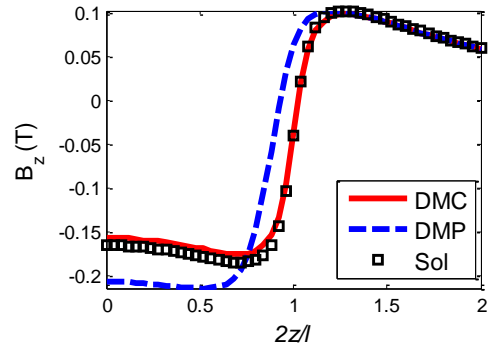
(a) B_x above top surface



(b) B_z above top surface

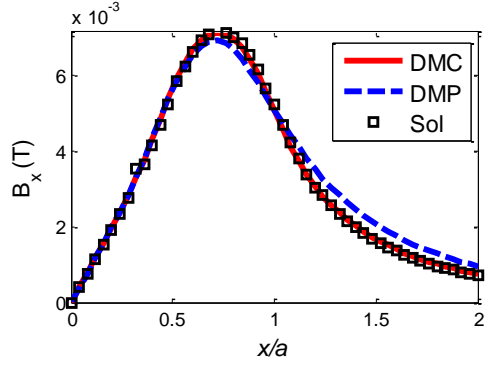


(c) B_x above side surface

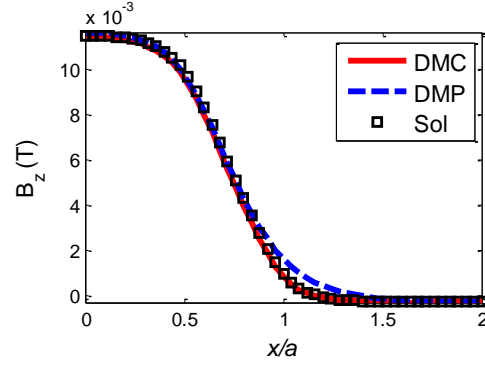


(d) B_z above side surface

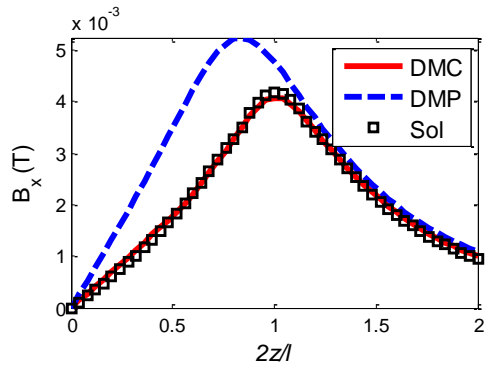
Figure 2-13 Computed magnetic fields nearby the cylindrical PM



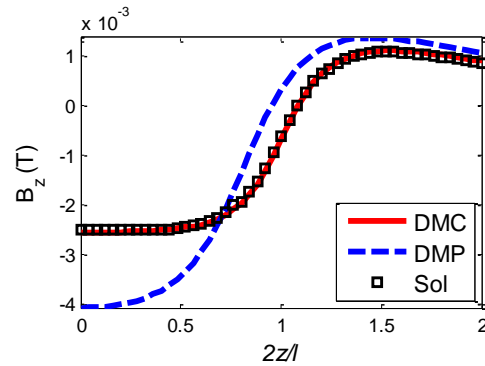
(a) B_x above top surface



(b) B_z above top surface



(c) B_x above side surface



(d) B_z above side surface

Figure 2-14 Computed magnetic fields nearby the cylindrical EM

Table 2-3 Computation time and error for the PM and EM

		Error (%)		Computation Time* (sec)
		B_x	B_z	
PM	DMC	2.653	5.842	0.0492
	DMP	15.61	28.93	0.0186
	Solution	0	0	5.9045
EM	DMC	2.044	4.402	0.0465
	DMP	18.65	26.16	0.0165
	Solution	0	0	6.6275

* Average computation time for 100 simulations of DMC and DMP model

Next, the electromagnetic force between the cylindrical PM and EM is validated numerically by comparing against results computed using DMP models and published experimental data [63]. Two test setups (denoted by Large and Small) are shown in Figure 2-15, and the simulation parameters for DMC and DMP model are summarized in Table 2-4. For each setup, the computed axial forces are compared against experimental forces in Figure 2-16. Also for each method, the error (relative to the experimental force) and required time to compute 52 data points are compared in Table 2-5.

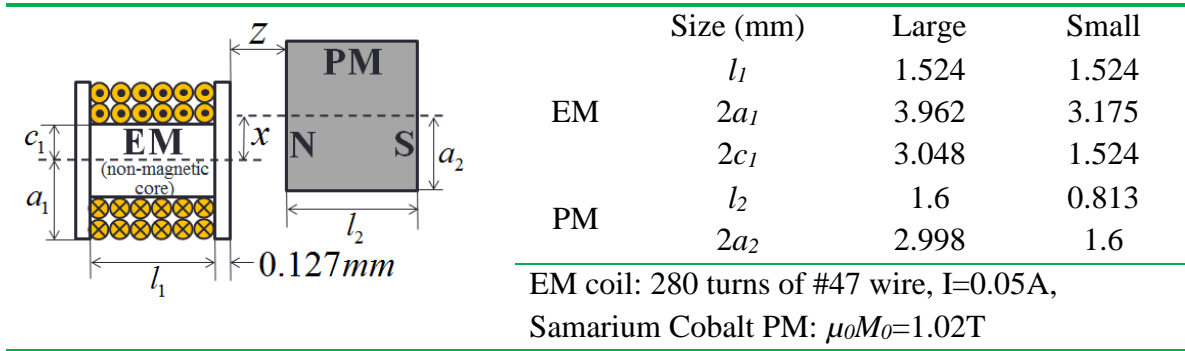


Figure 2-15 Experimental setup and parameters [63]

Table 2-4 Simulation parameters for the force validation

		DMC			DMP [27]		
		n_c	l_i	d_i/ b_i	n_p	N	K
Large	PM	114	4	3	13	6	2
	EM	72	3	2	97	12	8
Small	PM	117	4	3	13	6	2
	EM	80	3	2	25	8	3

As shown in Figure 2-16, the DMC force computation agrees well with large experimental setup while the DMP shows better accuracy for the small test case. The DMC force is always larger than DMP force, and closely agrees with the computation

results by other numerical method in [1]. Comparing with the DMP model, the DMC model requires a bit more computational effort.

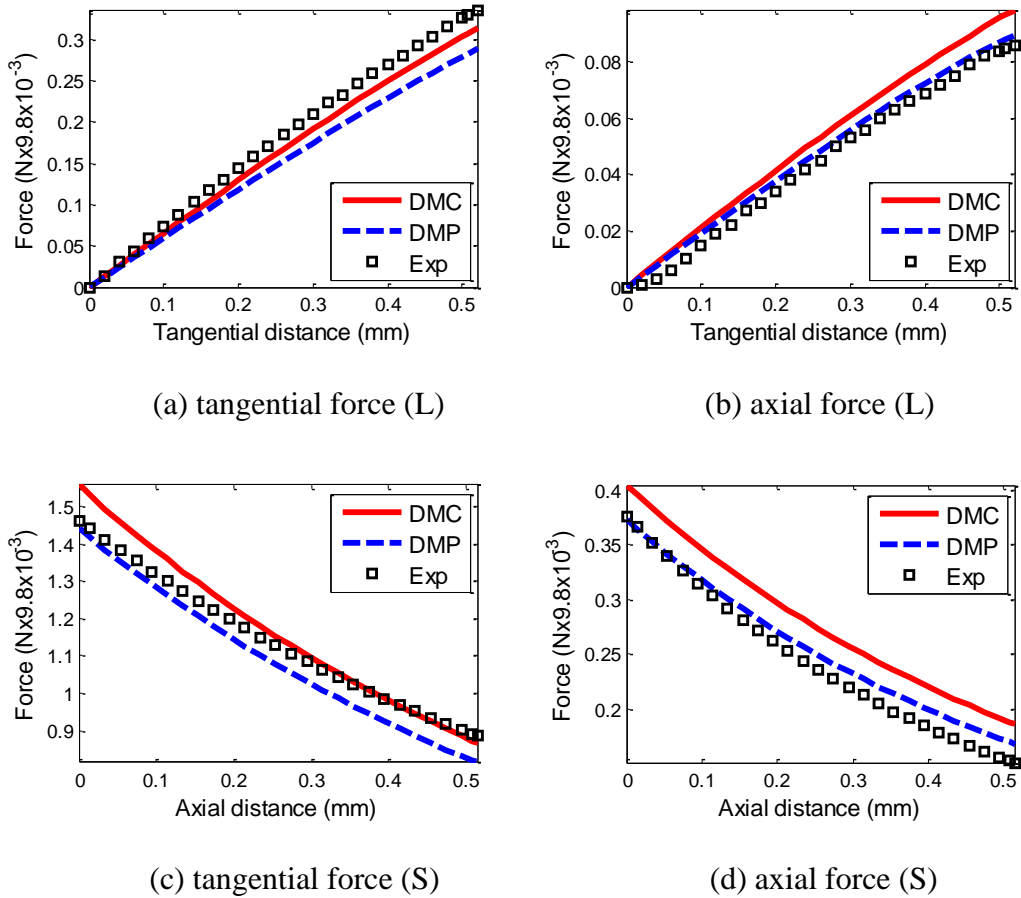


Figure 2-16 Computed force and experimental data of cylindrical EM and PM

Table 2-5 Computation time and error for the force validation

		Error (%)		Computation Time* (sec)
		Tangential	Axial	
Large	DMC	7.65	3.30	1.989
	DMP	15.94	4.38	0.2904
Small	DMC	14.79	17.59	2.381
	DMP	7.39	4.94	0.1404

* Average computation time for 20 simulations of DMC and DMP model

2.5.3 Iron plate and cylindrical PM

The DMC iron model is applied to analyze an iron plate magnetized by a cylindrical PM, and validated against known data. Figure 2-17 shows two test setups (with different gaps and thicknesses) along with parametric values used for validating the DMC iron model magnetized by a cylindrical PM.

- The gap setup compares the attraction force to test the magnetization effects (without saturation) for different z distances between the PM and thick steel plate.
- The thickness setup compares the adhesion force to investigate the magnetization effects (with saturation) on steel-plate thickness.

Figure 2-18 compares the simulated forces of the DMC models to published experimental data [65], FEA, and results obtained using an image method with DMP [28]. A time comparison for different numerical methods is given in Table 2-6.

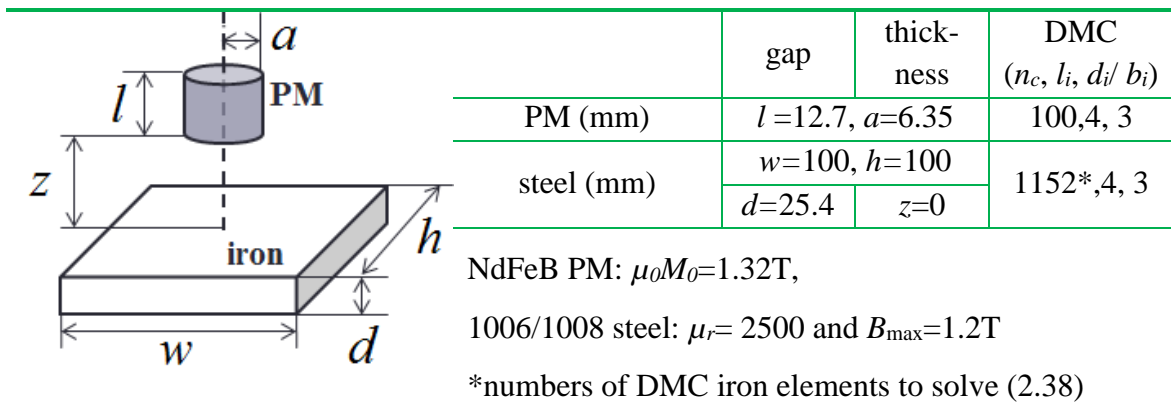


Figure 2-17 Iron test setup and parameters

For each case, the force computed by the DMC iron model very closely agrees with FEA and experimental data. The image method accurately analyzes the large and

thick steel plate in the gap setup with idealized boundary model but fails to explain saturation for the thin steel plates. As shown in Table 2-6, the DMC iron model significantly reduces the computational effort as compared to FEA. The DMP-image method [28], which exhibit the best computational speed, is only limited to the simple and idealized iron shapes such as plain or circular surfaces. The results of the thickness test setup in Figure 2-18(b) shows that saturation occurs only for thin iron. The effect caused by iron saturation will not be considered in the subsequent chapters for irons with sufficiently large thickness.

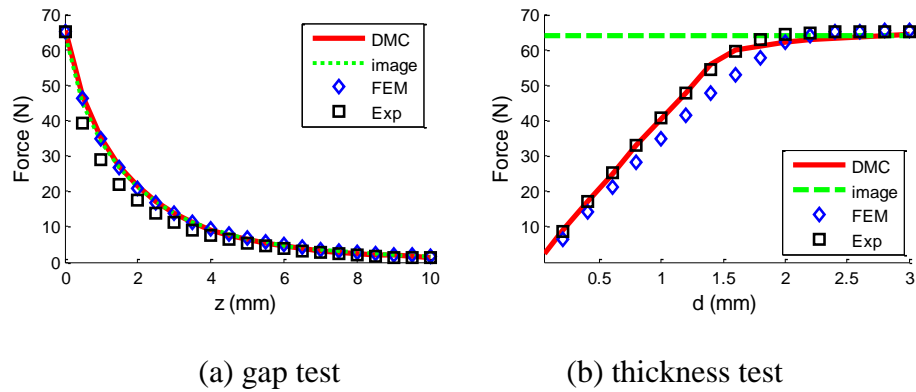


Figure 2-18 Force comparison between cylindrical PM and iron plate

Table 2-6 Computation time for the iron plate and cylindrical PM

Method	DMC	FEM	Image
Computation Time	24.95s	1h 32m 16s	0.47s

2.5.4 Eddy current induced by EMs

The DMC eddy current model is applied to analyze the levitation of a cylindrical aluminum plate by two concentrically located cylindrical EMs. With oppositely-directed sinusoidal current inputs, the eddy current appears on the aluminum plate, and forms a

levitation force with the magnetic fields of the EMs. The schematics in Figure 2-19 illustrated the design and parameters involved. To validate the effects of the DMC model on the eddy current analysis, the simulated transient responses of this coupled electromechanical system are compared against measured experimental result [64].

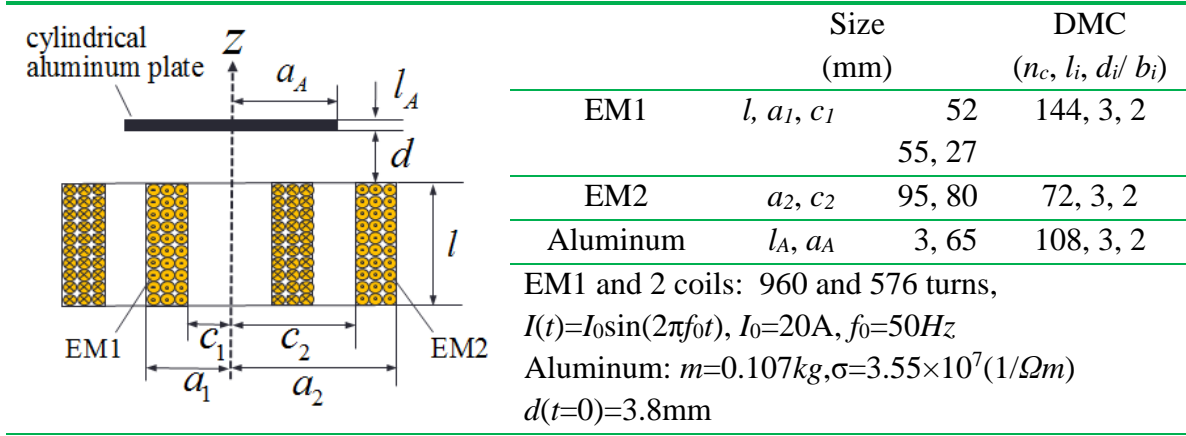


Figure 2-19 Eddy current test setup and parameters [64]

After modeling the EMs and aluminum plate with DMC elements, the eddy current equations formulated by (2.43) are used to solve equations of motion of the aluminum plate along z-axis:

$$m\ddot{d} = f_z - mg \quad (2.47)$$

where f_z denotes a levitation force computed by (2.29); g is the acceleration of gravity ($9.8m/s^2$). In this analysis, we do not consider eddy current on current controlled EMs; decomposed volumes of the electric conductor have no relative motion since the aluminum plate is single rigid body, which makes $\dot{\mathbf{A}} = 0$ in (2.43). While this simulation can be further simplified with axis-symmetric geometry, a 3D analysis is performed to validate the general eddy current formulation.

The transient response was solved using a stiff ODE solver which took 27 minutes and 37 seconds for the first 1.5s computation. Figure 2.20 shows the simulation result by DMC well matches with the published experimental response, and DMC model for eddy current offers efficient ways to analyze time dependent response of an electromagnetic actuator.

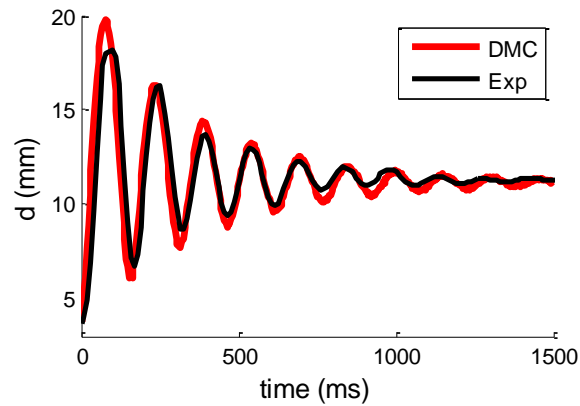


Figure 2-20 Simulated levitation height and measured data

2.6 SUMMARY

A general DMC modeling method based on multi-level current sources has been presented for characterizing electric current and magnetic material for design analysis of an electromagnetic actuator. This method, which extends the existing DMP method for analyzing general magnetic material effects, provides a direct means to model electromagnetic components with electric and magnetizing currents on decomposed geometries. Along with closed-form magnetic field and force equations (represented by an active multi-level local sources), DMC models has been applied to characterize the effects of PM, EM, iron, and eddy current, and verified by comparing other simulated results against DMP, FEA, exact solutions or published experimental data. On the

development of DMC models for iron, constitutive equations are formulated in terms of local point sources that improve the accuracy of solution without geometry refinement.

This simple and fast multi-level modeling method, which directly converts the geometry and sources of an electromagnetic component into spatial distribution of point currents, will be utilized to characterize various electromagnetic actuators in Chapter 5 including 3-DOF spherical motor. Furthermore, the DMC defined by decomposed geometries can offer an efficient way to topologically optimize initial designs of electromagnetic actuators; its detail will be given in next chapter.

CHAPTER 3

DMC BASED ACTUATOR LAYOUT OPTIMIZATION

This Chapter offers an effective optimization method (referred to here as Layout Optimization) based on the DMC model to determine the “best or most preferred” design of a rotary actuator. The remainder of this Chapter begins with an overview of Layout Optimization. Next, a linear topology is formulated for optimizing the PM layout. Finally, the Layout Optimization is illustrated with two 2D examples; 1-DOF rotary motor and 2-DOF orientation stage. While the Chapter illustrates the method in the context of a rotary actuator, it can be readily extended to other general PM-based actuators such as output force optimization of a linear motor.

3.1 OVERVIEW OF LAYOUT OPTIMIZATION

The objective of Layout Optimization is to maximize the torque output of a PM-based rotary actuator with a predefined EM layout for an optimized PM shapes. Layout Optimization offers an efficient way to find the best shape and repetitive patterns of EM and PM. Without loss of generality, the design optimization is simplified with the following conditions for clarity of illustrating the concept:

- 1) PMs and EMs are equally spaced in repetitive patterns. For a rotary actuator, the symmetric properties of the PM/EM arrangement about its rotational center are often used to cancel out undesired radial forces that tend to increase friction.

- 2) The axes of the EM cores are radially directed towards the rotor center; in other words, they are always perpendicular to the rotor rotation so that the strongest magnetic field around the core is utilized.
- 3) Eddy current is not considered in optimization. To support this condition, electric current inputs (instead of voltage inputs) are used.
- 4) Only the rotor PM configurations are topologically optimized for the predefined stator EMs (with air-cored windings or slotted non-magnetic core). While the optimization is illustrated with designing the rotor PM, it can be easily extended to optimizing a stator EM design for a defined rotor PM design.

3.1.1 Topology optimization of a PM actuator

An objective of topology optimization is to find the best material distribution of a design space such that maximizes (or minimizes) objective quantity for specified non-design space conditions and constraints.

Formulation of topology optimization

To optimize a rotor PM configuration, the PM magnetizations \mathbf{M} of rotor 3D design space (decomposed by N_v volumes) are defined by a volume density vector:

$$\mathbf{M} = M_{\max} \boldsymbol{\rho} \quad (3.1)$$

where $\boldsymbol{\rho} = [\boldsymbol{\rho}_{(1)}^T \cdots \boldsymbol{\rho}_{(i)}^T \cdots \boldsymbol{\rho}_{(N_v)}^T]^T$; the material density vector of the $(i)^{\text{th}}$ PM volume $\boldsymbol{\rho}_{(i)}$ is defined in (B.2); and M_{\max} is the maximum magnetization of the rotor PM. For a PM actuator with the stator EM in non-design space, a distribution of the rotor PM in the

design space is topologically optimized to maximize the weighted sum of the electromagnetic torque τ_p over a specified range of its rotor position \mathbf{r}_p :

$$\text{maximize}_{\rho} \sum_p |\mathbf{c}^T \boldsymbol{\tau}_p| \text{ subjected to } |\boldsymbol{\rho}_{(i)}| \leq 1 \quad (3.2)$$

where $\mathbf{c} = [w_x \ w_y \ w_z]^T$; w_x , w_y and w_z denote weight factors for x, y and z directional torques respectively; $\boldsymbol{\rho}_{(i)}$ is subjected to a nonlinear constraint $|\boldsymbol{\rho}_{(i)}| \leq 1$. With N_s surface elements belonging to the boundary of N_V PM design volumes, the $(k)^{\text{th}}$ PM surface source $\mathbf{j}_{(k)}$ can be described by \mathbf{M} (or $\boldsymbol{\rho}$) using (2.5), and the torque $\boldsymbol{\tau}_p$ in (3.2) can be represented by the sum of the torque on the $\mathbf{j}_{(k)}$ located at $\mathbf{r}_{(k)}$:

$$\boldsymbol{\tau}_p = \sum_{k=1}^{N_s} \mathbf{r}_{(k)} \times \mathbf{j}_{(k)} \times \left[J(p) \bar{\mathbf{B}}_p(\mathbf{r}_{(k)}) \right] \quad (3.3a)$$

or a linear matrix form in terms of $\mathbf{j}_{(k)}$:

$$\boldsymbol{\tau}_p = J_p \sum_{k=1}^{N_s} \text{skew}(\mathbf{r}_{(k)}) \text{skew}(\bar{\mathbf{B}}_p(\mathbf{r}_{(k)})) \mathbf{j}_{(k)} \quad (3.3b)$$

where $\bar{\mathbf{B}}_p$ is the magnetic field formed by a stator EM with an unit current input density; and $J(p)$ is the EM current input at rotor position \mathbf{r}_p . Due to the discontinuity in the 1st order derivative caused by the absolute value operation, it is difficult to solve (3.2) directly for an optimal solution. To remove the absolute value operator, the EM current input $\mathbf{J}_{EM} = [J(1) \cdots J(p) \cdots J(P)]^T$ is treated as an additional optimization variable:

$$\text{maximize}_{\rho, \mathbf{J}_{EM}} \sum_p \mathbf{c}^T \boldsymbol{\tau}_p \text{ subjected to } |\boldsymbol{\rho}_{(i)}| \leq 1 \quad (3.4)$$

But, now (3.4) requires many iterations, and easily converges to local maximums due to the nonlinearity caused by the multiplication of $\mathbf{j}_{(k)}$ (depending on $\boldsymbol{\rho}$) and $J(p)$. While $\mathbf{j}_{(k)}$ depends on the PM density vector $\boldsymbol{\rho}$, unknown $J(p)$ depending the rotor position and nonlinear constraint $|\boldsymbol{\rho}_{(i)}| \leq 1$ mainly exhibit nonlinearity or convergence issue.

3.1.2 Linearization of topology optimization

To resolve described nonlinearity or local convergence problems, the topology optimization will be converted into linear programming using electric current specification and alternative linear constraint. Details descriptions are as follows.

Electric input current specification

Once an electric input current can be predefined before solving an optimization problem, then the objective function in (3-4) can be expressed by a linear function over the material density vector $\boldsymbol{\rho}$ using DMC model (described in Chapter 3.2). The magnitude of the EM input current becomes the maximum EM input current J_{\max} to maximize the objective function, and it defines the EM current input in a square wave form. The sign of EM input current $J(p)/J_{\max}$ depends on the relative position p and polarities of the nearby PMs.

For the electric input current specification, the shapes of the PM and EM are not necessary, but the center position of each PM polarity, referred to PM pole position, should be known to change the sign of the input current. Figure 3-1 illustrates how the electric input current can be specified to increase the x -directional output force f_x for the

given cylindrical EMs and PMs. For different EM positions, the EM inputs that increase f_x becomes the square wave changing its sign by the polarities of the nearby PMs.

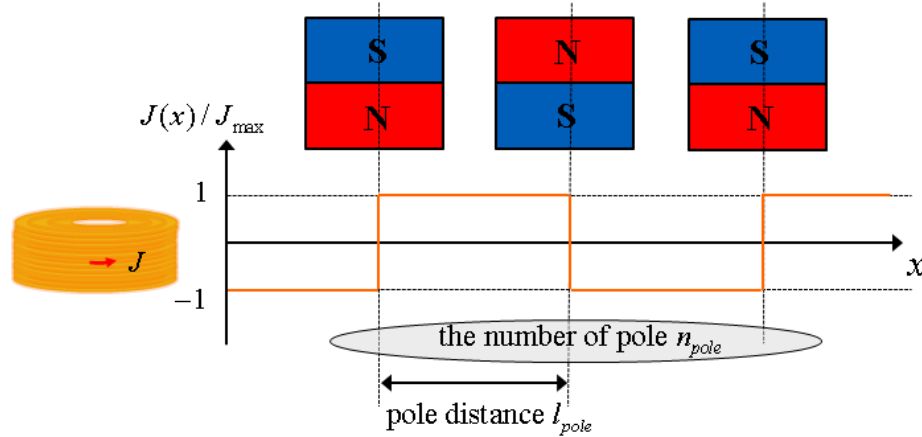


Figure 3-1 EM input currents defined by PM pole patterns

Assuming that PM poles are equally spaced in repetitive patterns (as described in the beginning of this chapter), different number of PM poles n_{pole} or distance between PM poles l_{pole} is used to define a number of PM pole positions; it generates linear optimization cases with many different electric input current specifications. n_{pole} and l_{pole} are effective to define PM pole positions for close and open ended design space respectively. In this thesis, the closed and opened ends in the rotor design space are defined as follows:

- Closed design space is axis-symmetric about its rotational axis. Most of continuous spinning motors are designed by the closed rotor. In the closed rotor design space, the PM poles are equally spaced by $2\pi/n_{pole}$ for different $n_{pole} = 2, 3, \dots$.

- Opened design space is for the design of many kinds of actuators having a limited range of motion such as a linear motor or orientation stage. PM poles can be equally spaced by different l_{pole} starting from the base position like a geometric center or default position of the rotor design space.

In Chapter 3.4, detailed description of the electric input current specification will be presented for optimizations of 1-DOF rotary motor and 2-DOF orientation stage to respectively define PM pole positions by n_{pole} and l_{pole} .

Linear constraints on a design variable

In the view of the material mixture of PMs magnetized along x, y, and z axis, the PM material density variable defined by 6 positive density variables in (B.1) requires following 12 lower and upper boundary constraints:

$$0 \leq \bar{\rho}_{(i)} \leq 1 \quad (3.5)$$

, and the material density vector $\boldsymbol{\rho}_{(i)} = \bar{\mathbf{I}}_{\rho} \bar{\boldsymbol{\rho}}_{(i)}$ in (B.2) gives a nonlinear constraint to limit its magnitude by

$$\boldsymbol{\rho}_{(i)}^T \boldsymbol{\rho}_{(i)} \leq 1. \quad (3.6)$$

The feasible domain of (3.6) becomes the inner space of a unit sphere; it can represent any directions of $\mathbf{M}_{(i)}$. Considering difficulties on fabricating continuously changing PM magnetization (and also far from preferred practical actuator designs), the nonlinear constraint can be alternatively described by a following linear constraint to limit the sum of the positive density variables:

$$\|\bar{\boldsymbol{\rho}}_{(i)}\|_1 \leq 1 \quad (3.7)$$

or

$$\mathbf{u}_\rho^T \bar{\boldsymbol{\rho}}_{(i)} \leq 1 \quad (3.8)$$

where $\mathbf{u}_\rho^T = [1 \ 1 \ 1 \ 1 \ 1 \ 1]$ sums 6 positive density variables. The linear constraint (3.7) softly penalizes the maximum magnitude of PM mixtures by less than one, and softly forces $\boldsymbol{\rho}_{(i)}$ to converge one of PMs magnetized along the local coordinate during the optimization. Figure 3-2 compares the feasible solution set of (3.6) and (3.7) for a 2D case. While the nonlinear solution set (denoted by dotted circle) fully supports unit magnitude of $\boldsymbol{\rho}_{(i)}$ for any direction, diamond-shaped linear solution set only allows along x or y axis.

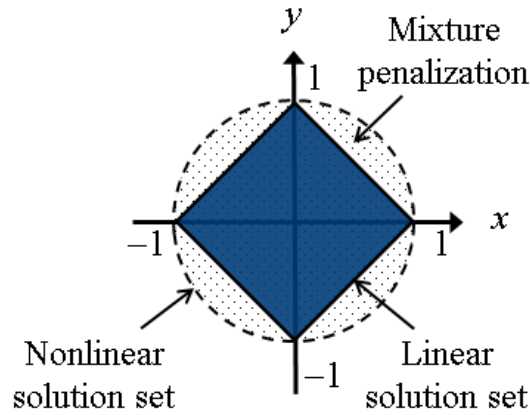


Figure 3-2 Solution set with nonlinear and linear constraints

The local coordinates for each design volume can be assigned by many different ways depending on the specifications of the actuator design. In this thesis, the local

coordinate is defined by parallel and perpendicular directions of desired actuator motions to effectively represent Halbach PM configuration.

3.1.3 Layout Optimization

Linearized topology optimization offers an efficient design method, referred here as Layout Optimization, to find an optimized EM and PM shapes, and its respective pole positions in the stator and rotor space. The flowchart in Figure 3-3 illustrates the Layout Optimization process consisting of predefining steps for 1) EM layout and 2) PM poles, two optimization steps: 3) linear optimization and 4) integer programming, and post processing for 5) optimized EM and PM layouts. Detailed description of each step is as followings:

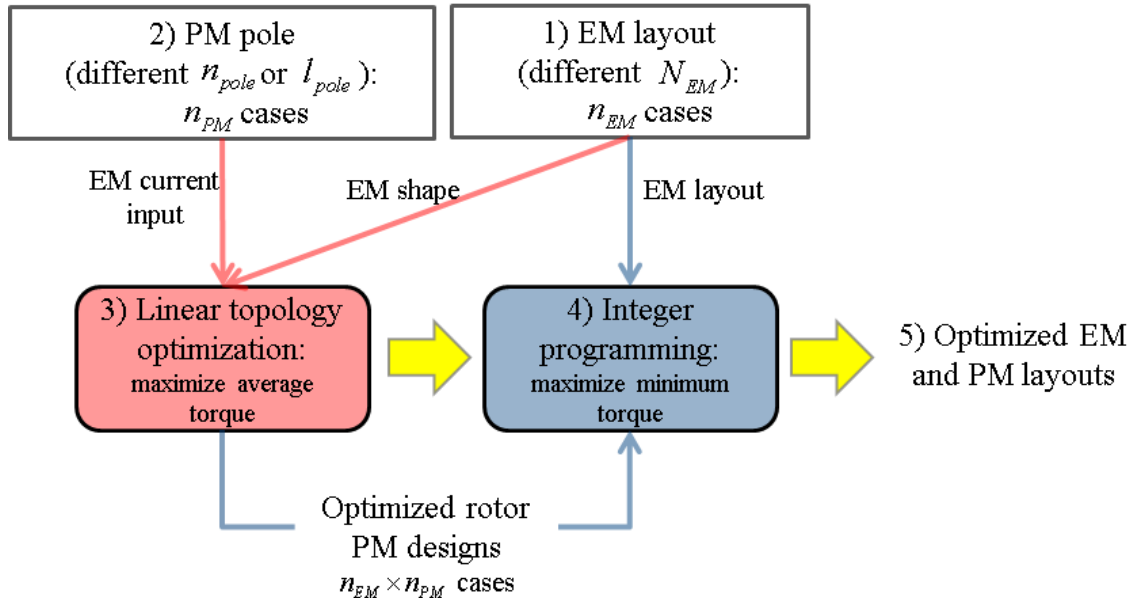


Figure 3-3 Flow chart of Layout Optimization

1, 2) EM layout and PM pole specification

n_{EM} possible EM layouts and n_{PM} PM pole patterns are configured leading to $n_{EM} \times n_{PM}$ cases of linearized design problems to be optimized by the Layout optimization. While varying the number n_{pole} or length l_{pole} of the rotor PM pole, the PM pole patterns are defined to predefine an electric input current for the range of rotor positions. Assuming that a non-design space stator is fully filled with same sized EMs, EM positions can be specified by different numbers of the EMs N_{EM} ; and its respective EM size is also defined by S_{stator} / N_{EM} where S_{stator} denotes the stator size along the moving direction to be optimized.

3) Linear topology optimization

For each case of the $n_{EM} \times n_{PM}$ specifications, linear topology optimization determines the best rotor PM design to maximize torque average. While solving the linear optimization by a SIMPLEX method, the signs of the electric input current of an EM along the rotor orientations clearly shape a PM configuration with the predefined PM pole pattern in the way to increase the output torque; and it prevents the solution converging to undesired checker board patterns.

4) Integer programming

By exploiting fast computational speed of the DMC model, the net output torques of the N_e EMs for linearly optimized rotor PM designs are evaluated to determine an optimized design; and various design objectives can be imposed on this integer programming step. In this research, the criteria to evaluate a design optimality is set to maximize minimum torque considering design compactness such as the number of EMs

or PMs; and the best or preferred PM and EM layouts are determined by the evaluated design optimality.

5) Optimized EM and PM layouts

To fabricate an optimized actuator design with commercially available products like standard sized PMs, optimized EM and PM layouts are polished into a simpler design. Starting from the optimized EM and PM layouts, optional optimization steps can be applied to further optimize the shape of the rotor PM while investigating the effects of different rotor weight or weight factors for moving directions on net output torque.

3.2 LINEAR TOPOLOGY OPTIMIZATION

As a part of layout optimization, a linear optimization of the rotor PM can be formulated for predefined EM shape and PM poles. Consider the rotor design space decomposed by N_v PM design volumes and its N_s surface elements. After describing the DMC torque with a $6N_v \times 1$ rotor PM design variable $\bar{\mathbf{p}} = [\bar{\mathbf{p}}_{(1)}^T, \dots, \bar{\mathbf{p}}_{(i)}^T, \dots, \bar{\mathbf{p}}_{(N_v)}^T]^T$ where $\bar{\mathbf{p}}_{(i)}$ is defined by 6 positive material density variables in APPENDIX B, the linear topology optimization will be expressed in the canonical form to maximizing weighted average of the torque evaluated at P different rotor orientations:

$$\underset{\bar{\mathbf{p}}}{\text{maximize}} \mathbf{w}^T \mathbf{T}_{PM} \bar{\mathbf{p}} \text{ subjected to } \|\bar{\mathbf{p}}_{(i)}\|_1 \leq 1, \mathbf{u}_\rho^T \bar{\mathbf{p}}_{(i)} \leq 1 \quad (3.9)$$

where $3P \times 6N_v$ torque matrix $\mathbf{T}_{PM} = [\mathbf{T}_1^T \cdots \mathbf{T}_p^T \cdots \mathbf{T}_P^T]^T$ computes the torque $\boldsymbol{\tau} = [\boldsymbol{\tau}_1^T \cdots \boldsymbol{\tau}_p^T \cdots \boldsymbol{\tau}_P^T]^T$ at all rotor orientation using the PM volume density variable $\bar{\boldsymbol{\rho}}$; $\mathbf{u}_\rho^T = [1 \ 1 \ 1 \ 1 \ 1 \ 1]$; and the linear constraints are described in (3.5) and (3.8).

In (3.9), $3P \times 1$ normalized weight vector $\mathbf{w} = \mathbf{w}_p / \|\mathbf{w}_p\|_1$ do a weight sum of the torque $\boldsymbol{\tau}$, and it gives a scalar value to be maximized during the linear optimization. The weight vector $\mathbf{w}_p = [w_1 \mathbf{w}_d^T, \dots, w_p \mathbf{w}_d^T \cdots, w_P \mathbf{w}_d^T]^T$ is defined by weight factor w_p at actuator orientation p and weight factors $\mathbf{w}_d = [w_x \ w_y \ w_z]^T$ for three moving directions. For example, $w_x = w_y = 0$ and $w_z = 1$ is used for designing a rotary motor spinning for z-axis; $w_p = 1$ for $p = 1, \dots, P$ if all rotor orientations have same significance.

In following subsection, the formulation of \mathbf{T}_{PM} and \mathbf{J}_{PM} by the DMC model is presented for the rotor PM design variable $\bar{\boldsymbol{\rho}}$ including a rotor iron boundary; and \mathbf{F}_{PM} $3P \times 3N_s$ force matrix \mathbf{F}_{PM} is additionally presented to solve a force-based design optimization:

$$\underset{\bar{\boldsymbol{\rho}}}{\text{maximize}} \quad \mathbf{w}^T \mathbf{F}_{PM} \bar{\boldsymbol{\rho}} \quad \text{subjected to} \quad \|\bar{\boldsymbol{\rho}}_{(i)}\|_1 \leq 1, \mathbf{u}_\rho^T \bar{\boldsymbol{\rho}}_{(i)} \leq 1 \quad (3.10)$$

3.2.1 Surface current equations

Consider a $(k)^{\text{th}}$ PM surface (with surface area $S_{(k)}$ and unit normal vector $\mathbf{n}_{p(k)}$) exists between the $(i)^{\text{th}}$ and $(j)^{\text{th}}$ PM volumes as shown in Figure 3-4(a); and it gives DMC surface current $\mathbf{j}_{p(k)}$ at an orientation p using (2.5):

$$\mathbf{j}_{p(k)} = S_{(k)} \mathbf{n}_{p(k)} \times (\mathbf{M}_{p(j)} - \mathbf{M}_{p(i)}) \quad (3.11)$$

Using (B.5), $\mathbf{j}_{(k)}$ is also defined by a design variable $\bar{\mathbf{p}}_{(i)}$:

$$\mathbf{j}_{p(k)} = M_{\max} S_{(k)} \text{skew}(\mathbf{n}_{p(k)}) (\bar{\mathbf{G}}_{p(j)} \bar{\mathbf{I}}_{\rho} \bar{\mathbf{p}}_{(j)} - \bar{\mathbf{G}}_{p(i)} \bar{\mathbf{I}}_{\rho} \bar{\mathbf{p}}_{(i)}) \quad (3.12)$$

where $\bar{\mathbf{G}}_{p(j)}$ is a transformation matrix from the local coordinate to the global coordinate at the orientation p ; and $\mathbf{M}_{p(j)}$ (or $\bar{\mathbf{G}}_{p(j)}$) is set to zero when $(k)^{\text{th}}$ PM surface contacted to the $(j)^{\text{th}}$ volume in a non-design space (such as air or rotor iron). With $3 \times 3N_V$ matrix $\mathbf{G}_{p(k)} = [\mathbf{O}_3 \cdots \mathbf{O}_3 \bar{\mathbf{G}}_{p(j)} \mathbf{O}_3 \cdots \mathbf{O}_3 - \bar{\mathbf{G}}_{p(i)} \mathbf{O}_3 \cdots \mathbf{O}_3]$ to describe a geometric relation between $(i)^{\text{th}}$ and $(j)^{\text{th}}$ PM volumes and its $(k)^{\text{th}}$ PM surface leading to the relationship (3.13) between $\bar{\mathbf{p}}$ and $\mathbf{j}_{p(k)}$:

$$\mathbf{j}_{p(k)} = \mathbf{J}_{p(k)} \bar{\mathbf{p}} \quad (3.13)$$

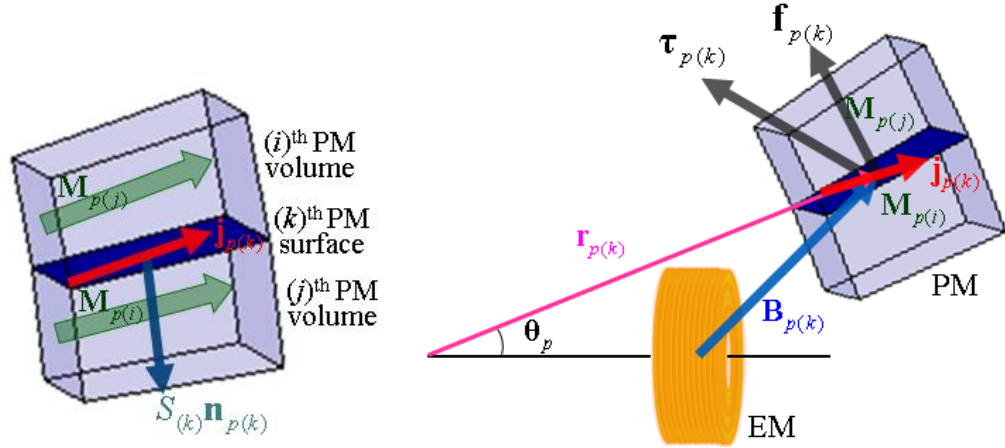
where $\mathbf{J}_{p(k)} = M_{\max} S_{(k)} \text{skew}(\mathbf{n}_{p(k)}) \mathbf{G}_{p(k)} \mathbf{I}_{\rho}$; \mathbf{O}_3 is 3×3 zero matrix; and

$$3N_V \times 6N_V \quad \mathbf{I}_{\rho} = \begin{bmatrix} \bar{\mathbf{I}}_{\rho} & \mathbf{O} \\ \vdots & \ddots \\ \mathbf{O} & \bar{\mathbf{I}}_{\rho} \end{bmatrix} . \quad \text{Then, combining (3.13) for all surface}$$

currents $k = 1, \dots, N_S$, gives the linear relation between \mathbf{j}_p and $\bar{\mathbf{p}}$ by:

$$\mathbf{j}_p = \mathbf{J}_p \bar{\mathbf{p}} \quad (3.14)$$

where $\mathbf{j}_p = [\mathbf{j}_{p(1)}^T, \dots, \mathbf{j}_{p(N_S)}^T]^T$ and $\mathbf{J}_p = [\mathbf{J}_{p(1)}^T, \dots, \mathbf{J}_{p(N_S)}^T]^T$.



(a) PM volumes and its surface

(b) force and torque on a rotor PM surface

Figure 3-4 Force and torque on a rotor PM surface at the orientation θ_p

3.2.2 Force and torque equations

Considering an EM and PM design volumes assembled by a relative orientation θ_p as shown in Figure 3-4(b), the force $\mathbf{f}_{p(k)}$ and torque $\boldsymbol{\tau}_{p(k)}$ acting on the surface current $\mathbf{j}_{p(k)}$ located at $\mathbf{r}_{p(k)}$ can be written by DMC force and torque equations in (2-31) and (2-32):

$$\mathbf{f}_{p(k)} = -\text{skew}(\mathbf{B}_{p(k)})\mathbf{j}_{p(k)}, \quad \boldsymbol{\tau}_{p(k)} = \text{skew}(\mathbf{r}_{p(k)})\mathbf{f}_{p(k)} \quad (3.15a, b)$$

where $\mathbf{B}_{p(k)} = J(\theta_p)\mathbf{b}_{p(k)}$ is defined by the flux density of the EM with a unit current input at $\mathbf{r}_{p(k)}$ multiplied by a predefined EM electric input current $J(\theta_p)$ at the orientation θ_p . Combining all surface currents $k=1, \dots, N_s$, the summation of the force and torque, \mathbf{f}_p and $\boldsymbol{\tau}_p$, at the orientation p can be defined by

$$\mathbf{f}_p = \mathbf{F}_p \bar{\boldsymbol{\rho}}, \quad \boldsymbol{\tau}_p = \mathbf{T}_p \bar{\boldsymbol{\rho}} \quad (3.16a, b)$$

where $\mathbf{F}_p = \mathbf{C}\mathbf{B}_p\mathbf{J}_p$ and $\mathbf{T}_p = \mathbf{C}\mathbf{P}_p\mathbf{B}_p\mathbf{J}_p$; $\mathbf{C} = [\mathbf{I}_3, \dots, \mathbf{I}_3]$ is $3 \times 3N_s$ summation matrix;

$$\mathbf{B}_p = -\text{blkdiag} \left[\text{skew}(\mathbf{B}_{p(1)}), \dots, \text{skew}(\mathbf{B}_{p(k)}), \dots, \text{skew}(\mathbf{B}_{p(N_s)}) \right];$$

$$\mathbf{P}_p = \text{blkdiag} \left[\text{skew}(\mathbf{r}_{p(1)}), \dots, \text{skew}(\mathbf{r}_{p(k)}), \dots, \text{skew}(\mathbf{r}_{p(N_s)}) \right]; \text{ and } \mathbf{J}_p \text{ is in (3.14). Finally,}$$

$$\mathbf{F}_{PM} = [\mathbf{F}_1^T \cdots \mathbf{F}_p^T \cdots \mathbf{F}_p^T]^T \text{ and } \mathbf{T}_{PM} = [\mathbf{T}_1^T \cdots \mathbf{T}_p^T \cdots \mathbf{T}_p^T]^T \text{ in the objective function of (3.10)}$$

and (3.9) can be respectively determined by combining (3.16a) and (3.16b) for all orientations $p = 1, \dots, P$.

3.2.3 Rotor iron equation

During the linear optimization, iron (or magnetic material) can be involved in a rotor design. Assuming that design space is only consisting of PMs, such iron is attached to the rotor PM design space as a predefined non-design space. To account for the force and torque caused by the rotor iron boundary, DMC iron magnetized by each PM design variable is solved, and the sum of the force and torque by the rotor iron is included in the objective functions (3.10) and (3.9).

Consider the rotor iron decomposed by N_M surface elements. Figure 3-5 shows the iron boundary modeled by DMC iron $\hat{\mathbf{j}}_p = [\hat{\mathbf{j}}_{p(1)}^T \cdots \hat{\mathbf{j}}_{p(q)}^T \cdots \hat{\mathbf{j}}_{p(N_M)}^T]^T$ magnetized by a surface current $\mathbf{j}_{p(k)}$ in (3.13). With the flux density $\mathbf{B}_{p(k,q)} = \bar{\mathbf{B}}_{p(k,q)} \mathbf{j}_{p(k)}$ formed by $\mathbf{j}_{p(k)}$ on the location of $\hat{\mathbf{j}}_{p(q)}$, DMC iron $\hat{\mathbf{j}}_p$ with respect to $\mathbf{j}_{p(k)}$ is solved by the DMC model for magnetic materials in (2.38):

$$\hat{\mathbf{j}}_{p(k)} = \mathbf{\Lambda}_{p(k)} \mathbf{j}_{p(k)} \quad (3.17)$$

where $3N_M \times 3N_S$ matrix $\Lambda_{p(k)} = \mathbf{T}^T (\mathbf{D} + \mathbf{S})^{-1} \mathbf{T} \bar{\mathbf{B}}_{p(k)}$; $\mathbf{T} = \text{blkdiag}(\mathbf{T}_{(1)}, \dots, \mathbf{T}_{(q)}, \dots, \mathbf{T}_{(N_M)})$; .

$\mathbf{T}_{(q)} = [\mathbf{t}_{(q)1} \ \mathbf{t}_{(q)2}]^T$ for the orthonormal surface tangent vectors $\mathbf{t}_{(q)1}$ and $\mathbf{t}_{(q)2}$ of the $(q)^{th}$ iron surface; and $\bar{\mathbf{B}}_{p(k)} = [\mathbf{B}_{p(k,1)}^T, \dots, \mathbf{B}_{p(k,N_M)}^T]^T$. Combining (3.17) for $k=1, \dots, N_S$ gives the

linear relation between \mathbf{j}_p and $\hat{\mathbf{j}}_p$ at an orientation p :

$$\hat{\mathbf{j}}_p = \Lambda_p \mathbf{j}_p \quad (3.17)$$

where $\Lambda_p = \sum_{k=1}^{N_S} \Lambda_{p(k)}$, and (3.14) gives a relationship between $\hat{\mathbf{j}}_p$ and $\bar{\mathbf{p}}$:

$$\hat{\mathbf{j}}_p = \hat{\mathbf{J}}_p \bar{\mathbf{p}} \quad (3.18)$$

where $\hat{\mathbf{J}}_p = \Lambda_p \mathbf{J}_p$; and Λ_p is same for all rotor orientations since the rotor iron is fixed to the rotor PM space. Using (3.18), (3.16a) and (3.16b) for the iron boundary leading to:

$$\hat{\mathbf{f}}_p = \hat{\mathbf{F}}_p \bar{\mathbf{p}}, \quad \hat{\boldsymbol{\tau}}_p = \hat{\mathbf{T}}_p \bar{\mathbf{p}} \quad (3.19a, b)$$

where $\hat{\mathbf{F}}_p = \hat{\mathbf{C}} \hat{\mathbf{B}}_p \Lambda_p \hat{\mathbf{J}}_p$ and $\hat{\mathbf{T}}_p = \hat{\mathbf{C}} \hat{\mathbf{P}}_p \hat{\mathbf{B}}_p \Lambda_p \mathbf{J}_p$; $\hat{\mathbf{C}} = [\mathbf{I}_3, \dots, \mathbf{I}_3]$ is $3 \times 3N_M$ summation matrix; $\hat{\mathbf{B}}_p = -\text{blkdiag} \left[\text{skew}(\hat{\mathbf{B}}_{p(1)}), \dots, \text{skew}(\hat{\mathbf{B}}_{p(q)}), \dots, \text{skew}(\hat{\mathbf{B}}_{p(N_M)}) \right]$;

$\hat{\mathbf{P}}_p = \text{blkdiag} \left[\text{skew}(\hat{\mathbf{r}}_{p(1)}), \dots, \text{skew}(\hat{\mathbf{r}}_{p(q)}), \dots, \text{skew}(\hat{\mathbf{r}}_{p(N_M)}) \right]$; $\hat{\mathbf{B}}_{p(q)}$ is the flux density of

the EM with the input $J(\theta_p)$ at the orientation θ_p ; and $\hat{\mathbf{r}}_{p(q)}$ is a position of the $(q)^{th}$ iron

surface element. Finally, redefining $\mathbf{F}_{PM} = [(\mathbf{F}_1 + \hat{\mathbf{F}}_1)^T, \dots, (\mathbf{F}_p^T + \hat{\mathbf{F}}_p^T), \dots, (\mathbf{F}_p^T + \hat{\mathbf{F}}_p^T)]^T$ and

$\mathbf{T}_{PM} = [(\mathbf{T}_1 + \hat{\mathbf{T}}_1)^T, \dots, (\mathbf{T}_p + \hat{\mathbf{T}}_p)^T, \dots, (\mathbf{T}_p + \hat{\mathbf{T}}_p)^T]^T$ can account for rotor PM and iron

force/torques together in the respective objective functions (3.10) and (3.9).

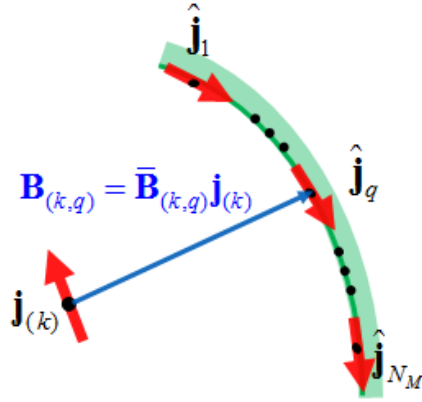


Figure 3-5 Iron boundary magnetized by a PM surface current

3.3 ILLUSTRATIVE EXAMPLES

The Layout Optimization model has been formulated by the DMC modeling method. The optimization is illustrated with a 1-DOF rotary motor and a 2-DOF rotational stage which can be regarded as 2D design problems for a spherical motor capable of spinning and inclinational motion in a single joint. Figure 3-6 shows how the 2D examples are extracted from horizontal and vertical cross sections of an existing spherical motor. With the optimized results, the preferred design layouts will be chosen on the basis of output performance while taking into account the effects of rotor iron and the number of EMs and PMs.

For the 2D design problems, following four design configurations (DCs) for a rotor design space are considered:

DC1: M_r, M_θ , and M_ϕ without a rotor iron

DC2: M_r, M_θ , and M_ϕ with a rotor iron

DC3: Only M_r without a rotor iron

DC4: Only M_r with a rotor iron

where M_r, M_θ , and M_φ denote PM magnetizations in the spherical coordinate system.

DC1 and DC2 newly optimize the rotor design space with PMs magnetized by r, θ , and φ directions, and compares conventional motor designs optimized by only radially magnetized PMs in DC3 and DC4. Also, separately optimize rotor designs with and without iron boundary compare the effects of the rotor iron on improving output performances. With the optimized results, all DCs are compared with its design complexity and performance.

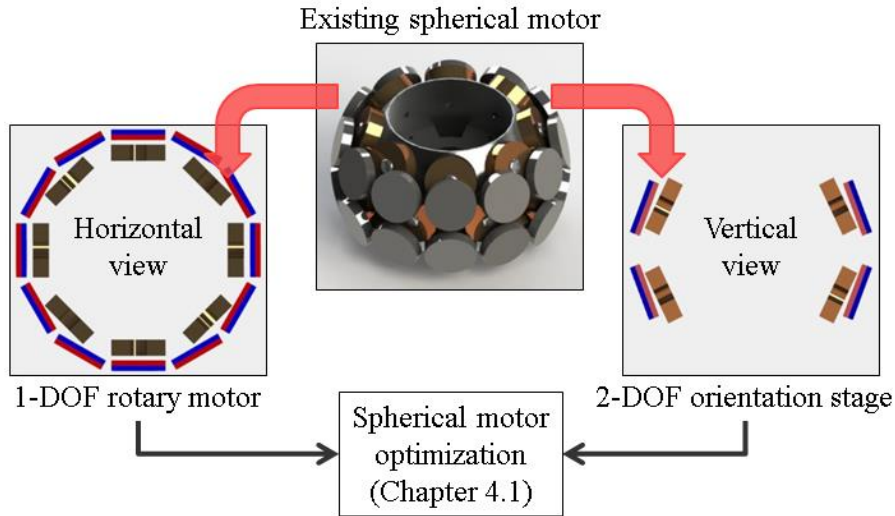


Figure 3-6 Flowchart of 3-DOF spherical motor optimization

3.3.1 Electric input current specification

Electric input currents for the design optimization of 1-DOF rotary motor and 2-DOF orientation stage are specified by either of the number of PM poles n_{pole} or distance between PM poles l_{pole} . The assembly of an EM and external rotor design space of 1-DOF

rotary motor and 2-DOF orientation stage are shown in Figure 3-7 (a) and (b) respectively where θ and φ denote relative orientation between the EM and rotor design space; and the rotor design space of 1-DOF rotary motor is closed ends while the 2-DOF orientation stage has an opened design space sized by φ_{stator} . The specification of the electric input current for each example is described as follows.

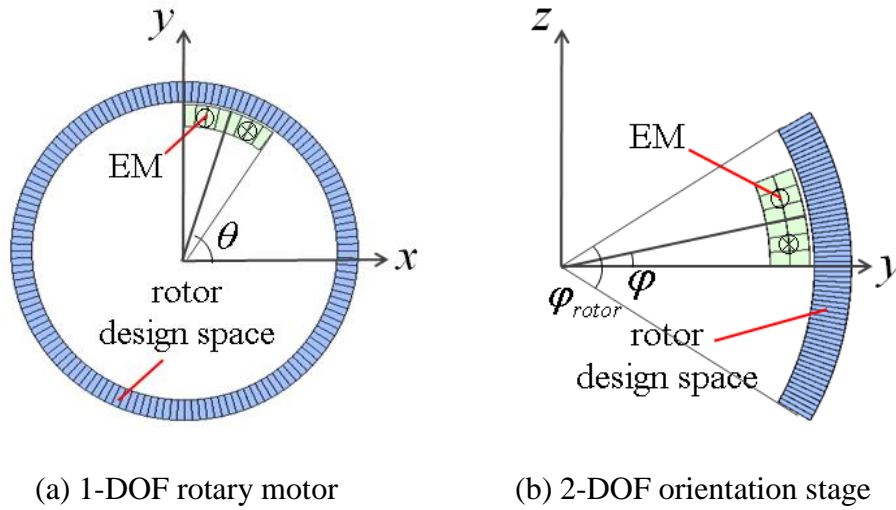


Figure 3-7 EM input current specifications of 2D design examples

1-DOF rotary motor with an external rotor (closed design space)

The 1-DOF rotary motor being optimized has closed rotor as shown in Figure 3-7(a). First, the number of PM poles is set to any positive even $n_{pole} = 2, 4, 6, \dots, n_{PM} / 2$ to make a fair of north and south PM poles. For the relative angular position of an EM θ , the electric input current $J(\theta)$ is defined to have a square-wave form:

$$J(\theta) / J_{\max} = (-1)^{\bar{\theta}}, \quad \bar{\theta} = \left\lfloor \frac{\theta}{2\pi / n_{pole}} \right\rfloor \quad (3.20)$$

where J_{\max} is the maximum current density in the EM; and $\lfloor x \rfloor$ is the floor function to find the maximum integer less than x .

2-DOF orientation stage (opened design space)

Figure 3-7(b) shows the axisymmetric 2-DOF orientation stage having the opened rotor sized by φ_{rotor} . To define PM pole position, the pole distance l_{pole} is used to support various PM shapes near the ends of the rotor. For specifying PM pole positions, two different configurations, denoted by even and odd pole, are considered by:

- Even pole having even number of n_{pole} distributes PM poles with anti-symmetric polarity patterns about y-axis.
- Odd pole with odd number of n_{pole} have symmetric polarity patterns about y-axis; and one of the PM pole should be located on the y-axis.

The square-wave formed input currents, $J_E(\varphi)$ and $J_O(\varphi)$ for even and odd poles are respectively defined by

$$J_E(\varphi) / J_{\max} = (-1)^{\bar{\varphi}_E} \quad \text{where } \bar{\varphi}_E = \left\lfloor \frac{\varphi_b + l_{pole} / 2}{l_{pole}} \right\rfloor \quad (3.21)$$

$$J_O(\varphi) / J_{\max} = (-1)^{\bar{\varphi}_O} \text{sign}(\varphi) \quad \text{where } \bar{\varphi}_O = \left\lfloor \frac{\varphi_b}{l_{pole}} \right\rfloor \quad (3.22)$$

where $\varphi_b = \min(|\varphi|, \varphi_{rotor} / 2)$ prevents the polarity changing outside of the rotor space.

With $n_{PM(O)}$ and $n_{PM(E)}$ respective cases of the odd and even pole patterns,

$n_{PM} = n_{PM(O)} + n_{PM(E)}$ cases of PM pole patterns are used in the optimization.

3.3.2 1-DOF rotary motor

1-DOF rotary motor shown in Figure 3-8(a) will be optimized by Layout Optimization. Figure 3-8(b) shows the rotor PM design space with the inner radius r_o and outer radius r_1 , and the rotor iron with the inner radius r_1 and outer radius r_2 to check the effects of iron boundary on the optimization results. The predefined stator with the inner radius a_i and outer radius a_o shown in Figure 3-8(c) has N_{EM} of stator EM coils fully occupying the stator space; and the angular size of an EM θ_{EM} is defined by

$$\theta_{EM} = 2\pi / N_{EM} \quad (3.23)$$

where the core of an EM core is located on the center angle of the EM, but its actual volume is zero; electric current flowing along +z or -z direction alters its direction across the core. The z axial thickness of the rotor and stator space is l_z . Rotor iron and design space are decomposed by $N_V = 180$ volume, $N_S = 900$ and $N_M = 2160$ surface elements, and $\mu_0 M_{\max} = 1T$.

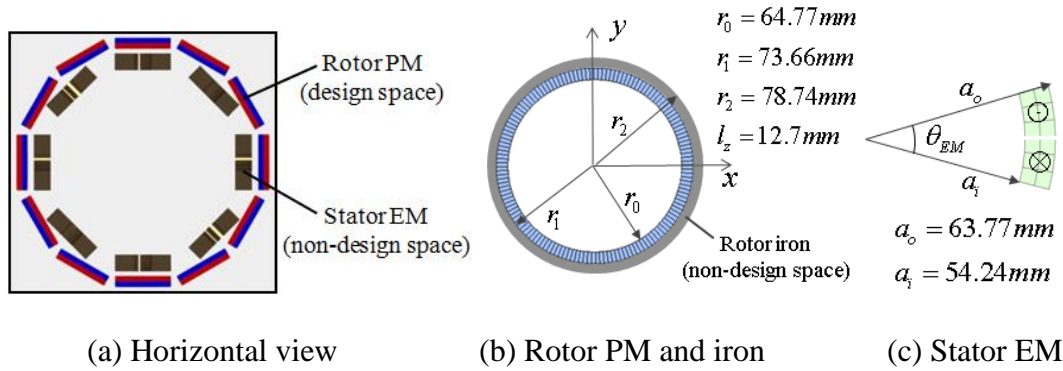


Figure 3-8 Optimization parameters for the 1-DOF rotary motor

Once rotors are designed by linear topology optimization for every combinations of n_{pole} and N_{EM} , integer programming will be applied to maximize achievable minimum

spinning torque T_{z_0} with the maximum electric current input J_{\max} . On the integer programming, 1-phase and 2-phase EM inputs are separately applied for computing output torque.

- 1-phase input denotes each EM has independent input channel; $N_{EM} / N_{inp} = 1$ where N_{inp} denotes the number of the input channels.
- 2-phase inputs shares input channels of opposing two EMs, and reduces N_{inp} by half ($N_{EM} / N_{inp} = 2$). 2-phase inputs has two wiring choices of connecting EMs; and 2-phase (+) and (-) respectively shown in Figure 3-12(a) and (b). 2-phase (+) is effective to odd n_{pole} rotor designs, and 2-phase (-) is for even n_{pole} . If (+) and (-) are inversely applied to even and odd poles, a pair of EMs cancels output torque at all orientations.

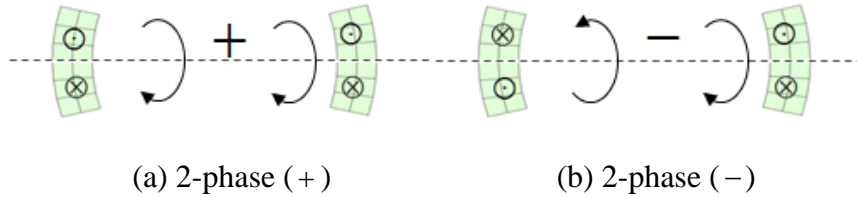


Figure 3-9 Two cases of 2-phase inputs for the 1-DOF rotary motor

Linear topology optimization

$N_{EM} = 3, 4, \dots, 16$ and its respective $n_{pole} = 2, 3, \dots < 3N_{EM}$ are considered to avoid too complex motor designs, and later optimized results will show that performance is not that improved by large N_{EM} or n_{pole} . Along with the EM input current (3.20) and $J_{\max} = 10^7 (A/m^2)$, torques are evaluated at every 0.5° of EM angles leading to the

number of evaluating orientation $P = 720$. As continuous spinning motor about z-axis is optimized, weight factors are set to $w_x = 0, w_y = 0, w_z = 1$, and $w_p = 1$ for $p = 1, \dots, P$.

Integer programming

The minimum spinning torque T_{z0} is evaluated for the combinations of n_{pole} and N_{EM} for each DC, and results are shown in Figure 3-10 where asterisk (*) and square (\square) represent T_{z0} of the optimized design with 1-phase and 2-phase inputs respectively. Following the results, T_{z0} of 2-phase inputs is similar to 1-phase input in even N_{EM} cases, and relatively better than to odd N_{EM} cases. Also, the results show that increasing N_{EM} does not necessarily improve outputs. In the view of DCs, iron boundary mostly improves the output, but improving rate much differs from different N_{EM} . Moreover, DC1 and DC2 being optimized by Halbach PM array give much better outputs than DC3 and DC4. Considering design complexity and requiring N_{inp} , the $N_{EM} = 10$ and 8 designs (marked by an orange box) makes the best and second best performance for both of DC1 and DC2; the designs with 8 EMs and 10 EMs are chosen as optimized ones.

For 10 and 8 EM designs, T_{z0} as a function of n_{pole} is plotted in Figure 3-13(a) and (b) respectively; and it clearly shows that iron boundary makes large improvement on output torque, but sometimes its effects are tiny or negative. When n_{pole} becomes the multiple of N_{EM} , T_{z0} should be dropped to zero, but finitely decomposed design space leads to non-zero values. $(N_{EM}, n_{pole}) = (10, 18)$ for DC1 and $(N_{EM}, n_{pole}) = (10, 14)$ for

DC2 can be optimal designs for 1-DOF rotary motor. For spherical motor optimization in Chapter 4, we consider more design results (marked by orange box in Figure 3-11):

$(N_{EM}, n_{pole}) = (10,12), (10,14), (10,16), (10,18), (8,10), (8,12),$ and $(8,14)$.

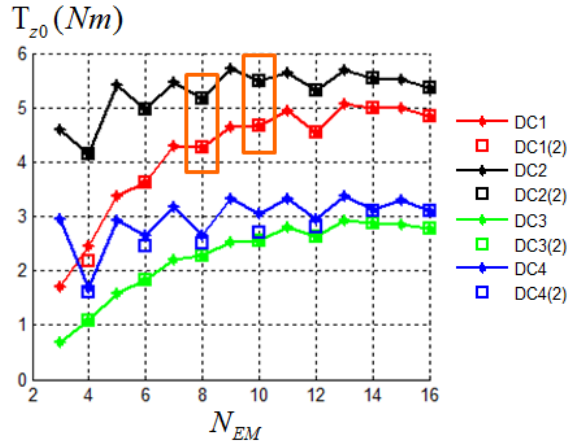


Figure 3-10 T_{z0} of linearly optimized designs for the 1-DOF rotary motor

Optimized rotor designs are depicted in Figure 3-12 where red arrows in enlarged view represent magnetizing direction of PMs leading to following conclusions: (1) DC1 and 2 are optimized to Halbach array while DC3 and 4 become conventional PM array, (2) mostly tangentially magnetized PMs are longer than radially magnetized ones, and their ratios are different from each design, (3) optimized designs of DC1 for each (N_{EM}, n_p) are same or almost similar as DC2 results.

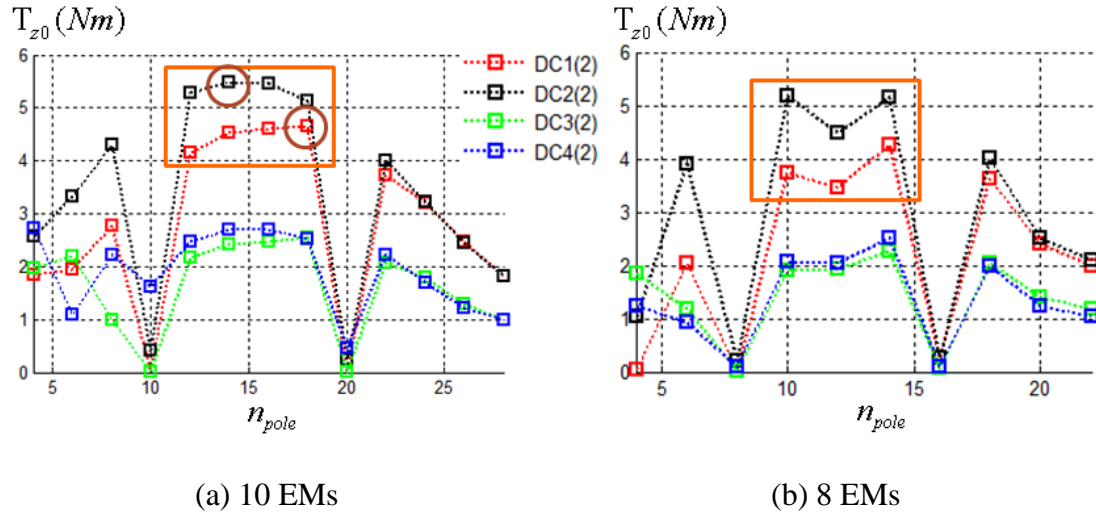


Figure 3-11 Integer programming for 8 and 10 EMs

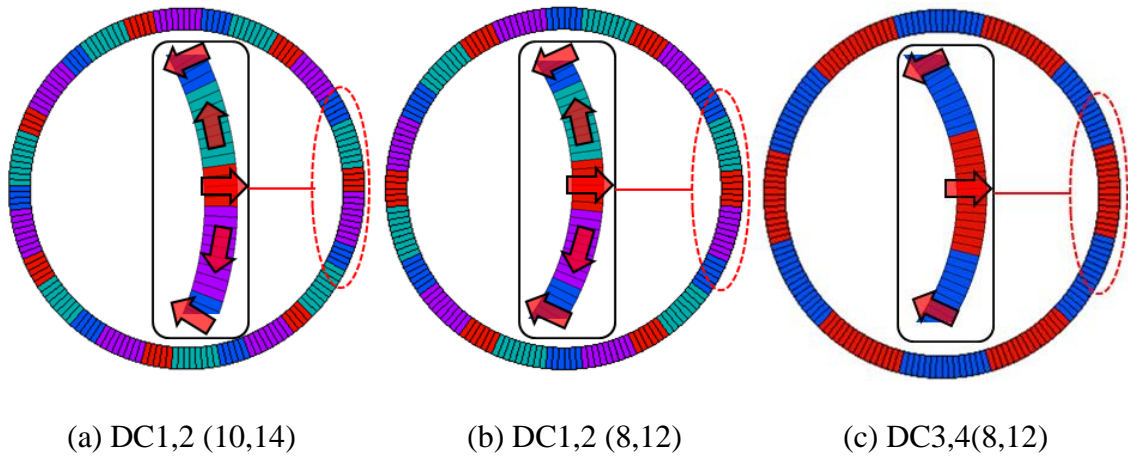


Figure 3-12 Optimized rotor PM designs for the 1-DOF rotary motor

3.3.3 2-DOF orientation stage

Axis-symmetric 2-DOF orientation stage being optimized by Layout Optimization is shown in Figure 3-13(a). The rotor PM design space with the inner radius r_o and outer radius r_i is shown in Figure 3-13(b) where the rotor iron has the inner radius r_1 and outer radius r_2 ; and the angular size of the rotor space; stator EM coils fully occupying the stator space is shown in Figure 3-13(c). The rotor and stator space are respectively sized

by angles φ_{rotor} and φ_{stator} in the inclinational direction, and thickness l_z along x axis. The stator EM coils fully occupying the stator space is defined by N_{EM} :

$$\varphi_{EM} = \varphi_{stator} / N_{EM} \quad (3.24)$$

where EM input current flowing along +x or -x direction changes its direction across the core located on the center of the EM. For odd and even N_{EM} , the locations of EM cores are respectively defined in (3.25) and (3.26).

$$\varphi_{loc} = 0, \pm \varphi_{EM}, \dots, \pm \left(\frac{N_{EM} - 1}{2} \right) \varphi_{EM} \text{ for odd } N_{EM} \quad (3.25)$$

$$\varphi_{loc} = \pm \frac{1}{2} \varphi_{EM}, \dots, \pm \left(\frac{N_{EM} - 1}{2} \right) \varphi_{EM} \text{ for even } N_{EM} \quad (3.26)$$

The optimization uses rotor iron and design decomposed by $N_v = 60$ volume, $N_s = 301$ and $N_M = 736$ surface elements; $\mu_0 M_{max} = 1T$ and $J_{max} = 10^7 (A/m^2)$.

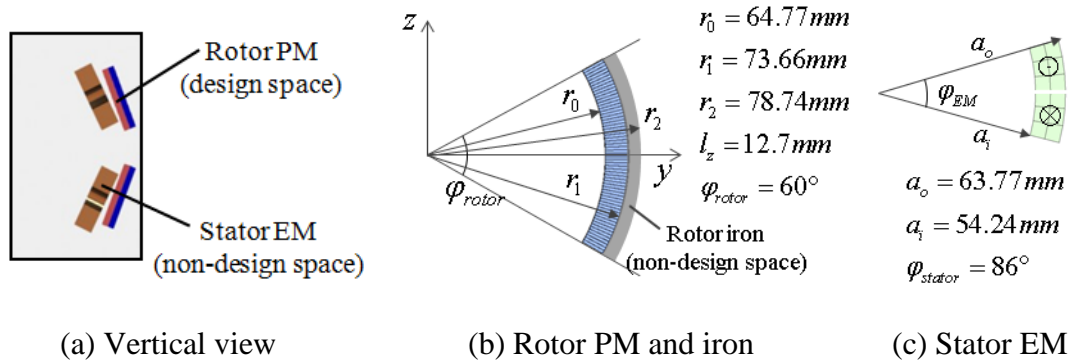


Figure 3-13 Optimization parameters for the 2-DOF orientation stage

Linear topology optimization

The optimization of the 2-DOF inclinational stage considers EMs with $N_{EM} = 1, 2, 3, 4, 5$, and its respective PM pole length $l_{pole} = \varphi_{d0} + \varphi_d \times [1, 2, \dots]$ where $\varphi_{d0} = 5^\circ$ denotes the minimum angular position of the PM pole to prevent having too many n_{pole} ; and $\varphi_d = 0.5^\circ$ is the incremental angle of l_{pole} .

While rotor PM is linearly optimized to maximize torque average by an EM, the range of the orientation angle φ_p of the EM is extended by the maximum angular position of the EMs, $\max(\varphi_{loc})$:

$$-\varphi_{\max} - \max(\varphi_{loc}) \leq \varphi_p \leq \varphi_{\max} + \max(\varphi_{loc}) \quad (3.27)$$

where $\varphi_{\max} = 22.5^\circ$ is the maximum inclinational motion of the rotor. The contribution of each EM for the extended angular motion in (3.27) differs from its core position; it is explained by different weight factors w_p in (3.9):

$$w_p(\varphi_p) = \sum_{i=1}^{N_{EM}} \left[u(\varphi_p - (\varphi_i - \varphi_{\max})) - u(\varphi_p - (\varphi_i + \varphi_{\max})) \right] \quad (3.28)$$

where u denotes a unit step function; φ_i is i^{th} EM position in (3-25) or (3-26). With these optimization parameters, normalized weight factors $w_p / \|\mathbf{w}_p\|_1$ for different number of EMs are plotted in Figure 3-14; it shows that weight factor is symmetric about y-axis due to symmetric EM positions, and torques on small angles are more stressed than torques at large angles. The linear optimization evaluates torques at $P = 181$ different orientations; and the weight factors for moving directions are $w_x = 1, w_y = 0$, and $w_z = 0$ to only optimize the inclinational motion.

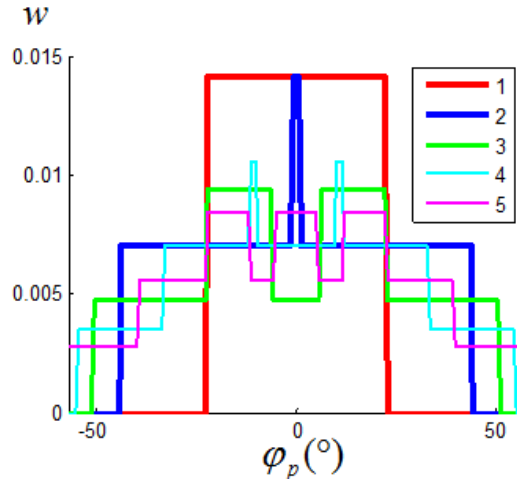


Figure 3-14 Weight factors for the linear optimization

Integer programming

The integer programming evaluates inclinational torques of linearly optimized designs to maximize minimum torque T_{x0} using 1-phase input ($N_{EM}/N_{inp}=1$). From the evaluated T_{x0} for each DCs as shown in Figure 3-15, $N_{EM} = 3$ and 2 designs (marked by orange box) are chosen to the best and second best designs in the view of T_{x0} over N_{inp} .

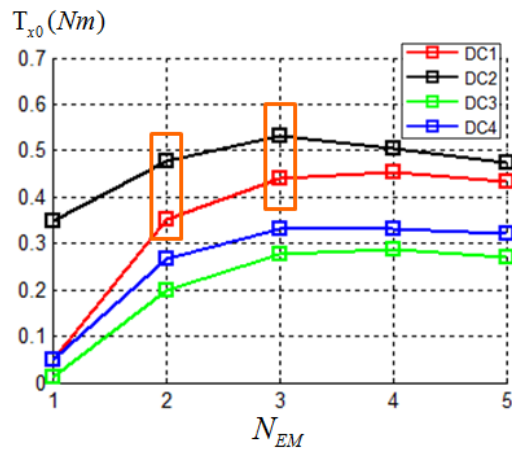


Figure 3-15 T_{x0} of optimized designs for the 2-DOF orientation stage

Detailed T_{x0} of those designs as a function of l_{pole} is shown in Figure 3-16 where the current inputs for odd (O) and even (E) poles are respectively denoted by asterisk (*) and square (\square). The result shows 3EM design with the odd input gives the best torque output, but its design is relatively complex (3 PM poles with 5~7 PMs). In both case, the even input gives reasonable torque output with simpler rotor designs (2 PM poles with 3~5 PMs). Optimized rotor designs for DC2 and DC4 are shown in Figure 3-17 where red arrow denotes magnetizing directions of PMs. Similar to the result from 1-DOF rotary motor, the rotor designs are optimized to Halbach array, and tangentially magnetized connecting PMs are longer than radial ones. Also, optimized designs for each (N_{EM}, l_{pole}) become almost same for DC1 and DC2, but has small difference around the ends of the rotor are observed due to the rotor iron. In the spherical motor optimization in Chapter 4, stator EM layout with $N_{EM} = 2$ and 3 will be included, but the rotor designs will not use the optimized l_{pole} , but it will be newly optimized in 3D design space.

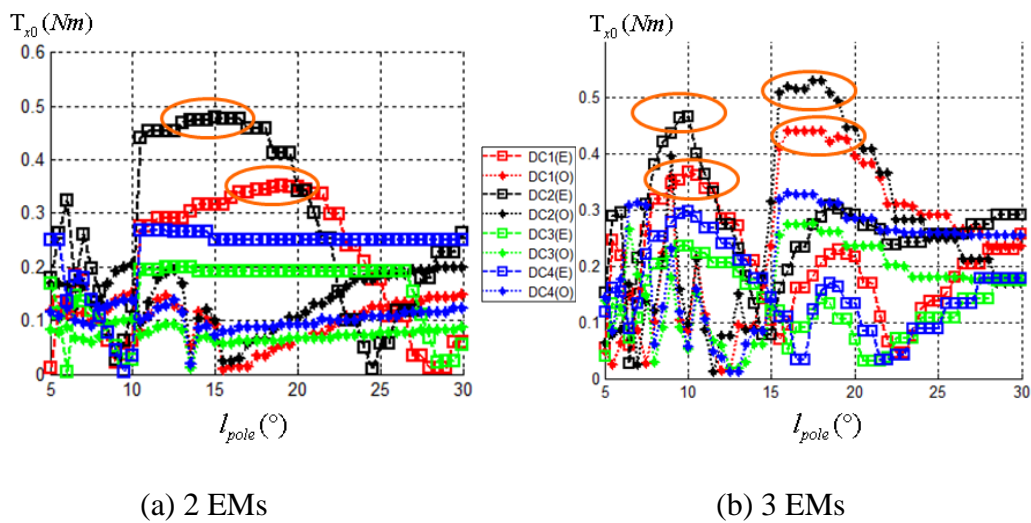


Figure 3-16 Integer programming for the design with 2 and 3 EMs

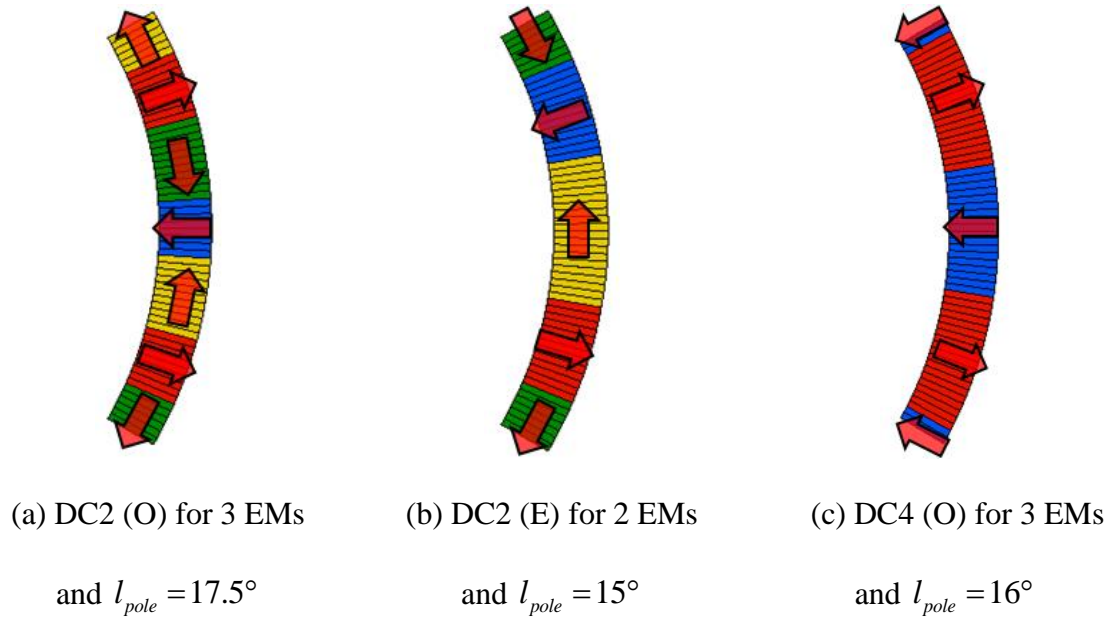


Figure 3-17 Optimized rotor designs for the 2-DOF orientation stage

3.4 SUMMARY

The DMC optimization model based on linear force and torque equations is presented to determine simple and effective initial designs of electromagnetic actuators. To overcome nonlinearity and local convergence of electromagnetic system, we described the layout optimization through two sequential optimization steps: linear optimization and integer programming. To formulate linear topology optimization problem, the design problems are divided into a number cases of EM and PM pole combinations, and desired EM current inputs are defined with respect to PM pole positions. With linearly optimized designs with or without iron boundary, performances over design complexity are evaluated during integer programming, and desired actuator layout including the number and positions of EM and PM is determined.

Two illustrative examples are presented to optimize horizontal and vertical layout of spherical motor which can be regarded as 1-DOF rotary motor and 2-DOF orientation stage. Following the layout optimization steps, several optimized designs are determined, and these results will be applied on optimizing 3-DOF spherical motor design in Chapter 4.2. Also, as illustrative applications, the optimization of 2-DOF linear-rotary actuator and 1-DOF disk-shaped motor will be followed in Chapter 4.3 and 4.4.

CHAPTER 4

ILLUSTRATIVE DESIGN OPTIMIZATION APPLICATIONS

This chapter illustrates three applications of design optimization based on DMC models as shown in Figure 4-1. The first application demonstrates the DMC-based Layout Optimization method to minimize the rotor weight of an existing ball-joint-like spherical motor. The optimization focuses on its output torque while taking into account its manufacturing cost in terms of the number of input channels and PMs. With optimized designs, the torque characteristics and rotor weight reduction are discussed for a given external loading condition.

The second application is to determine the best combination of EM and PM layouts of a 2-DOF tubular-shaped linear-rotary (LR) motor using the Layout Optimization method. Two of 2D designs, 1-DOF rotary motor with an internal rotor and 1-DOF linear motor, are optimized to determine the best EM and PM layout for 3D designs. With optimized 3D designs, the torque outputs subject to varying external force conditions are discussed.

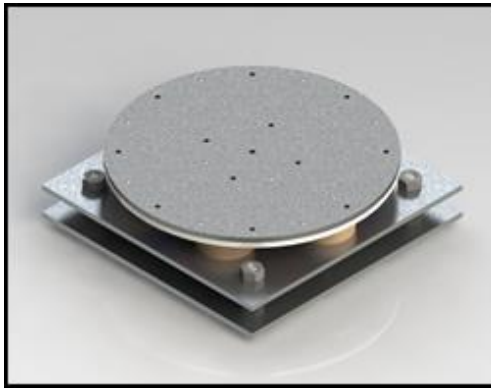
The third application is the optimization of a Disk-shaped synchronous motor (DSSM) which has been fabricated to serve as a basis for experimental validation of the Layout Optimization method. In this study, the DSSM is operated with a 3-phase current input considering the compactness of its design; with this in mind, the torque output of the DSSM is maximized. The experimental validation of the Layout Optimization based on the optimized DSSM motor will be discussed in Chapter 5.



(a) Spherical motor



(b) Linear-rotary motor



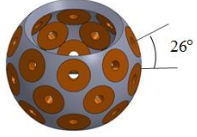
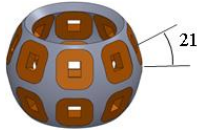
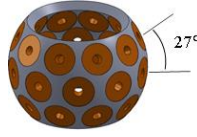
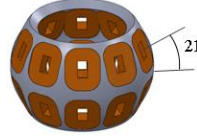
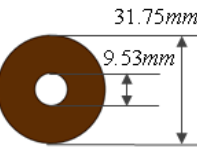
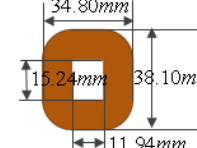
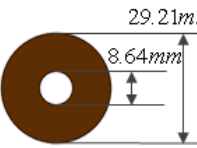
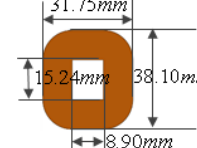
(c) Disk-shaped synchronous motor

Figure 4-1 Illustrative applications for the design optimization

4.1 SPHERICAL MOTOR

The existing spherical motor shown in Figure 4-1(a) is optimized by the DMC-based Layout Optimization. From the optimized results for 1-DOF rotary motor (spinning motion) and 2-DOF orientation stage (inclinal motion), selected EM and PM layouts for 3D design optimization are shown in Table 4-1 where the predefined stator layouts are denoted by the number of EM-layers N_{SL} and N_{SP} EMs per layer; and the PM layouts to be optimized are denoted by the number of PM-layers N_{RL} and N_{RP} PMs per layer.

Table 4-1 Stator and rotor design space for spherical motor (Coil thickness =9.525mm)

Design	A				B			C				D			
	$N_{SP} = 8, N_{SL} = 3$				$N_{SP} = 8, N_{SL} = 2$			$N_{SP} = 10, N_{SL} = 3$				$N_{SP} = 10, N_{SL} = 2$			
Stator															
															
Rotor (N_{RP})	A0	A1	A2	A3	B1	B2	B3	C1	C2	C3	C4	D1	D2	D3	D4
	12	10	12	14	10	12	14	12	14	16	18	12	14	16	18

Design A represents the existing stator; and Designs B, C, and D are the newly designed stators from the 2D results. The optimization considers two different numbers of PM layers; $N_{RL}=2$ and 3. The number of optimization variables can be reduced using $1/N_{RP}$ sized design space considering the alternating property of the rotor PM magnetization along the spinning direction:

$$\mathbf{M}(\theta_R + 2\pi / N_{RP}) = -\mathbf{M}(\theta_R) \quad (4.1)$$

where θ_R is the spin angle. Combining with the stator layout and rotor N_{RP} , 15 different cases for the integer-linear programming are considered:

- 4 cases for each of Design A, C, and D
- 3 cases for Design B

To compare the torque output with subsequent newly optimized designs, the rotor design space in Design A0 has been optimized by radially magnetized PMs for the existing stator.

4.1.1 Optimization parameters and formulations

For the linear topology optimization, the EM input current with respect to the spinning and inclination motions of the EM or rotor design space is predefined. After describing the optimization parameters including weight factors, the torque output of the spherical motor is evaluated in the integer programming step.

EM input current specification

The spinning and inclinational motions of the rotor can be described in terms of Euler angles. Instead of the 3-DOF rotational motions, the linear optimization only uses simplified 2-DOF motions; the inclination of an EM constrained to yz plane, and the spinning of the rotor about the z axis. Figure 4-2(a) shows an EM and design space initially aligned to the y axis which allows to rotate about the x and z axes by the angles, ϕ_s and θ_r , respectively. Using these angle definitions, the EM input current for the spinning torque T_z and inclinational torque T_x is separately defined for linear optimization. For the $1/N_{RP}$ rotor design space, two different PM layers ($N_{RL}=2$ and 3) are compared in Figure 4-2(b) and (c) respectively where the PM poles are positioned on the side of the design space at $\theta_r = \pm\pi / N_{RL}$; and $N_{RL}=2$ and 3 are denoted by even (E) and odd (O) PM poles.

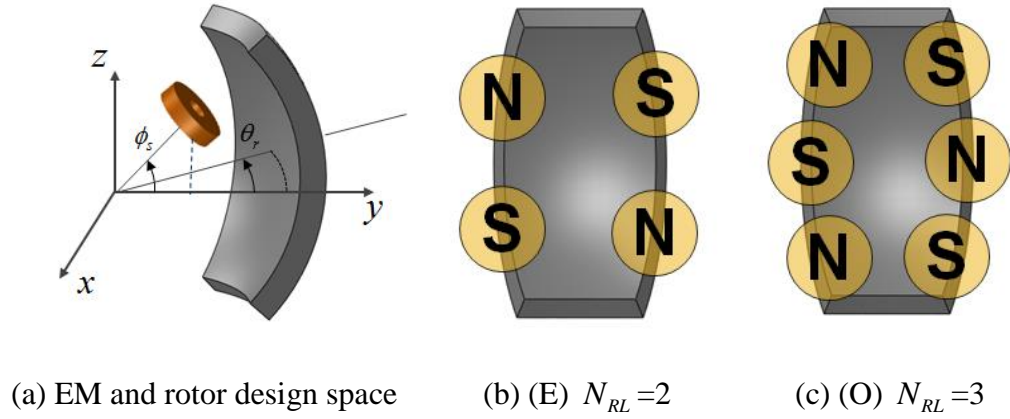


Figure 4-2 Angle definition of EM and design space with two different PM layers

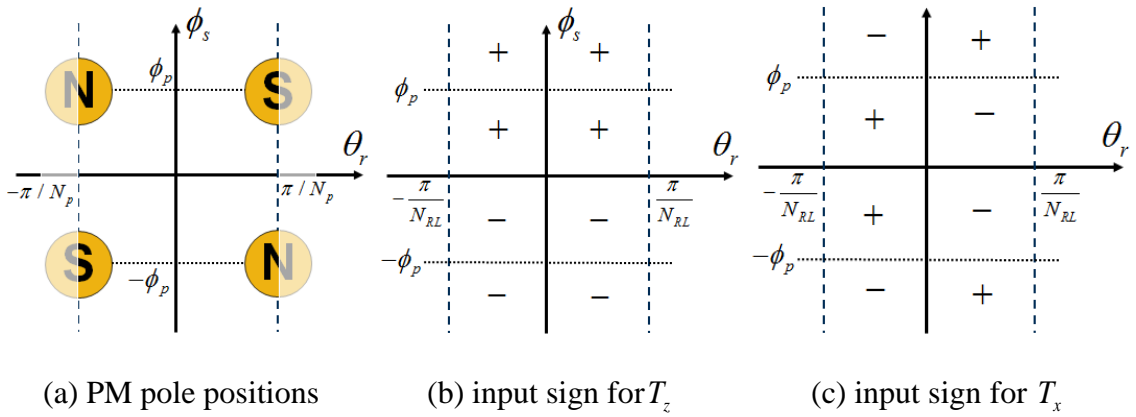


Figure 4-3 EM current input for even poles ($N_{RL}=2$)

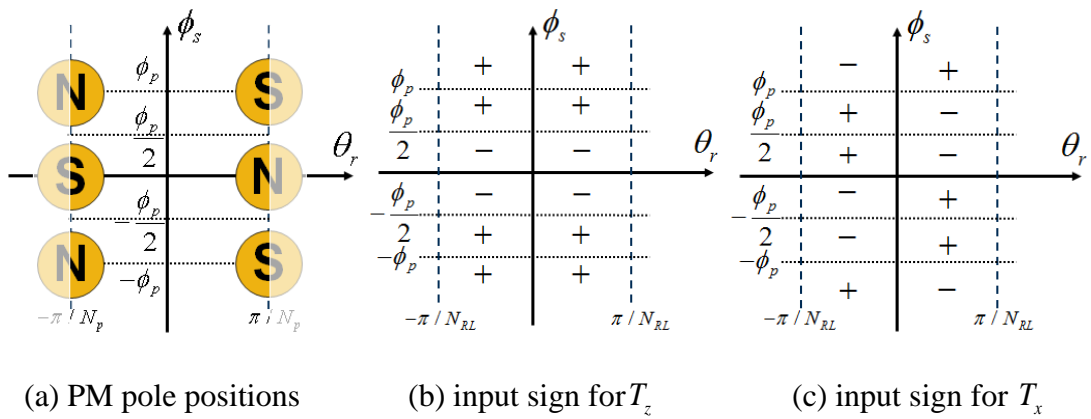


Figure 4-4 EM current input for odd poles ($N_{RL}=3$)

For each N_{RL} , the layout of the (E) and (O) PM poles are depicted on Figure 4-3(a) and Figure 4-4(a) respectively in $\theta_r - \phi_s$ plane. From the given PM pole layout, the sign of the spinning torque T_z and inclinational torque T_x are defined as follows:

- The sign for T_z is independent of θ_r , which changes at $\phi_s = 0$ for Case (E), and at $\phi_s = \pm\phi_p / 2$ for Case (O) as shown in Figure 4-3(b) and 4-4(b).
- The sign for T_x reverses at $\theta_r = 0$, and also changes at the PM layer pole positions; for (E) $\phi_s = \pm\phi_p$, and for (O) $\phi_s = 0$, and $\pm\phi_p$.
- The EM input current can be predefined by $J_z = J_{\max} \text{sign}(T_z)$ for spinning and $J_x = J_{\max} \text{sign}(T_x)$ for inclinational motion.

Optimization parameters

The rotor design spaces with respective optimization parameters are listed in Table 4-2. Each design space is decomposed by N_V volume elements and N_S surface elements, where the DMC for the rotor PMs are placed. For The linear optimization evaluates torques at P different orientations (for P_θ spinning and P_ϕ inclinational orientations), and maximizes the average torques to determine rotor PM design for each of EM and PM pole layouts. With the condition in (4.1) that the PM magnetization alternately changes along the spinning direction, the design variable $\bar{\rho}$ for the full rotor design space is replaced by the rotor PM design variable $\bar{\rho}_{sym}$ for the $1/N_{RP}$ design space:

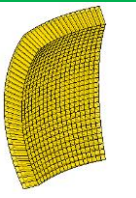
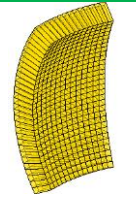
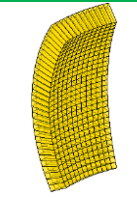
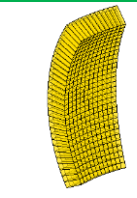
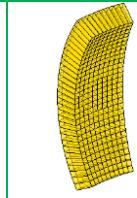
$$\bar{\rho} = \mathbf{S}\bar{\rho}_{sym} \quad (4.2)$$

where the $(V_N \times N_{RP} V_N)$ matrix $\mathbf{S} = [\mathbf{I}_{V_N}, -\mathbf{I}_{V_N}, \dots, \mathbf{I}_{V_N}, -\mathbf{I}_{V_N}]^T$ replicates the PM magnetization of each volume, and also other DMC parameters such as surface geometry and source positions can be simply obtained by z-axis transformation.

The linear optimization only maximizes T_x and T_z leading to $w_x = 1, w_y = 0, w_z = 1$.

The weight factors for the relative rotor orientations are similarly defined by the 2D optimization cases using the predefined stator EM layouts.

Table 4-2 Optimization parameters for rotor design spaces

N_{RP}	10	12	14	16	18
design space					
N_V, N_S	540, 2208	420, 1724	360, 1482	360, 1482	300, 1240
P_θ, P_ϕ	80, 100	62, 100	52, 100	46, 100	40, 100
$P = P_\theta \times P_\phi$	8000	6200	5200	4600	4000

Torque evaluation for the integer programming

Once the rotor PMs are linearly optimized, the torque output actuated by all the stator EMs are evaluated by using the DMC model. The torque τ_s by a pair of EMs with input J_s can be linearly represented by

$$\mathbf{k}_s J_s = \tau_s \quad (4.3)$$

where \mathbf{k}_s is the current-torque relation of the s^{th} pair of EMs at a rotor orientation.

Combining (4.3) over N_{inp} results in the net torque $\mathbf{T} = [T_x, T_y, T_z]^T$ which can be

expressed as a matrix product of the EM inputs $\mathbf{u} = [J_1, \dots, J_s, \dots, J_{N_{imp}}]^T$ and the current-torque matrix $\mathbf{K} = [\mathbf{k}_1, \dots, \mathbf{k}_s, \dots, \mathbf{k}_{N_{imp}}]$:

$$\mathbf{K}\mathbf{u} = \mathbf{T} \quad (4.4)$$

At a certain orientation, the redundant current inputs can be determined by solving a simple linear optimization problem that maximizes the torques with a weight factor $\mathbf{c} = [c_x, c_y, c_z]^T$:

$$\underset{\mathbf{u}, \tau_m}{\text{maximize}} \quad \mathbf{c}^T \mathbf{T} \quad \text{subjected to} \quad \mathbf{K}\mathbf{u} = \mathbf{T}, \quad -J_{\max} \leq J_s \leq J_{\max} \quad (4.5)$$

where the \mathbf{T} components can be either a specified constant or a variable to be maximized; and J_{\max} is the maximum input current. Using (4-5), the integer programming evaluates the maximum inclinational torque T_x with $\mathbf{c} = [1, 0, 0]^T$ and $\mathbf{T} = [T_x, 0, 0]^T$, and the maximum spinning torque T_z with $\mathbf{c} = [0, 0, 1]^T$ and $\mathbf{T} = [0, 0, T_z]^T$ with other torques constrained to zero. Then the performance of each linearly optimized design is measured by

$$T_0 = \min(T_{x0}, T_{z0}) \quad (4.6)$$

where $T_{x0} = \min(T_x)$ and $T_{z0} = \min(T_z)$ for the range of the rotor spin angle θ and that of the inclinational angle ϕ . For the preferred designs, the inclinational and spinning torque characteristics will be discussed with the following measurements:

$$\tau_{x0}(\phi) = \min[T_x(\phi)], \quad \tau_{z0}(\phi) = \min[T_z(\phi)] \quad (4.7 \text{ a,b})$$

where $\tau_{x0}(\phi)$ and $\tau_{z0}(\phi)$ denote the minimum torque at a certain inclinational angle ϕ .

For all torque computation, $J_{\max} = 2.8343 \times 10^7 (A/m^2)$ (equivalent to 3A EM input

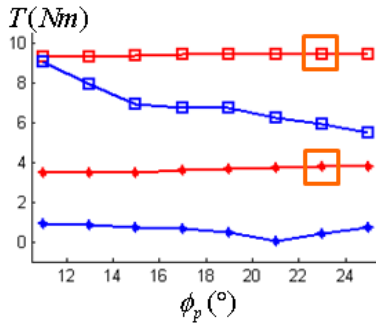
current for existing spherical motor); and the rotor design space is optimized by PM with residual flux density $\mu_0 M_{\max} = 1.0(T)$.

4.1.2 Layout Optimization results

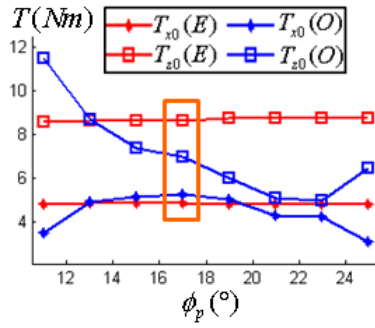
For each of the design layouts in Table 4-1, the rotor PM design is optimized for different PM pole position, ϕ_s . The evaluated T_{x0} and T_{z0} are shown in Figure 4-5 where even (E) and odd (O) PM pole configurations are plotted with red and blue lines respectively. For all cases, odd PM designs are resulted in drastic changes for ϕ_s while even PM designs show small variations. Following T_0 in (4.6), the best design is chosen for each of design cases as marked (orange-square) in Figure 4-5. As a special case, the best designs for each of even and odd PMs are included for further investigation of newly optimized rotor designs with the existing stator.

Figure 4-6 shows the $1/N_{RP}$ rotors of the chosen designs along with (even or odd) PM pole type and its layer position ϕ_s . The rotor designs depict the magnetizing directions of PM volumes in spherical coordinate system (r, θ, ϕ) ; $+M_r$ (red), $-M_r$ (blue), $+M_\theta$ (teal), $-M_\theta$ (violet), $+M_\phi$ (yellow), and $-M_\phi$ (green). Except for design A0 (intentionally optimized only with the radial PMs), all optimized designs are resulted into Halbach PM array: radially magnetized PMs are surrounded by connecting PMs magnetized along θ and ϕ directions. As the rotor designs are seen from the outside of the rotor, the flux densities of the rotor PMs are weakened by the opposing PM polarities of all connecting PMs with respect to nearby radially magnetized PM while intensifying the airgap flux densities at the other side. The number of the PM layer is resulted into 3

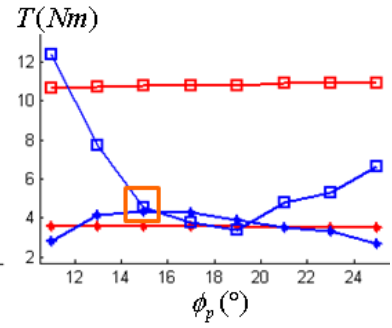
for even and 5 for odd PM configurations. The large torque variations for the odd pole designs were found to be mainly caused by the small design space for locating 5 layers of PMs.



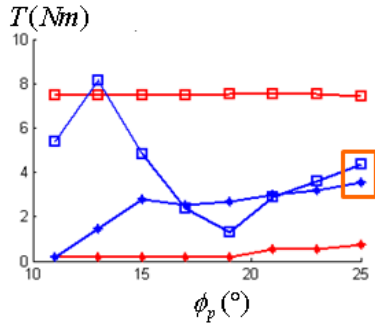
(a) Design A1



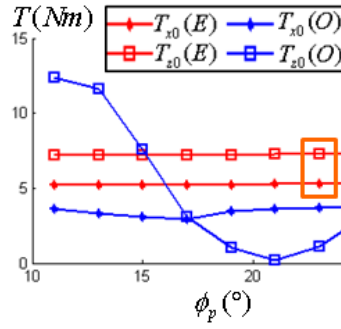
(b) Design A2



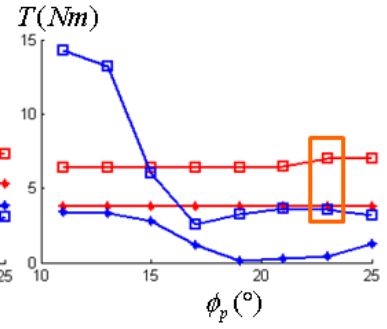
(c) Design A3



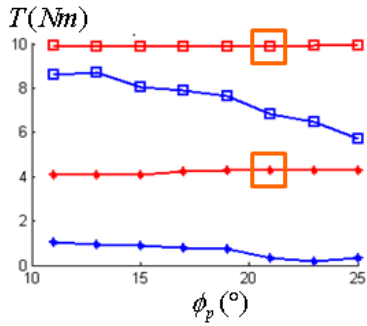
(d) Design B1



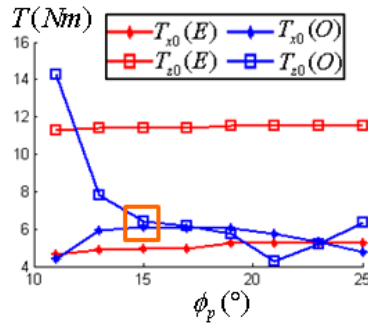
(e) Design B2



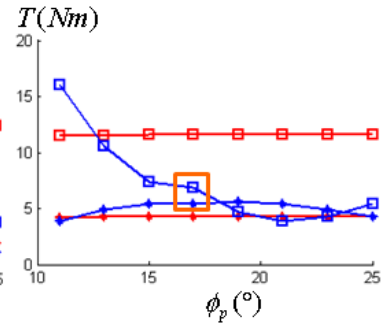
(f) Design B3



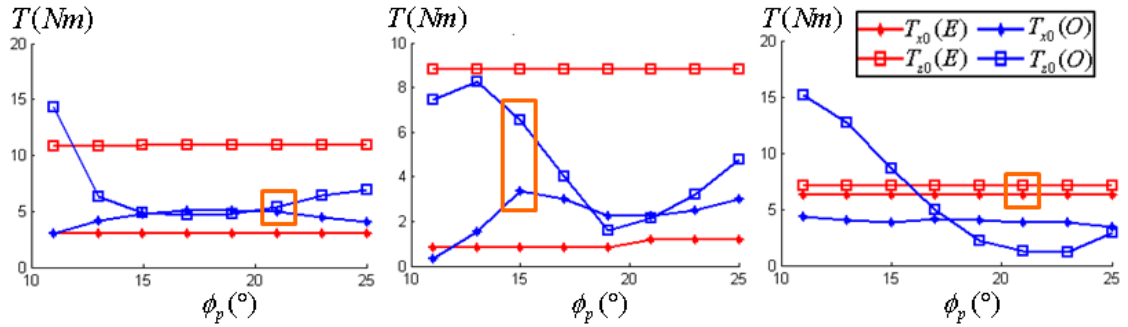
(g) Design C1



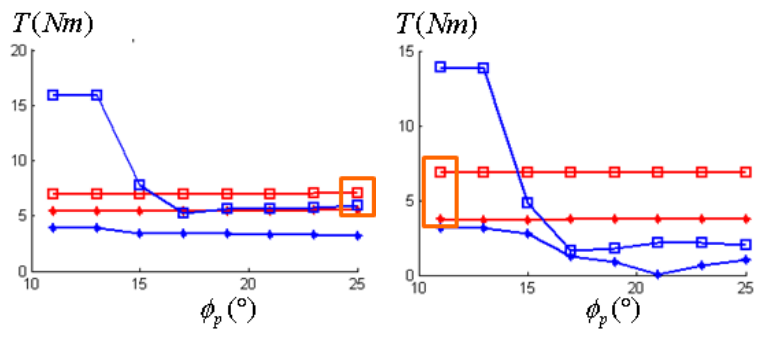
(h) Design C2



(i) Design C3

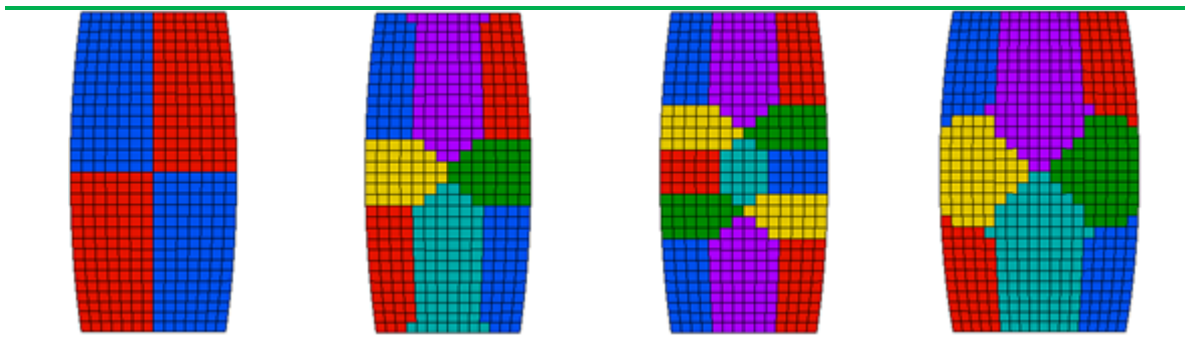


(j) Design C4 (k) Design D1 (l) Design D2



(m) Design D3 (n) Design D4

Figure 4-5 τ_{x_0} and τ_{z_0} of linearly optimization designs for different ϕ_p



(a) A0(E) $\phi_p = 15^\circ$ (b) A2(E) $\phi_p = 17^\circ$ (c) A2(O) $\phi_p = 17^\circ$ (d) A1(E) $\phi_p = 23^\circ$

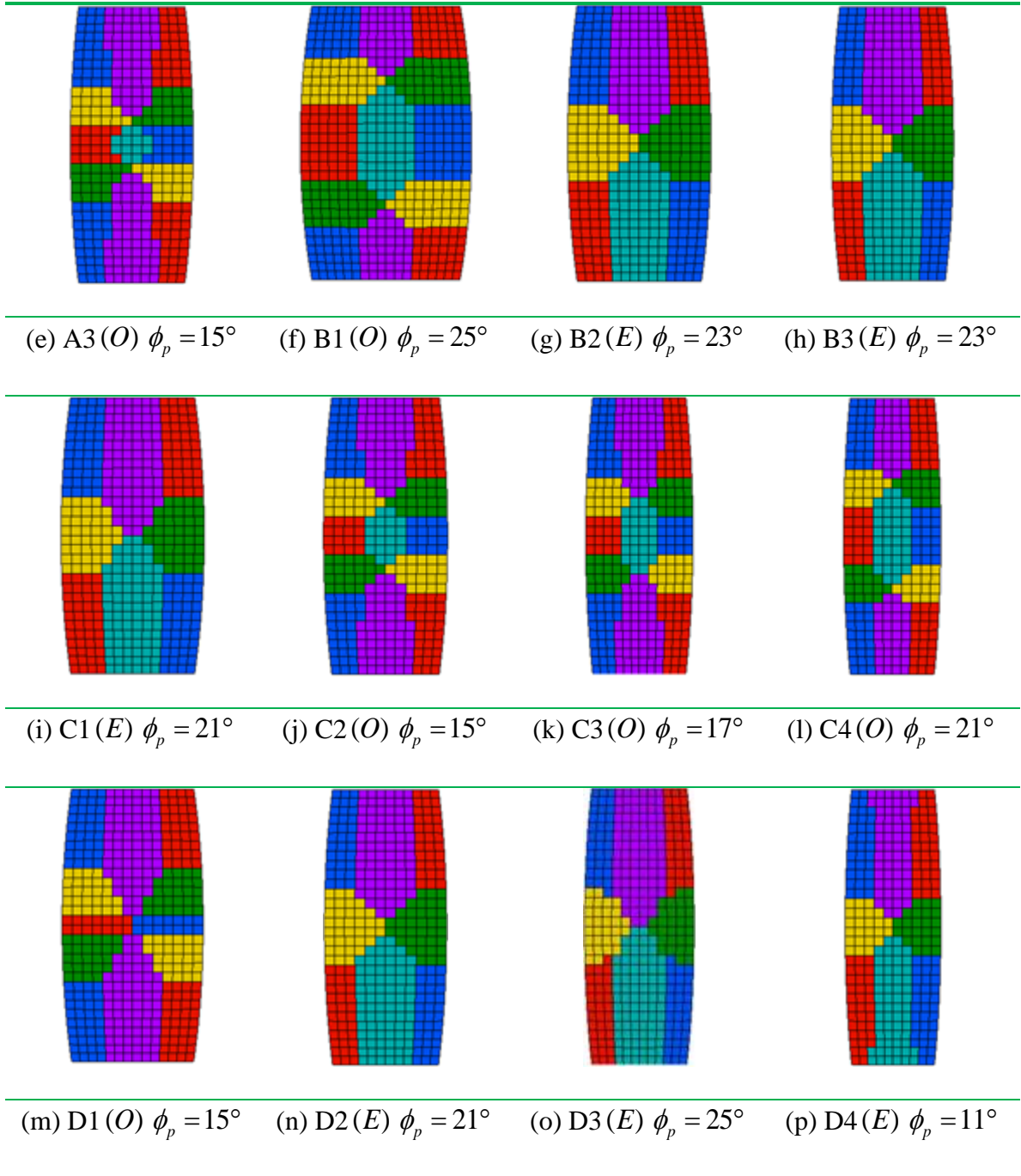


Figure 4-6 Chosen rotor designs of each design case

Torque characteristics for varying inclinational angle ϕ are evaluated by (4.7) for the chosen rotor designs in Figure 4-6, and compared for each group of stator Design A, B, C, and D in Figure 4-7. Design A0 is included in each group of the stator design to

compare torques of newly optimized designs against the existing spherical motor. Also, the required numbers of the EMs and PMs for each design are tabulated in Table 4-3 where (θ_x, ϕ_x) and (θ_z, ϕ_z) denotes the orientations where T_{x0} and T_{z0} occurs respectively. With the evaluated torque characteristics, three optimized designs are determined subject to the following considerations:

a) The best design regardless of complexity:

Consideration a) leads to Design D2 where an optimized design is chosen because of its largest output performance T_0 defined in (4.6).

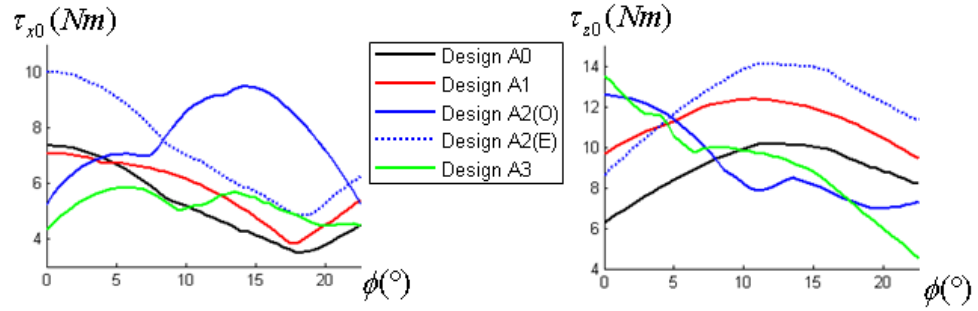
b) A good design considering the number of EM input channels

Consideration b) results in Design B2 among the simple designs (A1, B2, and C1), which shows reasonably a good output performance with only 60PMs and 16EMs (8 independent channel input)

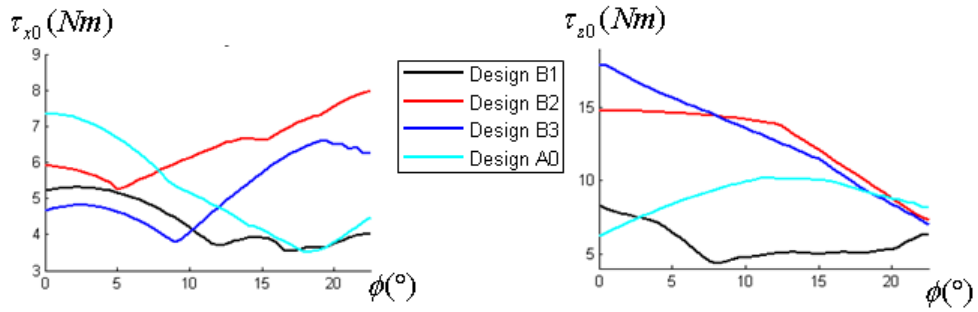
c) A good design which needs minimum modification from the existing design.

For consideration c), all types of Design A optimized with the existing stator are considered. While Design A2(O) gives the largest T_0 , it demands relatively complex rotor designs with 96 PMs. Comparing with A2(O), A2(E) shows 8.4% lower T_{x0} , but 24.2% larger T_{z0} with 60 PMs. A2(E) is chosen as an optimal design when considering the existing stator for performance improvement requiring minimal changes.

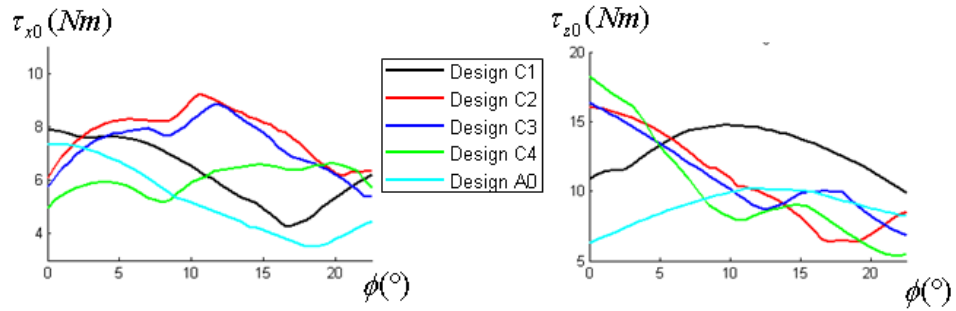
All selected optimal designs are written by bold red characters in Table 4-3, and full rotor designs are depicted in Figure 4-8.



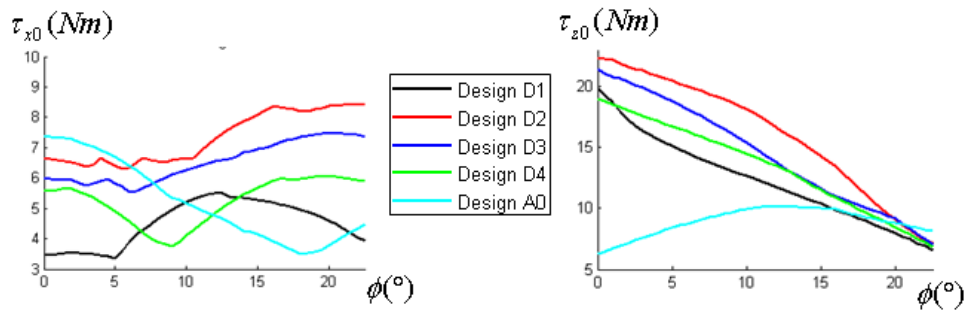
(a) Design A



(b) Design B



(c) Design C



(d) Design D

Figure 4-7 Evaluated torque characteristics of each design case

Table 4-3 Torque comparison of optimized designs

	$\theta_x(^{\circ})$	$\phi_x(^{\circ})$	$T_{x0}(Nm)$	$\theta_z(^{\circ})$	$\phi_z(^{\circ})$	$T_{z0}(Nm)$	EM	PM
A0	11.7	18	3.50	15	0	6.25	24	24
A1	1.1	17.8	3.74	18	22.5	9.42	24	50
A2(E)	11.9	18.2	4.81	0	0	8.62	24	60
A2(O)	10	22.5	5.25	5.6	19.3	6.94	24	96
A3	0	0	4.33	11.3	22.5	4.49	24	70
B1	7.5	16.7	3.50	0	8.2	4.30	16	80
B2	12.9	5	5.24	3.1	22.5	7.26	16	60
B3	0	9.2	3.77	8.8	22.5	6.98	16	70
C1	0	16.5	4.28	12	22.5	9.89	16	60
C2	10.5	0	6.10	0	16.9	6.38	30	112
C3	10.0	22.1	5.37	11.3	22.5	6.75	16	128
C4	8.7	0	4.96	10	22.1	5.38	16	144
D1	0	5.0	3.36	8.9	22.5	6.53	20	96
D2	6.3	5.8	6.26	2.5	22.5	7.08	20	70
D3	0	6.2	5.48	11.2	22.5	6.87	20	80
D4	0	9.0	3.73	10.0	22.5	6.85	20	90

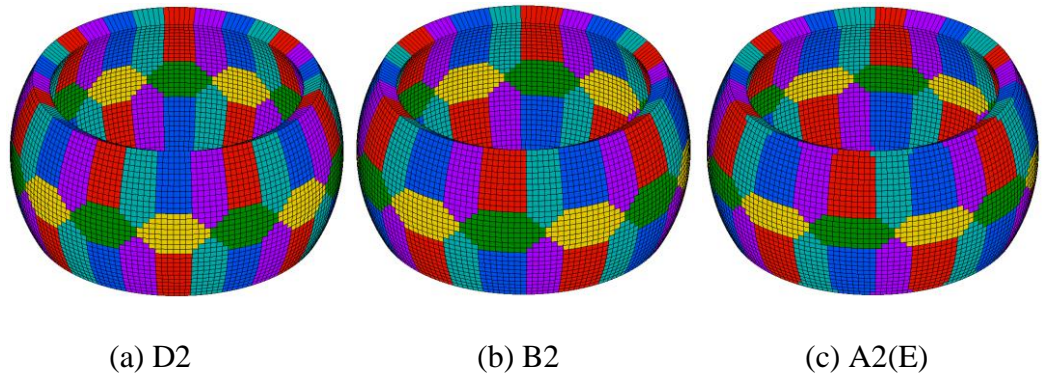


Figure 4-8 Optimized full rotor designs

4.1.3 Iron boundary and external loads

The optimized designs, D2, B2, and A2(E), are further analyzed with the presence of rotor iron boundary and external loads. Using the dimensions of iron boundary in Figure 3-8(b) and 3-13(b), the evaluated torques T_{x0} and T_{z0} including the rotor iron are

listed in Table 4-4 where Design A2(E) is shortly denoted by A2; and the torque improvement by the rotor iron is evaluated by

$$\Delta T_{x0} = \frac{T_{x0} - \hat{T}_{x0}}{\hat{T}_{x0}} \times 100, \quad \Delta T_{z0} = \frac{T_{z0} - \hat{T}_{z0}}{\hat{T}_{z0}} \times 100 \quad (4-8a, b)$$

where \hat{T}_{x0} and \hat{T}_{z0} denote evaluated torques without the rotor iron. For all cases, the rotor iron much improves both of spinning and inclinational torques; and it is more effective to improve spinning torque due to the closed rotor design space. The Halbach PM array in Design D2, B2, and A2 experience a larger improvement in the output as compared with the conventional PM configuration in Design A0.

Table 4-4 Torque comparison of the optimized designs with an iron boundary

	A0	A2	B2	D2
$T_{x0} (Nm)$	3.74	5.30	6.09	7.32
$T_{z0} (Nm)$	7.28	10.95	9.40	8.92
$\Delta T_{x0} (\%)$	6.86	10.19	16.22	16.93
$\Delta T_{z0} (\%)$	16.48	27.03	29.48	25.99

External loads

Figure 4-9 shows the external force acting on the rotor center caused by the additionally mounted mass m_{load} which causes an external torque varying with rotor inclinational angle ϕ . Assuming that the center of gravity g coincides with the rotation center O , the loading torque T_{load} are given by

$$T_{load} = h_z \sin(\phi) m_{load} g f_d \quad (4.9)$$

where the length of torque arm $h_z = 64.8mm$; and a design factor $f_d = 2$ assuming 50% torque loss for further design steps or real implementation.

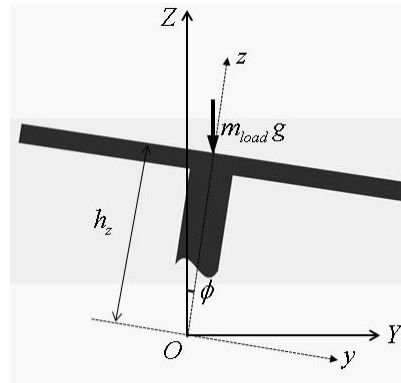


Figure 4-9 External loads on the spherical motor

The torque characteristics of the optimized designs with/without the rotor iron are shown in Figure 4-10 where the external torque caused by the mass (from 8 to 22kg) is denoted by green dotted lines on the right side of Figure 4-10(a); but the external force acting on the rotor center is not related to the spinning torque shown in Figure 4-10(b). As discussed in the results of Layout Optimization, Design D2 and B2 give superior performances for in both spinning and inclinational directions. Beside large T_{x0} and T_{z0} , these designs could yield relatively high inclinational torque at a large ϕ supporting more than 16kg (only PM rotor) and 18kg (PM rotor with iron) external loads. Furthermore, at a small ϕ , larger spinning torque supported by Design D2 and B2 is highly desired torque characteristic for the high speed continuous spinning M-DOF motors like a vehicle wheel. Additionally, using N42 grade PMs with residual flux density $\mu_0 M_{\max} = 1.3(T)$ instead

of initially assumed $\mu_0 M_{\max} = 1(T)$ can improve the performance by 30% from the simulated results without changing simulated torque patterns.

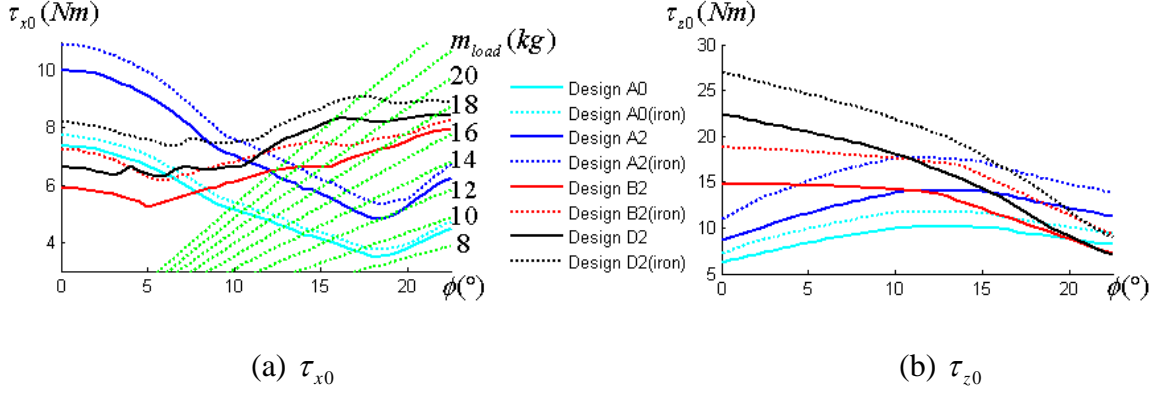


Figure 4-10 Performance of optimized designs subjected to an external loading

4.1.4 Weight efficiency

Design D2 and Design A0 (to compare the result with existing rotor design) are optimized again to improve the ratio of output-torque to (rotor PM) weight. For the linear optimization, an additional volume constraint (equivalent to weight constraint) is defined in terms of the density variable $\bar{\rho}$ and desired rotor volume v_r :

$$\mathbf{c}_v^T \bar{\rho} = v_r \quad (4.10)$$

where $\mathbf{c}_v = [V_{(1)}\mathbf{c}_\rho, \dots, V_{(N_v)}\mathbf{c}_\rho]^T$; $\mathbf{c}_\rho = [1 \ 1 \ 1 \ 1 \ 1 \ 1]$; $V_{(i)}$ denotes the volume of $(i)^{th}$ element; and $V_{(i)}\mathbf{c}_\rho^T \bar{\rho}_{(i)}$ gives the volume of the $(i)^{th}$ element used by the design variable. Dividing (4.10) with the volume of an entire design space V_0 , the volume constraint (4.10) can be expressed by a desired rotor volume ratio V_r :

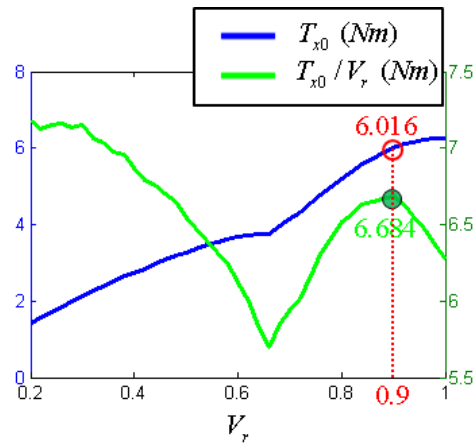
$$\mathbf{c}_v^T \bar{\rho} = V_r \quad (4.11)$$

where $\mathbf{c}_v = \mathbf{c}_v / V_0$; $V_r = v_r / V_0$ and $0 \leq V_r \leq 1$.

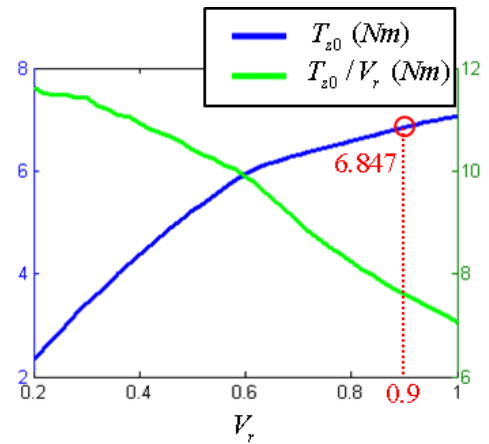
The optimized EM and PM layouts of the Design D2 and A0 are linearly optimized with the additional volume constraint in (4.11) while changing V_r between 0.2 and 1. On the integer programming step, the torque output (T_{x0} and T_{z0}) and volume efficiency (T_{x0}/V_r and T_{z0}/V_r) are evaluated. The results are shown in Figure 4-11 where left and right y-axes denote the torque output and volume efficiency respectively. Figure 4-11(a) and Figure 4-11(b) show the evaluated torque and its volume efficiency of the Design D2 for inclinational and spinning torques respectively, and Figure 4-11(c) and Figure 4-11(d) shows the evaluated results of the Design A0. From the results, an optimized design over the volume efficiency is chosen as follows:

- The spinning torque efficiency T_{z0}/V_r of Design D2 monotonically decreases with V_r . The inclinational torque efficiency T_{x0}/V_r has a highest value for $V_r \leq 0.3$, but the overall output torque will be significantly reduced by low V_r . To minimize the loss of torque, the local peak of the volume efficiency at $V_r = 0.9$ marked by green circles in Figure 4-11(a) is chosen as an optimized efficiency point. The newly optimized design with 10% volume reduction ($V_r = 0.9$) gives $T_{x0} = 6.016$ and $T_{z0} = 6.847$ leading to 3.9% and 3.3% torque reductions with respect to the original design ($V_r = 1.0$).
- The inclination torque efficiency T_{x0}/V_r of Design A0 monotonically decreases with V_r . The spinning torque efficiency T_{z0}/V_r exhibits a global peak at $V_r = 0.56$ leading to a new design with 44% volume reduction ($V_r = 0.56$). The

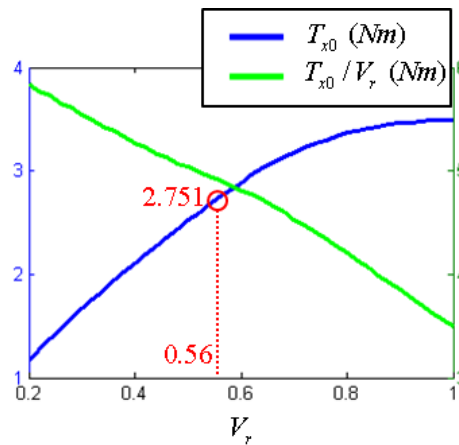
reduction of $T_{x0} = 2.751$ and $T_{z0} = 5.058$ for the newly optimized design is 21.4%, 19.1% comparing with the original design ($V_r = 1.0$).



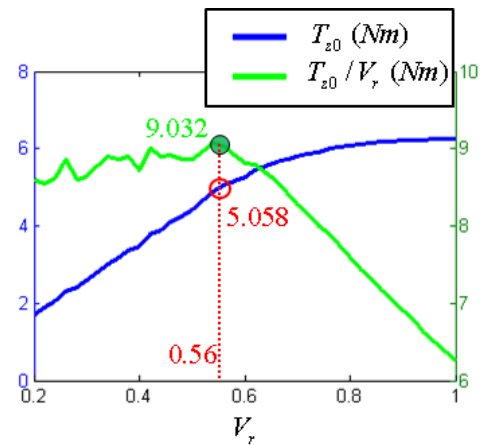
(a) Design D2: inclinational torque



(b) Design D2: spinning torque



(c) Design A0: inclinational torque



(d) Design A0: spinning torque

Figure 4-11 Torque output and volume efficiency

Figure 4-12(a) and (b) show the newly optimized designs of Design D2 and A0 respectively considering the torque-to-weight efficiency. As seen in the PM Halbach array of Design D2 ($V_r = 0.9$), the rotor design space at the junction of the connecting

PMs is less effective than other space; thus, the optimized PMs can be fabricated by block shaped PMs. For the Design A0 ($V_r = 0.56$) optimized by radially magnetized PMs, the optimization with the volume constraint empties the rotor design space where PMs are contacting each other. The newly optimized Design A0 for existing stator is much similar to existing rotor design.

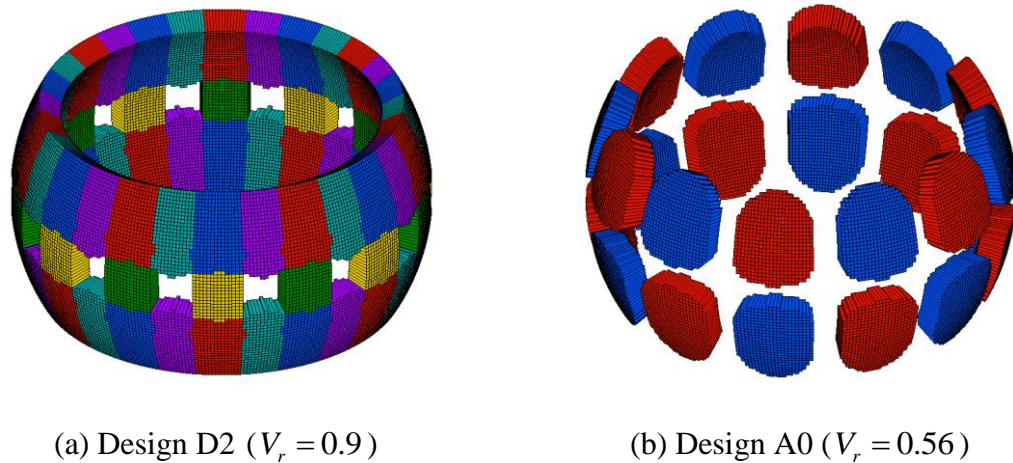


Figure 4-12 Optimized designs over the weight efficiency

4.2 LINEAR-ROTARY MOTOR

A new linear-rotary (LR) motor for 2-DOF motion is optimized by the Layout Optimization. A 3D CAD of a LR motor shown in Figure 4-13(a) is capable of both spinning and translational motion along the z -axis. Using similar designing steps for the spherical motor, the LR motor is separately optimized by 1-DOF rotary motor with an internal rotor and another 1-DOF linear motor as shown in Figure 4-13 (b); and 2D results are used to optimize the 3D LR motor. The design objective of the LR motor is to

maximize output torque and force for diameter 25.4mm (1inch) and z-axial length 152.4mm (6inch) while supporting 25.4mm (1inch) linear motion.

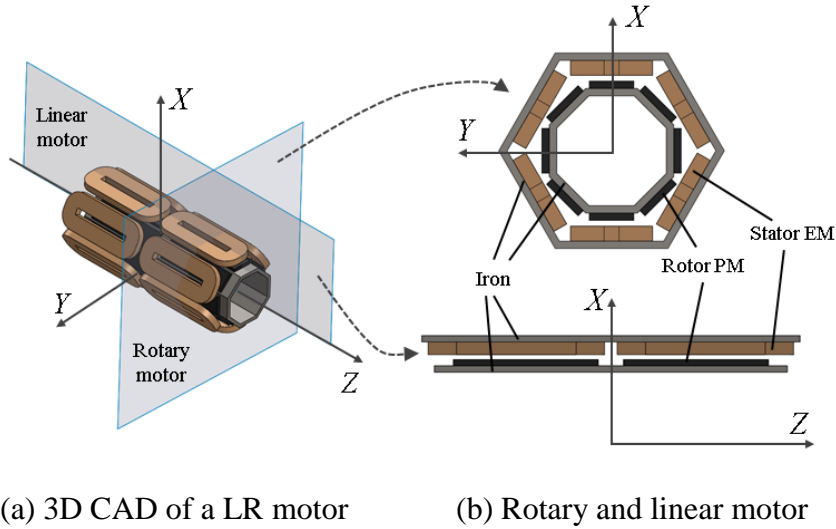
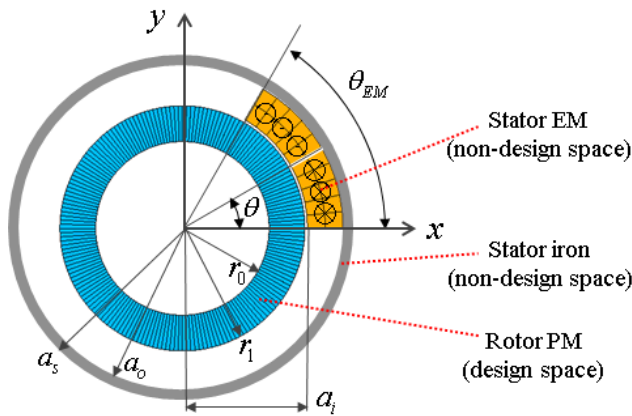


Figure 4-13 Design optimizations for a 2-DOF linear-rotary motor

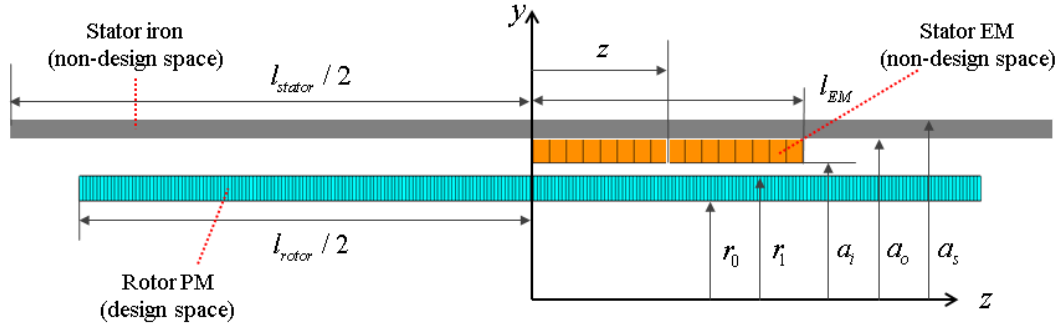
4.2.1 1-DOF rotary and linear motors



Geometry parameters (mm)
 $r_0 = 6.16$, $r_1 = 8.70$, $l_z = 2.54$,
 $a_i = 8.89$, $a_o = 11.43$, $a_s = 12.70$

Optimization parameters
 $N_v = 180$, $N_s = 900$,
 $\mu_0 M_{\max} = 1T$, $J_{\max} = 10^7 (A/m^2)$,
 $P = 720$, $\theta_d = 0.5^\circ$

Figure 4-14 Optimization parameters for the 1-DOF rotary motor



Geometry parameters (mm)	Optimization parameters
$r_0 = 6.16, r_1 = 8.70, l_x = 5.08,$	$N_V = 254, N_S = 1271,$
$a_i = 8.90, a_o = 11.43, a_s = 12.70,$	$\mu_0 M_{\max} = 1T, J_{\max} = 10^7 (A/m^2),$
$l_{stator} = 152.4, l_{rotor} = 127.0$	$P = 751, l_{d0} = 5mm, l_d = 1mm$

Figure 4-15 Optimization parameters for the 1-DOF linear motor

Figure 4-14 and 4-15 show the geometry and parameters for design optimization of a 1-DOF rotary and a 1-DOF linear motor. The objective is to find the preferred EM and PM layouts for the two moving directions of the LR motor. For both cases, the external stator in the non-design space has a number of EMs mounted on a stator iron, and the internal rotor PMs in design space are the target for to be optimized.

1-DOF rotary motor with an internal rotor (closed design space)

The 1-DOF rotary motor being optimized has a closed rotor, and its optimization is almost the same as the rotary motor with an external rotor case in Section 3.3. The electric current input in (3.20) can be used for linear optimization, and the angular size of an EM is defined by (3.23) for $N_{EM} = [4, 6, 8, 10, 12, 14, 16]$. The opposing located EMs are paired to reduce N_{inp} by means of 2-phase EM input. The optimization considers the

number of PM poles for $n_{pole} = 1, 2, \dots < 2N_{EM}$, and weight factors are set to $w_x = 0, w_y = 0, w_z = 1$, and $w_p = 1$ for $p = 1, \dots, P$. Figure 4-14 includes detailed parameters for the optimization.

1-DOF linear motor (open design space)

The optimization for the open rotor (or forcer) of the linear motor is similar to that in Section 3.3. The electric current inputs for even and odd poles are defined in (3.21) and (3.22) with φ and φ_{rotor} replaced by z and l_{rotor} respectively. The optimization considers $N_{EM} = [3, 4, \dots, 10]$ with the z-axial size $l_{EM} = l_{stator} / N_{EM}$, and its respective PM pole length $l_{pole} = l_{d0} + l_d \times [1, 2, \dots]$ for $l_{pole} < l_{rotor}$. The EM position z_{loc} is defined by (3.25) or (3.26) with φ_{EM} replaced by l_{EM} . The linear optimization uses $w_x = 0, w_y = 0$, and $w_z = 1$, and equal positional weight factors $w_p = 1$ for $p = 1, \dots, P$. The detailed parameters for the optimization are included in Figure 4-15.

Optimization result of the 1-DOF rotary motor

The minimum spinning torque T_{z0} of each (n_{pole} and N_{EM}) combination is evaluated for the linearly optimized designs. The evaluation results are plotted as a function of n_{pole} for each N_{EM} in Figure 4-16 where notably good designs are marked by an orange box including $(N_{EM}, n_{pole}) = (10, 14), (10, 12), (8, 10), (6, 10)$, and $(6, 8)$; and the best rotor designs for each of $N_{EM} = 6, 8$, and 10 are shown in Figure 4-17 where all rotors are optimized by a Halbach PM array; and internal rotors has longer radially magnetized

PMs than tangentially magnetized ones. Considering design compactness, $N_{EM} = 6$ and $n_{pole} = 8$ is chosen as an optimal layout being applied to a 3D LR motor optimization.

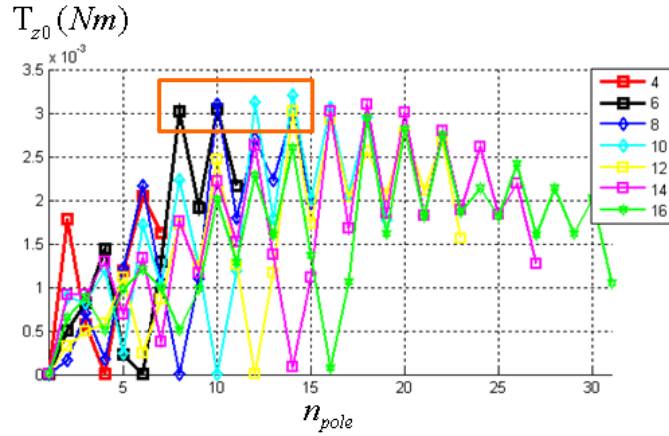
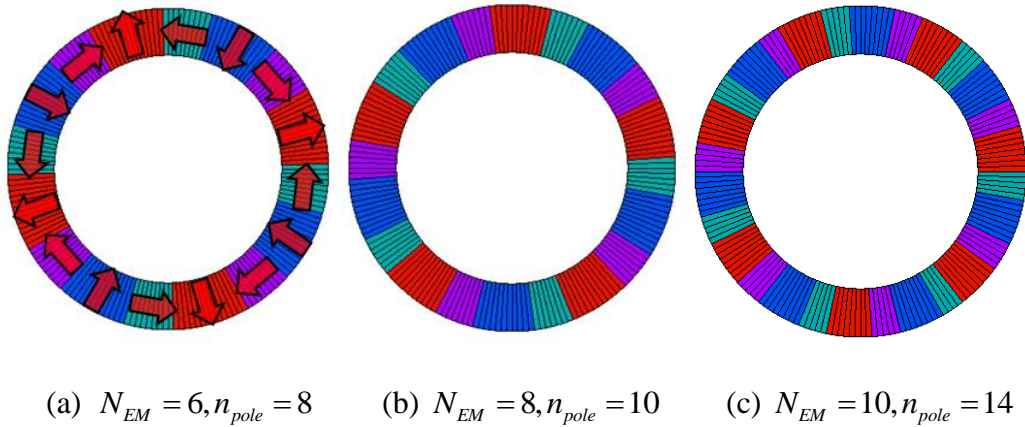


Figure 4-16 T_{z0} of linearly optimized designs for the 1-DOF rotary motor



(a) $N_{EM} = 6, n_{pole} = 8$ (b) $N_{EM} = 8, n_{pole} = 10$ (c) $N_{EM} = 10, n_{pole} = 14$

Figure 4-17 Optimized rotor PM designs of the 1-DOF rotary motor

Optimization result of the linear motor

The minimum z-axis force F_{z0} of the linearly optimized designs is evaluated for every combinations of l_{pole} and N_{EM} . The best F_{z0} for each N_{EM} is plotted in Figure 4-18 where $N_{EM} = 8$ and 10 cases (marked by orange boxes) show outstanding torque outputs.

The detailed F_{z0} of $N_{EM}=8$ and 10 designs as a functions of l_{pole} is plotted for odd (O) and even (E) PM poles in Figure 4-19 where the best combinations of EM and (O) PM poles, $(N_{EM}, l_{pole})=(8, 11.0mm)$ and $(10, 9.0mm)$ are denoted by orange boxes; optimized rotor designs with the magnetization of PMs (denoted by red arrow) are also depicted in Figure 4-20 where the $N_{EM}=8$ design requires a smaller number of PMs than $N_{EM}=10$ ones. Since both designs shows similar output force F_{z0} , considering the design compactness, $N_{EM}=8$ and $l_{pole}=(O)11.0mm$ is chosen as an optimal layout for a 3D LR motor optimization.

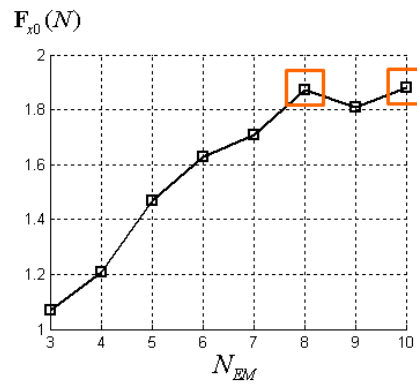


Figure 4-18 F_{x0} of optimized designs for the linear motor

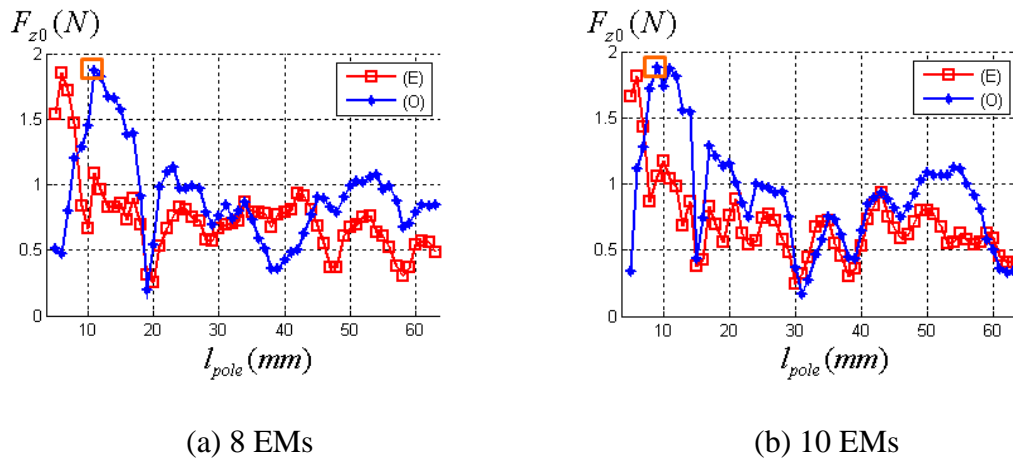
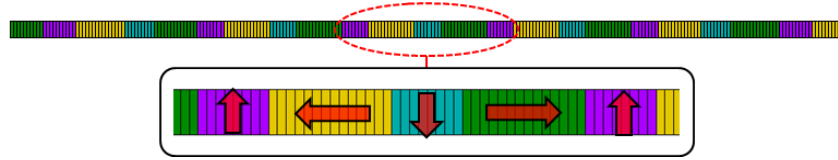
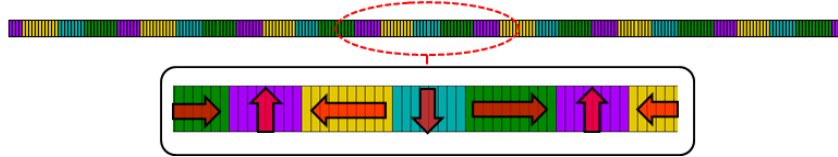


Figure 4-19 Integer programming for the design with 8 and 10 EMs



(a) Rotor design for $N_{EM} = 8$ and $l_{pole} = (O)11.00mm$



(b) Rotor design for $N_{EM} = 10$ and $l_{pole} = (O)9.00mm$

Figure 4-20 Optimized rotor designs for the linear motor

4.2.2 Linear-rotary motor

A linear-rotary motor is optimized by the Layout Optimization in 3D space. While changing weight factors for each of spinning and linear motions, the rotor design space is linearly optimized; and the maximum spinning torques of the rotor designs are compared for different external axial forces. From the 2D EM and PM layouts optimized for 1-DOF rotary motor and 1-DOF linear motor, the 3D stator design and rotor design spaces being optimized are defined in Figure 4-21(a) where the rotor PM design space is a hollow cylinder with $(r_1 - r_0)$ radial thickness and l_{rotor} length; and the non-design space stator is designed by the rectangular-cored 48 EMs and stator iron. The cross sectional view of the stator in Figure 4-21(b) shows the circular layout of the EMs along with the thicknesses of the EM and iron; and also the shape and size of the stator EM is shown in Figure 4-21(c). Most of the geometries are defined based on the geometric parameters of 2D optimizations in Figure 4-14 and 4-15.

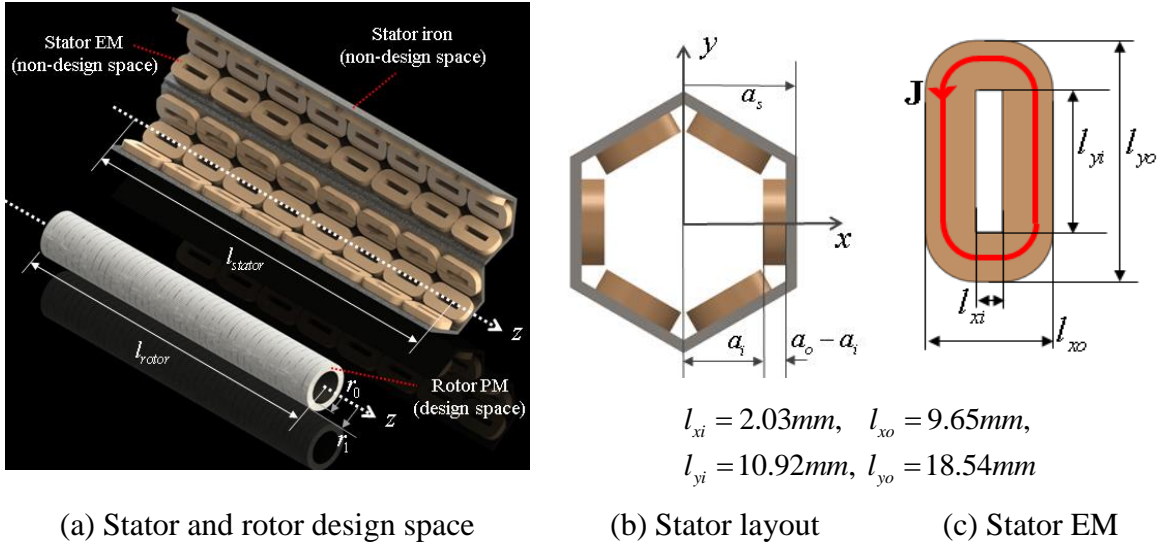


Figure 4-21 Stator and rotor design space for the linear-rotary motor optimization

Optimization parameters

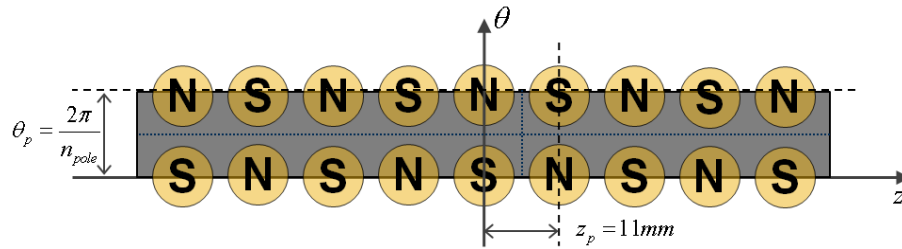
Taking advantages of the alternating magnetization (4.1) of the rotor PM along spinning direction, only 1/8 of the rotor PM design space is needed. The reduced rotor design space is decomposed into $N_V = 648$ volume and $N_S = 2658$ surface elements; which is then linearly optimized to maximize the weighted sum of the torque and force average evaluated at $P_\theta = 31$ spinning orientations and $P_z = 161$ linear positions (or $P = 4991$). The rotor PM is optimized by N42 grade PM with $\mu_0 M_{\max} = 1.3(T)$, and $J_{\max} = 10^7 (A/m^2)$ is used for all the torque and force computations.

Electric input current and torque evaluation

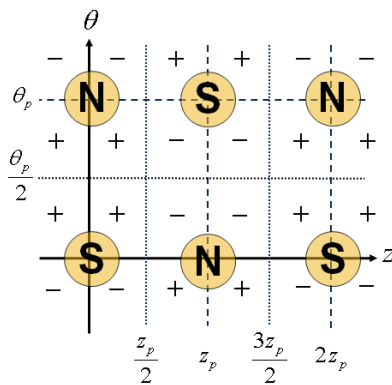
This optimization considers PM poles $n_{pole} = 8$ and layers $n_{layers} = 9$ for circular and longitude directions respectively. The PM pole layouts of the 1/8 sized rotor is

shown in Figure 4-22(a), which defines the sign of an EM input current for spinning torque T_z and linear force F_z as follows:

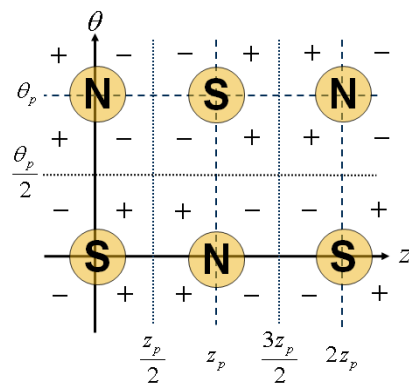
- The sign for T_z changes between PM layers, $z = \pm(2n-1)z_p/2$ for $n=1, \dots, 4$, and also at PM pole positions $\theta = 0$ and ϕ_p . The sign for T_z is shown in Figure 4-22(b), which defines the EM current input for the evaluation of spinning torque with $J_\theta = J_{\max} \text{sign}(T_z)$.
- The sign for F_z changes at every PM layer position $z=0$, and $\pm nz_p$ for $n=1, \dots, 4$, and also between PM pole position $\theta = \phi_p/2$. The predefined sign for the evaluation of linear force F_z is shown in 4-22(c); and it defines EM input current by $J_z = J_{\max} \text{sign}(F_z)$



(a) rotor PM pole layout



(b) EM input sign for T_z



(c) EM input sign for F_z

Figure 4-22 EM current input for the linear-rotary motor optimization

For a linearly optimized design, the net output torque and force $\mathbf{f} = [T_z, F_z]^T$ actuated by all stator EMs (with N_{inp} input channels) can be expressed by the multiplication of EM input $\mathbf{u} = [J_1, \dots, J_s, \dots, J_{N_{inp}}]^T$ and current-torque/force matrix \mathbf{K} :

$$\mathbf{K}\mathbf{u} = \mathbf{f} \quad (4.12)$$

where $\mathbf{K} = [\mathbf{k}_1, \dots, \mathbf{k}_s, \dots, \mathbf{k}_{N_{inp}}]$; and \mathbf{k}_s is an input current to z-axial torque and force relation by s^{th} pair of EMs . As the stator has $N_{inp} = 24$ for 48 EMs, the redundant current inputs are determined by solving a linear optimization problem at each rotor orientation:

$$\underset{\mathbf{u}, \mathbf{f}}{\text{maximize}} \quad \mathbf{c}^T \mathbf{f} \quad \text{subjected to} \quad \mathbf{K}\mathbf{u} = \mathbf{f}, \quad -J_{\max} \leq J_s \leq J_{\max} \quad (4.13)$$

where J_{\max} is the maximum input current; and the components of \mathbf{f} can be either specified constant or variable to maximize. To compare the maximum T_z over an external force $f_z = f_{ext}$, (4.13) is evaluated with $\mathbf{c} = [1, 0]^T$ and $\mathbf{f} = [T_z, f_{ext}]^T$; and the performances are compared with the minimum spinning torque, $T_{z0} = \min(T_z)$ for all range of the rotor motion while changing f_{ext} .

Optimization result of the linear-rotary motor

The rotor design space is linearly optimized for several combinations of force and torque weight factors (w_z, w_θ) , and it defines a directional weight factor $\mathbf{w}_d = [w_z \ 0 \ w_\theta]^T$. On the linear optimization, the design with the weight factor (1,0) only maximizes the z-axial force while the weight factor (0,1) only optimizes the spinning torque. Since the

scale of the torque is much smaller than that of the axial force due to the small torque arm of the rotor, a larger w_θ is used for the design optimized by a mixture of weight factors.

Figure 4-23 shows the evaluated minimum torque output T_{z_0} for different external loadings f_{ext} . The results show that the linearly optimized design with $(w_z, w_\theta) = (1, 12.5)$ is the best, and optimized design with only z-axial force, $(w_z, w_\theta) = (1, 0)$ also gives very close performance. However, the optimization only for the spinning torque $(w_z, w_\theta) = (1, 0)$ gives a relatively less effective design. Three rotor designs optimized with $(w_z, w_\theta) = (1, 12.5)$, $(1, 0)$, and $(0, 1)$ are compared in Figure 4-24 where small design differences are detected near the end of the rotor. Originally, it is expected that the composition of connecting PMs will be notably changed with a directional weight factor, but small differences on the optimized designs are observed.

As a results, the design optimized with $(w_z, w_\theta) = (1, 12.5)$ is chosen as the optimal design, and its torque output is shown in Figure 4-25 for $f_{ext} = 0, 1, 2(N)$. The optimized design gives small output force and torque caused by a low maximum current input $J_{max} = 10^7 (A/m^2)$, and higher performance can be achieved by using small EM wire and large input current. For example, 34AWG wire (0.160mm diameter) with 3A current gives 14.9 times larger current inputs, $J_{max} = 14.9 \times 10^7 (A/m^2)$; and the optimized LR motor can make 0.621(Nm) at all range of the rotor orientation while supporting external load $f_{ext} = 29.8(N)$.

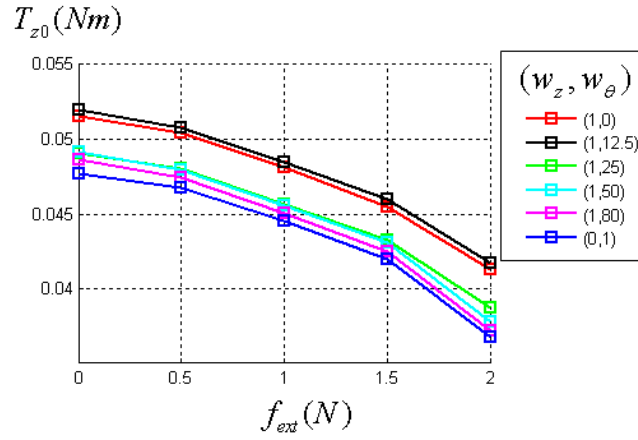
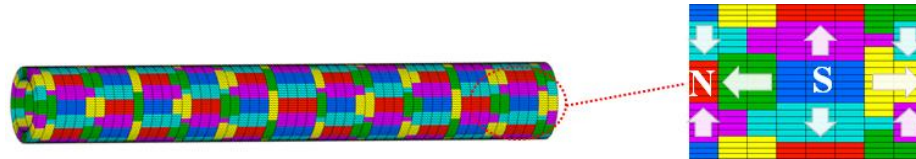
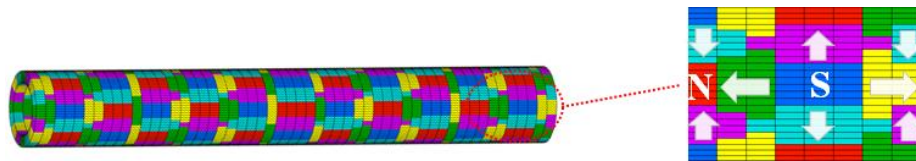


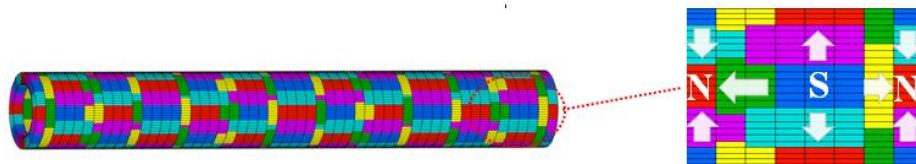
Figure 4-23 Evaluated minimum torque for different axial loads



(a) $(w_z, w_\theta) = (1, 12.5)$



(b) $(w_z, w_\theta) = (1, 0)$



(c) $(w_z, w_\theta) = (0, 1)$

Figure 4-24 Optimized rotor designs for the linear-rotary motor

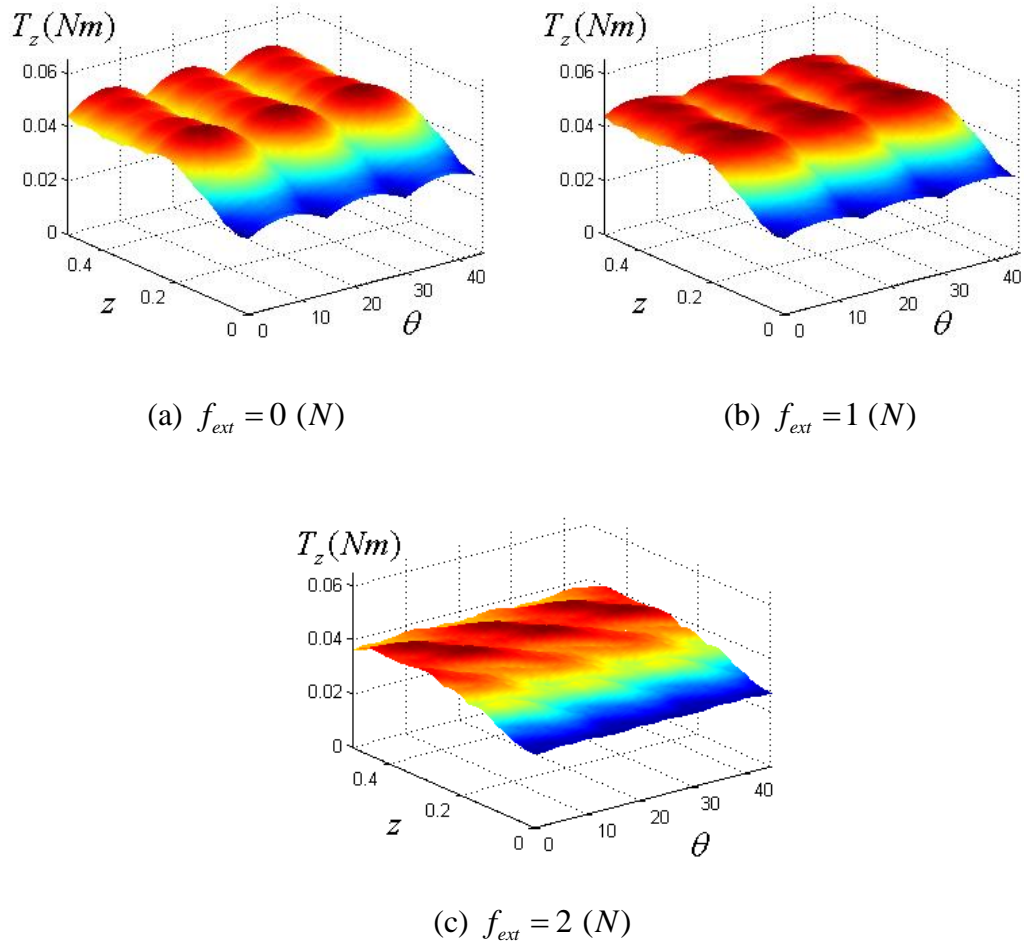


Figure 4-25 Torque output of the optimized designs for axial loadings ($w_z = 1, w_\theta = 12.5$)

4.3 DISK-SHAPED SYNCHRONOUS MOTOR

The rotor PMs and stator EMs of the disk-shaped synchronous motor (DSSM) are located circumferentially on two disks separated by a small air gap. Unlike a cylinder shaped conventional rotary motor; flat and thin shaped DSSM offers following advantages:

- 1) Extended work space to mount other materials
- 2) Hollowed inner space to easily assemble bearing or additional parts

- 3) Improved performance with increased torque arm
- 4) High torque with stacking up the motors along rotational axis

However, the main drawback of the DSSM is the increase in rotor inertia and bearing friction caused by the bulky rotor size limiting its usages for high-speed applications.

Two different DSSM motor designs, denoted as Large Design (LD) and Small Design (SD), consist of 48 rectangular EMs and 6 cylindrical EMs as shown in Figure 4-26(a, c) and Figure 4-26(b, d) respectively. The rotor PM design space in Figure 4-26(e) is optimized to find a set of preferred rotor PM designs for each of the predefined stator designs.

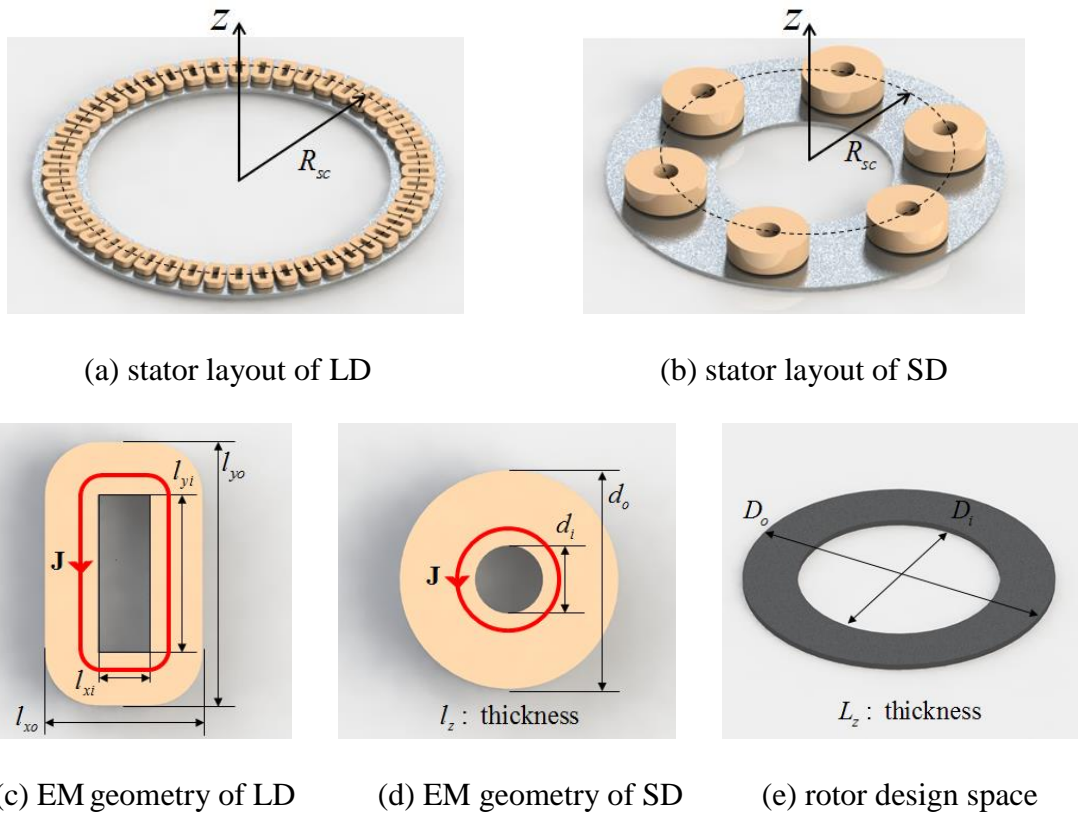


Figure 4-26 Design layouts for DSSM optimization

The design parameters for optimization are shown in Table 4-5 where d_g is air gap; J_{max} is the maximum input current for an EM; N_V and N_S are the number of decomposed volume and surface of the design space; D_i , D_o , and L_z are the size of each design space; and n_c , l_i , d_i , and b_i are DMC modeling parameters for EMs.

Table 4-5 Optimization parameters for DSSM

		LD	SD
EM	Geometry (mm)	$l_{xi}, l_{yi}, l_{xo}, l_{yo}, l_z, R_{sc}$ 10, 30, 30, 50, 10, 265	d_i, d_o, l_z, R_{sc} 9.78, 31.37, 9.53, 53.34
	$n_c, l_i, d_i/ b_i$	752, 3, 2	576, 3, 2
Rotor	Geometry (mm)	D_i, D_o, L_z 490, 570, 6	D_i, D_o, L_z 81.3, 132.1, 6.35
	N_V, N_S	11520, 47520	8640, 35280
Optimization parameters		$J_{max}=10^7(A/m^2), \mu_0 M_{max}=1(T), d_g=1(mm)$	

The closed rotor design spaces of DSSM are linearly optimized with EM inputs in (3.20). For LD and SD, the torques are evaluated at $P=1440$ and $P=720$ orientations respectively with 0.25° and 0.5° intervals. LD covers more number of poles for $n_{pole} = 2, 4, \dots, 96$ due to relatively large $N_{EM} = 48$, and SD is optimized for $n_{pole} = 2, 4, \dots, 48$.

When performing integer programming, the output performances are evaluated with 3-phase sinusoidal inputs in (4.14) and square wave inputs in (4.15) and compared among the linearly optimized designs:

$$i_s = i_{\max} \sin\left(\frac{N_p}{2}(\theta - \theta_s)\right) \quad (4.14)$$

$$\hat{i}_s = i_{\max} \text{sign}(i_s) \quad (4.15)$$

where $s = a, b, c$ denote each of 3-phase inputs; $\theta_a = 0$, $\theta_b = \theta_{s_0}$, and $\theta_c = 2\theta_{s_0}$ are phase difference defined by EM angle separation $\theta_{s_0} = 2\pi / N_{EM}$; and $N_{EM} = 48$ and 6 for LD and SD respectively. Since N_{EM} of the stator are multiple of 6 , two types of 3-phase EM wiring; types P and N as shown in Figure 4-27 are considered for the torque evaluation with 3-phase EM inputs. The optimized designs are chosen based on the net output torque and its ripple over the required number of PMs; and the CAD models of optimized designs are presented to simulate actual performance including iron rotor.



Figure 4-27 Two types of 3-phase EM inputs

4.3.1 Layout Optimization

For linearly optimized results, output performances are evaluated for minimum torque τ_{\min} and torque ripple $\tau_r = (\tau_{\max} - \tau_{\min})$ with sinusoidal 3-phase inputs, and $\hat{\tau}_{\min}$ and $\hat{\tau}_r$ with square wave 3-phase inputs. Notably effective designs of LD and SD are respectively listed in Table 4-6 and 4-7. All results commonly show that the square wave input always makes larger minimum torque, but also has larger torque ripples. The sinusoidal input offers much small torque ripple with reasonable torque magnitude, and its torque characteristics are highly desired as a rotary motor. Integer programming is performed to further narrow the choice of optimized LD and SD designs.

Optimization of LD

Table 4-6 shows four effective designs; two for type P, and two for type N connections. Comparing with other designs, Designs B and D show superior performances among all types of torque. The optimized rotor designs of B and D are shown in Figure 4-28 where either of PM polarities or magnetizing direction is depicted from the view of stator. Clearly, Halbach PM arrays on the optimized rotor design reinforces air gap flux, and it improves overall output torque. While the size of PMs are different for both cases, the optimized rotor designs are quite similar to each other; and it can be easily designed by commercially available bar shaped-PMs due to the large radius of the design space. Also, simulated torques of Design B and D are also compared in Figure 4-29 for different spinning angle θ ; and it shows Design B makes slightly better output, but both designs can be regarded to have similar torque performances. Considering less number of the PMs in Design B, its CAD model will be developed to simulate the performance loss during the actual motor design.

Table 4-6 Output torques of optimized LD

Design	A	B	C	D
Input type	P	P	N	N
$n_{pole} (N_{PM})$	32(64)	64(128)	16(32)	80(160)
$\hat{\tau}_{min}$	82.65	122.58	38.81	120.35
$\hat{\tau}_r$	27.31	20.66	58.87	19.97
τ_{min}	68.82	105.43	32.85	103.84
τ_r	2.51	1.86	24.96	0.98

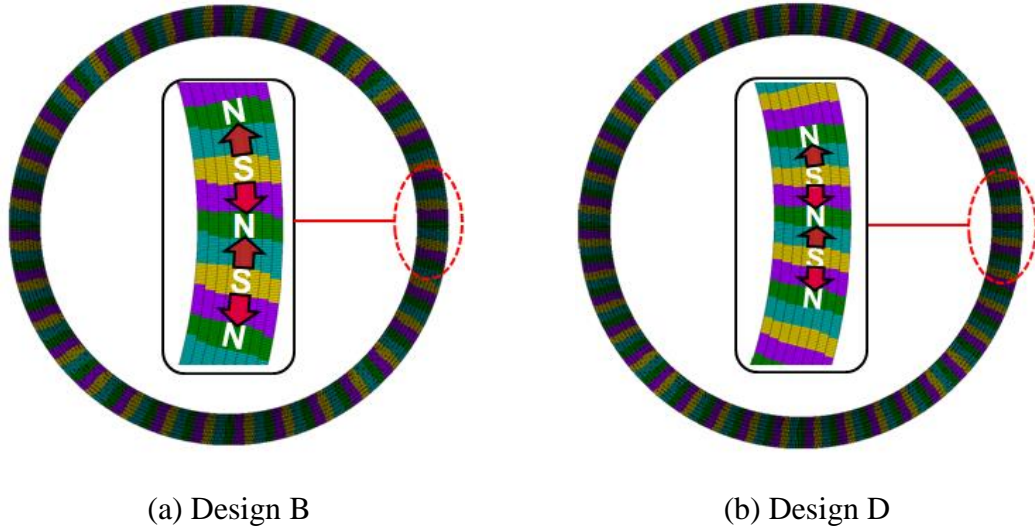


Figure 4-28 Optimized rotor designs for optimized LD

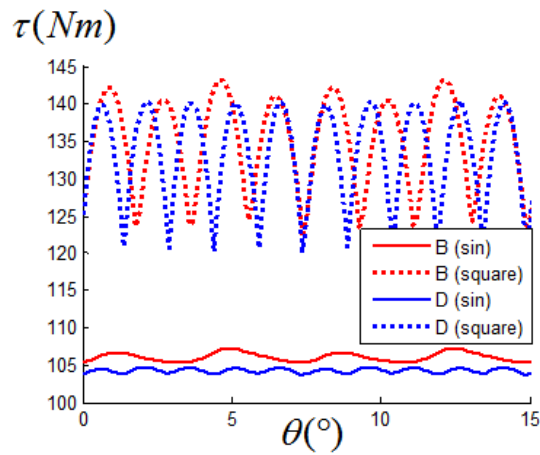


Figure 4-29 Simulated torque for optimized LD

Optimization of SD

Table 4-7 shows eight effective designs: four for type P, and four for type N connection. In view of torque output, Designs C, E, and F show similar performance but have a better efficiency than the others. The detailed optimized rotor designs are shown in Figure 4-30 where the small radius of the design space causes significant distortion of

the optimized PM shapes for small number of PMs. Figure 4-31 compares the simulated torques of the optimized designs for different spinning angle θ ; and all designs show similar performance, but design F gives about 4% larger torque than Designs B and E. Design C is chosen as an optimized design since it shows reasonably good performance, and its optimized rotor PMs can be effectively fabricated using commercially available bar-shaped PMs. A CAD model of Design C, being experimentally implemented in Chapter 5, is developed and analyzed in following section.

Table 4-7 Output torques of optimized SD

Design	A	B	C	D	E	F	G	H
Input type	P	P	P	P	N	N	N	N
$n_{pole} (N_{PM})$	4(8)	8(16)	16(32)	20(40)	10(20)	14(28)	22(44)	26(52)
$\hat{\tau}_{min}$	0.831	1.334	1.462	1.221	1.459	1.521	1.030	0.661
$\hat{\tau}_r$	0.806	0.316	0.242	0.185	0.258	0.257	0.204	0.190
τ_{min}	0.717	1.153	1.262	1.503	1.259	1.313	0.882	0.572
τ_r	0.292	0.002	0.016	0.001	0.007	0.018	0.044	0.065

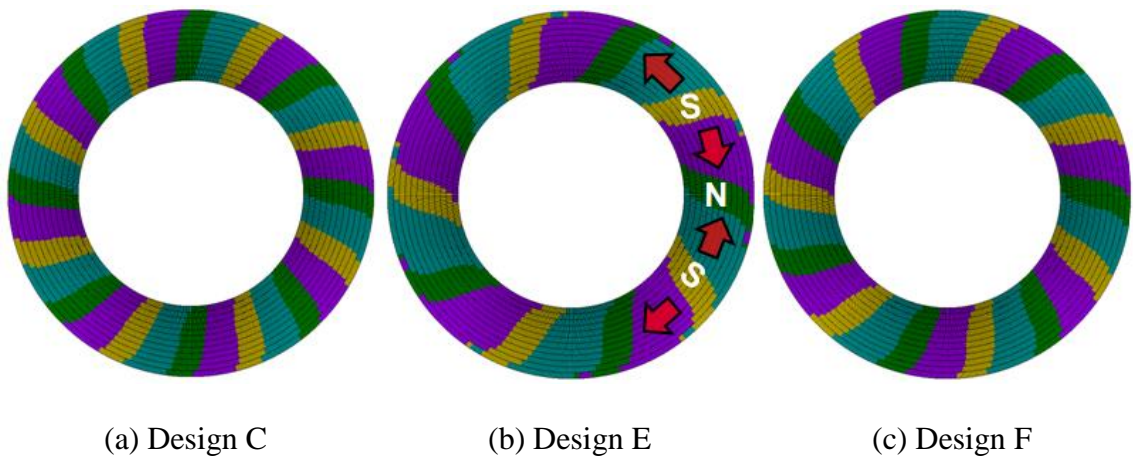


Figure 4-30 Optimized rotor designs for optimized SD

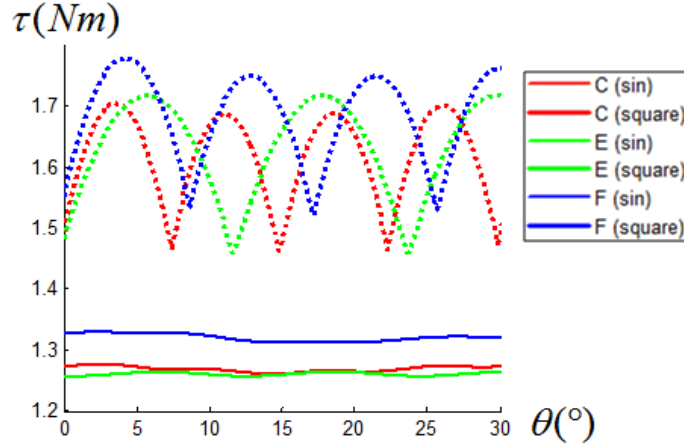


Figure 4-31 Simulated torque for optimized SD

4.3.2 Torque simulation of CAD model

The CAD model for Design B of LD and Design C of SD are developed by same sized bar-shaped PMs. The geometry of pole and connecting PMs are shown in Figure 4-32 where red and blue volumes denote north and south poles of the PMs. The LD and SD uses PMs respectively sized by $L_x \times L_y \times L_z = 10.16 \times 39.88 \times 6$ and $6.35 \times 25.4 \times 6.35$ (mm³). The developed CAD models of the large and small rotors are respectively shown in Figure 4-33(a) and (b) where the rotor volumes are almost fully filled by 128 PMs and 32 PMs respectively to minimize the performance loss from unused rotor space. On the torque analysis of CAD models, rotor irons with thickness 3mm for LD and 0.125in for SD designed by 1018 steel with relative permeability $\mu_r = 925$ is considered. Also, the same electromagnetic properties, $J_{max} = 10^7$ (A/m²) and $\mu_0 M_{PM} = 1$ (T) are applied to compare and discuss performance loss caused by designing actual rotors. Simulated parameters for the DMC model of PM and rotor iron are summarized in Table 4-8.

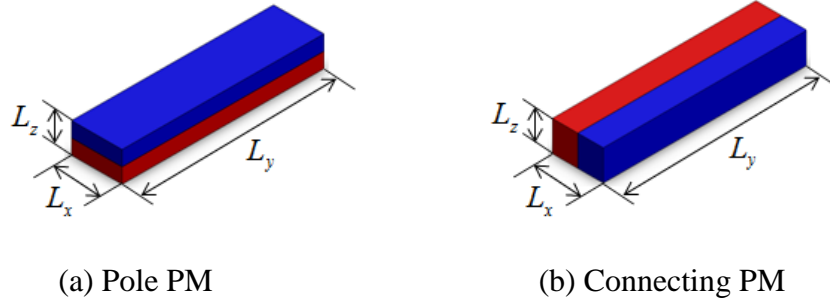


Figure 4-32 Bar-shaped PMs to design DSSM rotors

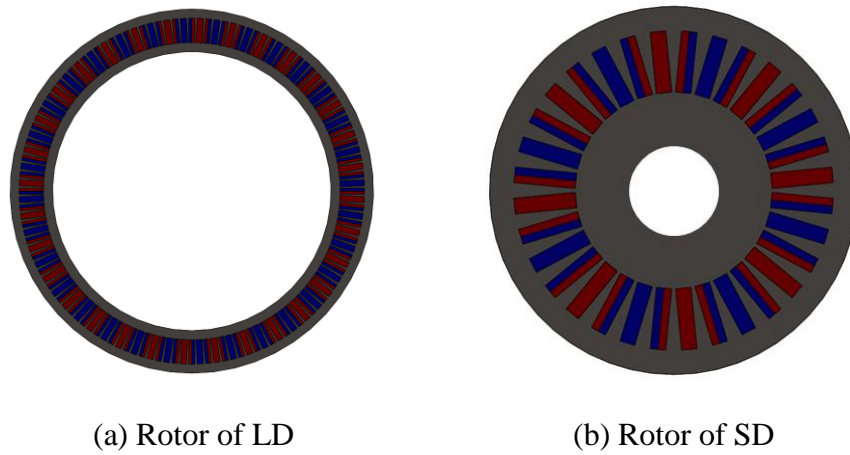


Figure 4-33 CAD model of optimized DSSM rotor

Table 4-8 DMC parameters to simulate the CAD of DSSM

	PM			Iron		
	n_c	l_i	d_i/ b_i	n_c	l_i	d_i/ b_i
LD	20	4	3	2048	5	3
SD	36	4	3	1536	5	3

The CAD model of a large DSSM is simulated by DMC to evaluate torque output for square wave and sinusoidal inputs. Figure 4-34 shows simulated net output torque, and each of 3-phase torques A,B, and C. The minimum net torque and its ripple are also tabulated in Table 4-9. The simulated results show that simplifying the optimized design

with the bar-shaped PMs causes 23.3% and 19.9% torque reduction while the rotor iron contributes to improve 34.7% and 33.1% of $\hat{\tau}_{\min}$ and τ_{\min} . Torque ripple of the CAD with sinusoidal inputs is twice of the optimized rotor, but still stays in small value comparing with torque output. For square wave input, torque ripple is reduced as net torque decreases.

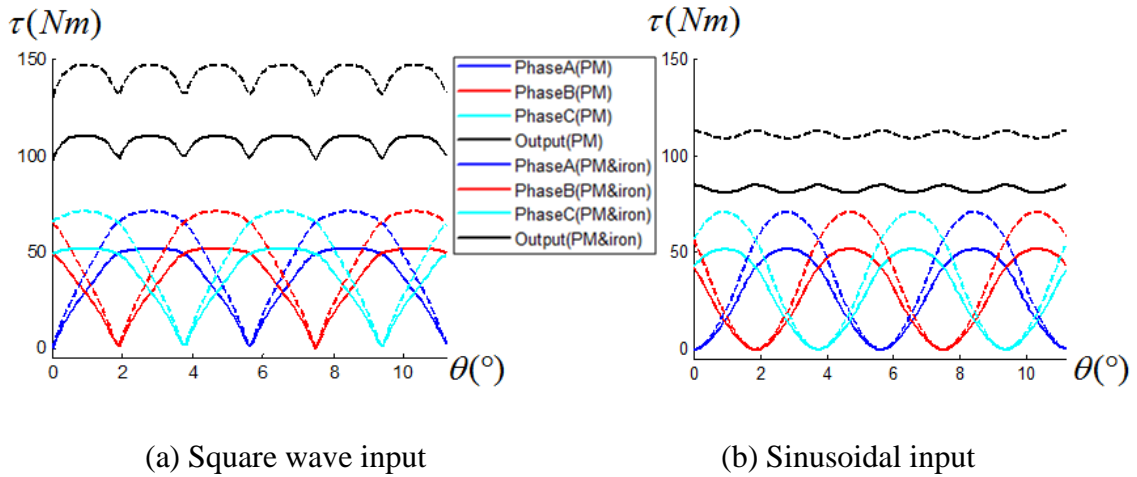


Figure 4-34 Torque response of CAD model of LD

Table 4-9 Output torques of CAD model of LD

Rotor	$\hat{\tau}_{\min}$	$\hat{\tau}_r$	τ_{\min}	τ_r
PM	98.21	12.07	81.15	3.9086
PM with iron	130.72	16.77	109.32	3.8966

For the CAD model of SD, output torques with square wave and sinusoidal inputs are also simulated by DMC. Figure 4-35 shows the torque for each of 3-phase and its net output; and the minimum net torque and its ripple is listed in Table 4-10. With the simplified rotor design with bar-shaped PMs, the output $\hat{\tau}_{\min}$ and τ_{\min} are decreased by 34.4% and 34.9% since the CAD model for the small rotor contains more unused space. Unlike the large design, the performance of this CAD model is merely improved by the

iron rotor; but it shows relatively small torque ripple. As overall torque outputs are decreases, torque ripples are also notably suppressed; and sinusoidal input gives negligibly small torque ripple, and it enables very smooth continuous spinning.

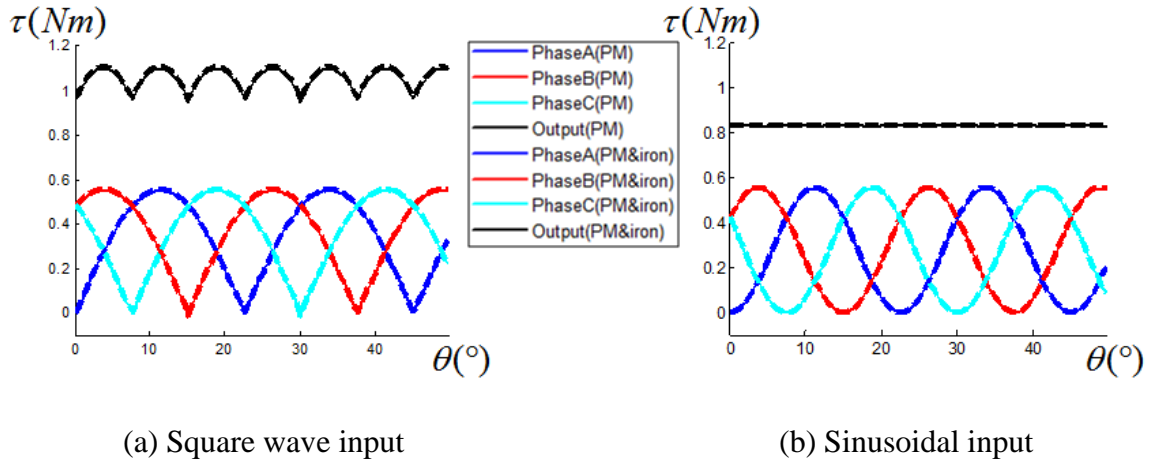


Figure 4-35 Torque response of CAD model of SD

Table 4-10 Output torques of CAD model of SD

Rotor	$\hat{\tau}_{\min}$	$\hat{\tau}_r$	τ_{\min}	τ_r
PM	0.9518	0.1510	0.8273	0.0045
PM with iron	0.9587	0.1516	0.8330	0.0046

The CAD model is developed for each of optimized rotor designs, and its performance loss caused by simplifying optimized rotor design is discussed. Also, it has been shown that performance improved by using rotor iron can be drastically changed by the choice of PM and EM layouts. While the designs are simulated with $\mu_0 M_{PM} = 1$, output torque of the actual motor can be improved by 45% with N52 grade PM, $\mu_0 M_{PM} = 1.45(T)$.

4.4 SUMMARY

This chapter has illustrated the DMC-based design optimization for three types of actuators; spherical, linear-rotary and disk-shaped synchronous motor. With layout optimization described in Chapter 3, a number of layout combinations of PM and EM are optimized, and chosen by critical design objectives such as output performance and design compactness. The CAD models of optimized designs are developed to evaluate performance changes during actual design implementation including iron boundary. On the optimization of the 3-DOF spherical motor, layouts of stator EMs and rotor PM poles are selected by on 2D optimization results in Chapter 3, optimized to improve torque characteristics under external loadings. Also, 2-DOF linear-rotary motor has been optimized to develop high torque rotary motor that can also support linear motion in the existence of linear external loading. Finally, DSSM have been optimized to develop high torque rotary motor for predefined stators of LD and SD. In Chapter 5.2, CAD model of optimized SD will be fabricated to experimentally validate optimized designs with measured air gap flux density and 3-phase torque output.

CHAPTER 5

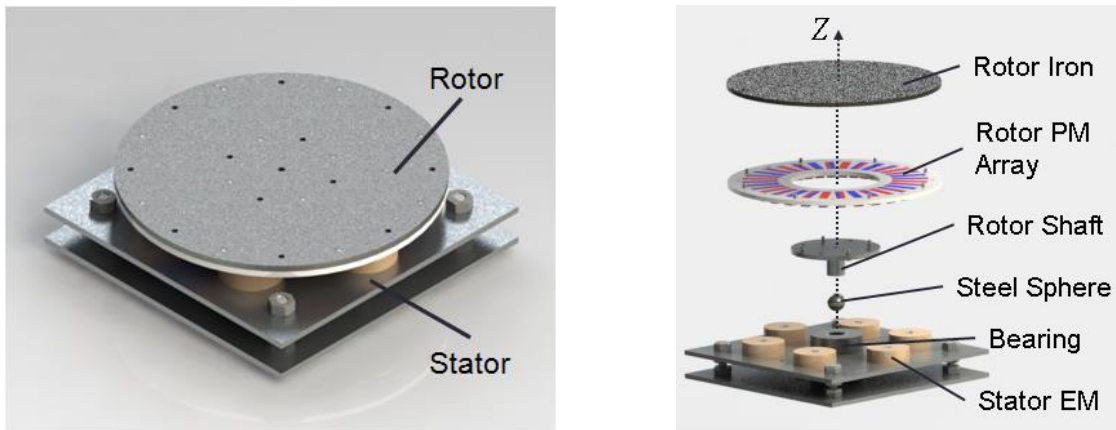
EXPERIMENTAL VALIDATION

This chapter presents the experimental results and validation for four different applications using the DMC models. The first examines the flux density and torque of a small disk-shaped synchronous motor (DSSM) optimized in Chapter 4; the custom-designed DSSM has been fabricated to demonstrate design optimization of a real actuator from the DMC models and for validating the computed results against measurements. The second is an analysis of an existing 3-DOF PM spherical-motor (PMSM) orientation stage [27, 66], where experimental data are available for comparison. The third analyzes the restoring magnetic torque between the magnetic wheels of a flexible mobile node (FMN) [69] and the iron bridge surface on which the FMN moves and turns around a tight corner. Finally, a PM linear synchronous motor (PM-LSynM) is analyzed using the DMC modeling method.

5.1 DISK-SHAPED SYNCHRONOUS MOTOR

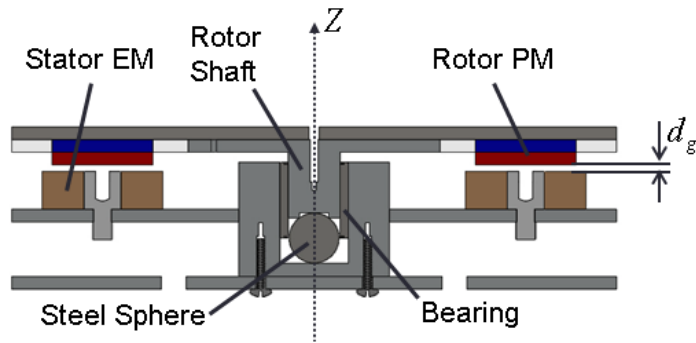
A DSSM consisting of a moving rotor with a Halbach array of 32 PMs (block-shaped, N52-grade), a stationary stator that houses 6 EMs (cylindrical, each with 800 turns), and a mechanical bearing, has been designed using the optimization results in Section 4.4 as shown in Figure 5-1(a). To help visualize the components making up the DSSM, an exploded view along the (spin) Z-axis and a sectional view are shown in Figure 5-1(b) and (c). The rotor PMs ($\mu_0 M_{PM} = 1.45T$) are tight-fitted in acrylic slots and

held in position by a thin iron rotor plate that eases the rotor assembly but is expected to have little effects on the output performance because of the Halbach PM arrangement. Six stator EMs are mounted on an aluminum plate which can be adjusted vertically by means of bolts/nuts for setting a specified air-gap d_g between the EMs and PMs. The rotor shaft is mechanically supported on the stator by means of a roller bearing and a steel sphere against gravity with little contact area to reduce friction.



(a) Isotropic view

(b) Exploded view



(c) Section view

Figure 5-1 CAD experimental setup of DSSM

Along with additional mechanical devices designed for measuring its air-gap flux density and 3-phase output torque, the DSSM experimental setup has been fabricated as shown in Figure 5-2(a). The rotor PM array and stator EMs are shown in Figures 5-2(b) and 5-2(c). The PMs are marked by N/S for PM poles and air-gap field direction for connecting PMs. The EMs grouped by A, B and C, and each group is serially connected to actuate the motor with 3-phase input.



(a) Motor assembly

(b) Rotor PM array

(c) Stator EMs

Figure 5-2 Experimental setup of DSSM

5.1.1 Experimental setup for measurement

Two different experimental setups are designed to measure torque and air gap flux density for validating the simulated results of the DMC models. During the experiment, the precision rotational stage (BR82-1 HWHR Instruments) attached to bottom of the stator, as shown in Figure 5-3, is used to specify the stator orientation. While the stator orientation is manipulated, the rotor orientation is constrained mechanically by a rotor arm assembly.

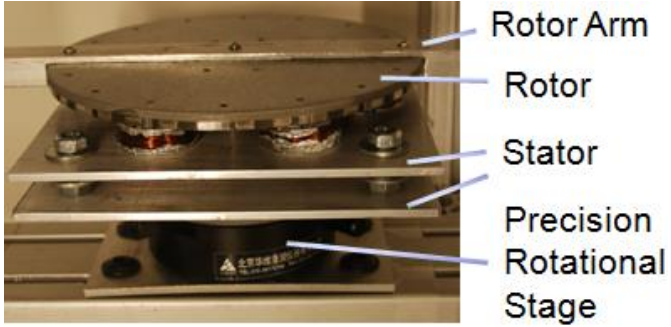


Figure 5-3 Precision rotational stage for DSSM experiment

The air-gap flux density due to the rotor PMs in the z direction was measured using 4 single-axis Hall-effect magnetic sensors (Asahi HG-362A), which were located $h_z = 5.3\text{mm}$ vertically from the PM surface and $h_r = 49.2\text{mm}$ radially from the rotational center. While the end of the rotor arm is secured to specify the rotor position relative to the stator, the flux densities were measured by means of a data acquisition (DAQ) module (NI USB-6008) for a revolution at 1 degree interval. For each increment, 1-second data taken at 5ms sampling rate was averaged.

A mechanical assembly has been designed to measure torque of the DSSM, where the rotor and its linked arm are constrained by two compression springs as shown in Figure 5-4 such that any displacement caused by an external torque or force can be measured using a micrometer. Figure 5-5 shows a CAD plane view for a closer look at the torque measurement setup and its parameters. For the electromagnetic torque T_z and external force f_w , which are caused by the current input flowing through the EMs and the external weight respectively, the spring force f_s restores the rotor assembly moves to a new equilibrium state. With a stiff spring which only allows a small displacement d_m , the micrometer-measured d_m gives the equations, (5.1), (5.2) and (5.3), for solving the

angular displacement θ_r of the rotor, the spring force f_s (that depends only on θ_r), and the torque T_z (that depends on both the angular displacement of the rotor θ_r and stator θ) from the moment equilibrium equation:

$$\theta_r = d_m / R_m \quad (5.1)$$

$$f_s(\theta_r) = k_s d_m R_s / R_m \quad (5.2)$$

$$R_s f_s(\theta_r) + T_z(\theta - \theta_r) - R_w f_w = 0 \quad (5.3)$$

In (5.2), the equivalent spring constant k_s (of the two springs) is calibrated using external weights on the rotor arm as shown in Figure 5-6. During calibration, a linear least-square fit for $T_z = 0$ in Figure 5-7 is sought to establish a relationship between d_m and f_s : $f_s = 4530.5d_m - 10.847$. With (5-2), the calibrated $k_s = 4530.5 \text{ N/m}$ of the combined two springs is slightly larger than twice the manufacturer specified spring constant of 4378.2 N/m (or 3.5% difference). With zero external force $f_w = 0$, T_z can be evaluated from (5.3) for a given stator orientation θ , where θ_r and f_s are computed from (5.1) and (5.2) respectively with measured d_m and calibrated k_s . This torque was measured with air-gap $d_g = 1.905 \text{ mm}$ and 1A current applied to each phase of EMs by a power supply (KEPCO BOP 50-2M).

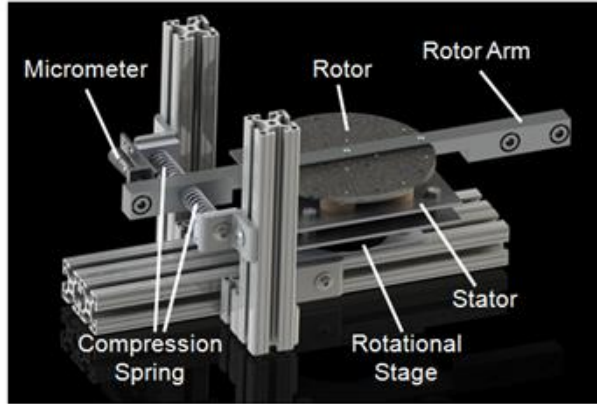


Figure 5-4 CAD mechanical assembly to measure DSSM torque

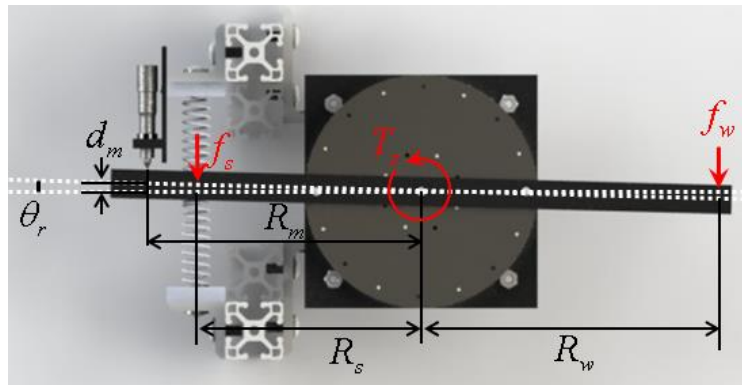


Figure 5-5 CAD torque measurement setup and its parameters

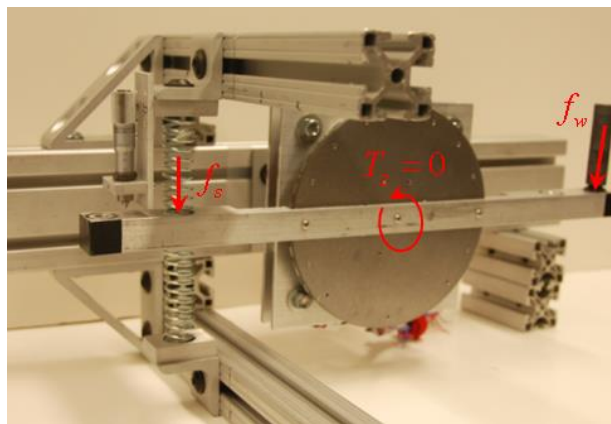


Figure 5-6 Spring calibration with external weights

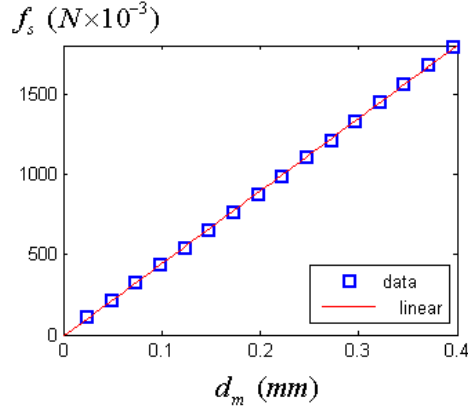


Figure 5-7 Spring calibration by a linear least-square fit

5.1.2 Model validation with experimental results

To validate DMC model, we compare simulated results with measured data obtained experimentally using the above described setups with the same DMC parameters in Table 4-5 and Table 4-8 for modeling PM, EM and iron. The current-density to current-magnitude ratio is $J/i = 7.49 \times 10^6 (m^{-2})$ for the 800-turn EM. Simulated flux densities and torques are compared with measured flux density in Figure 5-8 and Figure 5-9 respectively.

Air gap flux density

The computed and measured flux densities along the z-axis are compared in Figure 5-8 for all four sensors. Since the rotor is designed by same sized 32 PMs in Halbach array, periodic flux density has 16 peaks and 16 zero points under the center of pole and connecting PMs. Around peak points, measured field becomes little smaller than computed field. While such small errors can be caused by either sensor position error or

weaker PM magnetization, computed flux density clearly matches with measured data for most of orientations.

EM Torque

For each phase of EMs, simulated z-axial torques are compared against experimentally measured torques in Figure 5-9. While the result shows some phase differences which can be caused by hand manipulation of the rotational stage and shape errors of EMs, computed and measured torques of all phases well agrees with each other.

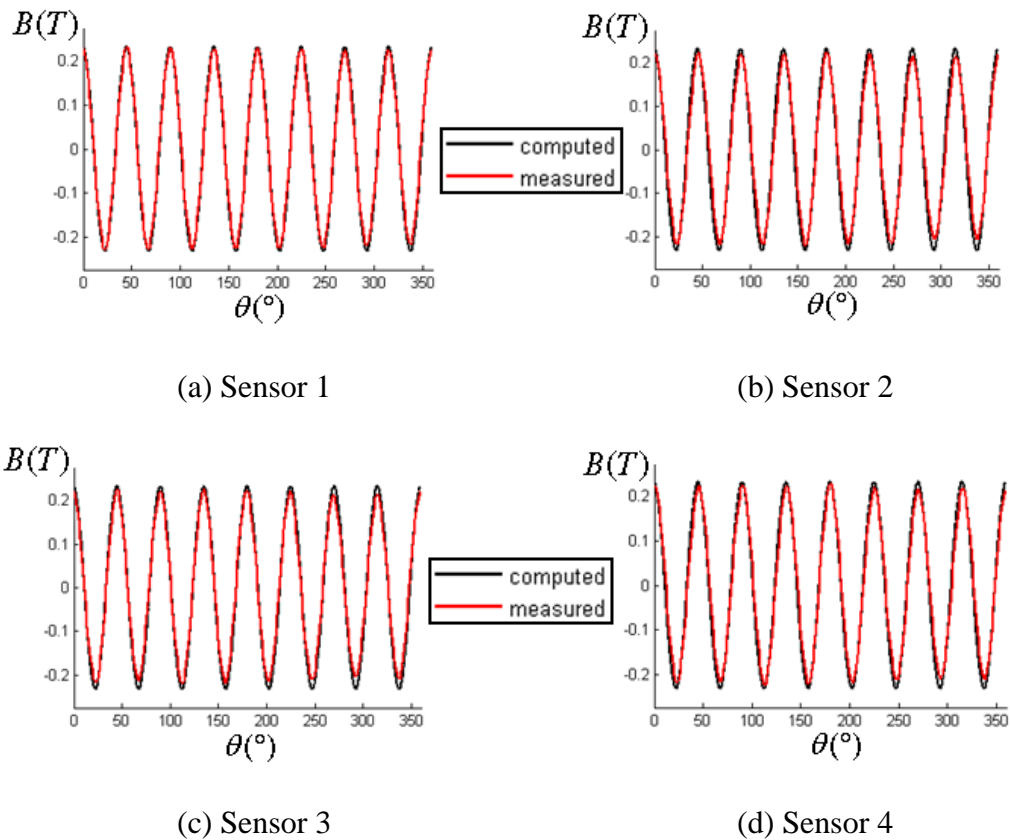


Figure 5-8 Comparison of DSSM flux density

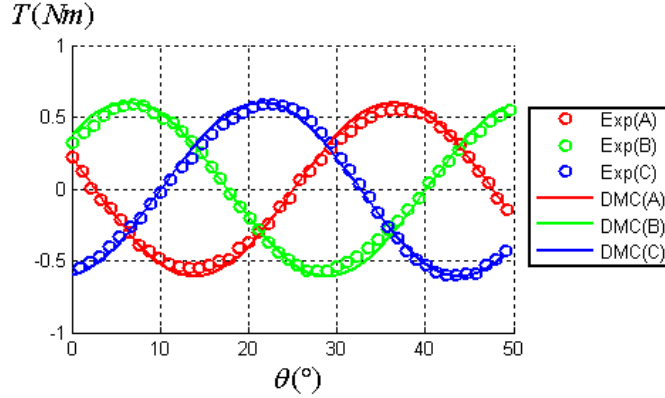
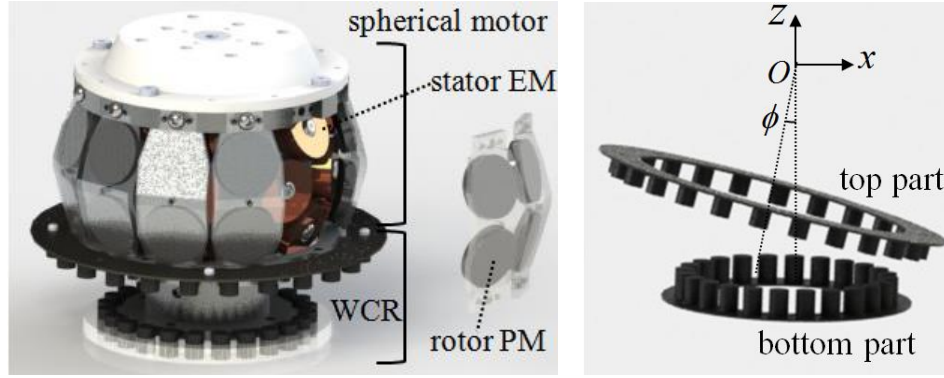


Figure 5-9 Comparison of DSSM torque

5.2 PM SPHERICAL-MOTOR (PMSM) ORIENTATION STAGE

The DMC model for an existing 3-DOF PMSM orientation stage was analyzed and validated against published experimental data [66]. Figure 5-10(a) shows a CAD model of the PMSM orientation stage, where two (top and bottom) rings of repulsive circular PMs forming a weight compensating regulator (WCR) are added to an existing spherical motor (that has 3 layers of 8 cylindrical EMs and 2 layers of 12 cylindrical PMs) to compensate for the gravitational effects on the orientation control. As shown in Figure 5-10(b), the WCR was supplementary to improve system stability with repulsive force, where the restoration torque increases as the inclinational angle ϕ increases and thus tending to stabilize the spherical motor control. To decouple the magnetic fields for orientation control of weight compensation, three shielding irons are added to the WCR; two iron rings separated by 0.25mm in top part, and one iron ring in bottom part.



(a) CAD model

(b) WCR

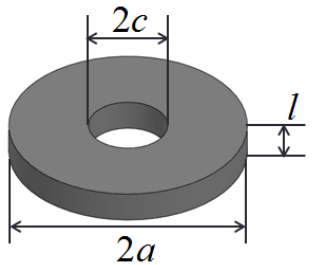
Figure 5-10 CAD model of existing PMSM orientation stage

5.2.1 Analysis of PMSM orientation stage

Given the geometries and electromagnetic properties of the PMSM orientation stage, three DMC models derived for its PM, EM and iron are listed in Table 5-21. While most of the mechanical structure of the spherical motor is non-magnetic, the WCR PMs are attached to a pair of shielding irons (the top shield was made up of two ring-like circular irons separated by $0.25mm$; and the bottom shield is an iron ring. On the top and bottom of WCR, each with 24 PMs are located along the circles with radii of $73.66mm$ and $49.53mm$, and WCR PMs are separated by $26.67mm$ at stable orientation $\phi = 0$.

In this simulation, the residual flux density of all PMs (N42 grade) is set to $\mu_0 M_0 = 1.32T$. Also, the rotor orientation is transformed by the rotation matrix $\mathbf{R} = \mathbf{R}_y(\phi)\mathbf{R}_z(\theta)$ where \mathbf{R}_z and \mathbf{R}_y are rotation matrix about z and y axes; θ and ϕ denote spinning and inclinational angles.

Table 5-1 Simulation parameters for PMSM orientation stage

		Geometry			DMC			
		$l(mm)$	$2a/l$	c/a	n_c	l_i	d_i/b_i	
Spherical motor	PM	6.35	5	0	20	4	3	
	EM	9.53	3.33	0.3	56	3	2	
WCR	top ring	PM	9.53	1	0	48	4	3
		iron1	1	175.26	0.768	144	5	3
		iron2	0.5	350.52	0.768	144	5	3
	bottom ring	PM	12.7	0.75	0	60	4	3
		iron	1	121.92	0.688	144	5	3

5.2.2 Magnetic field of rotor PMs

The radial components of the flux density measured by three hall-effects sensors located on the stator [66] are used to examine the validity of the simulated magnetic fields. Figure 5-11 depicts the sensor positions on the sectional view of the stator. Two sensors on the cores of EMs are located on $(r_s, \phi_s) = (s_{tb}, \mp\phi_{s0})$ where r_s and ϕ_s are radial and angular positions of sensors; ϕ_{s0} denotes EM angles at top layers. Another sensor attached to stator frame is position on $(r_s, \phi_s) = (s_m, 0)$.

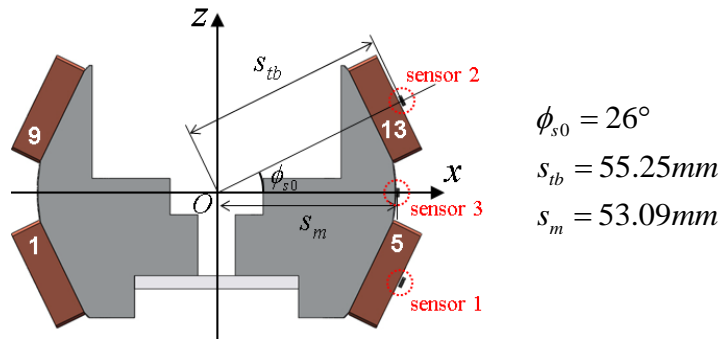
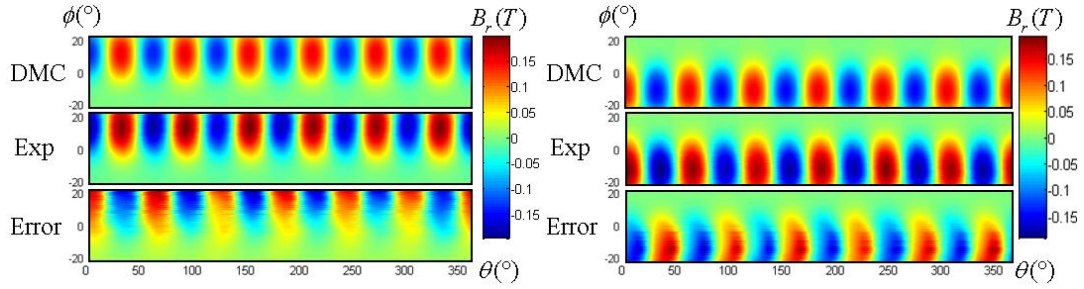


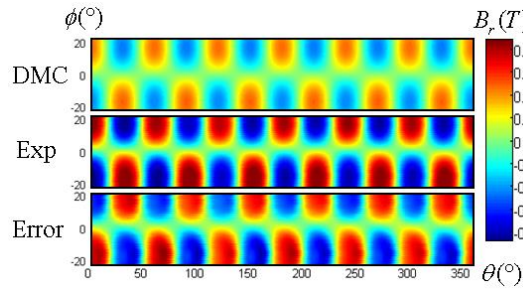
Figure 5-11 Hall-effect sensors to measure magnetic field of the rotor PMs

The radial magnetic field components of the rotor PMs that are housed in the non-magnetic structure of the spherical motor are simulated by the DMC model and compared with experimental data. In this simulation, the effects of the PMs and irons of the WCR were neglected since the top part of the WCR is sufficiently far from the sensors and rotor PMs. Figure 5-12 compares the flux density between the DMC model and experimental data and their differences for different spin θ and inclination ϕ angles. To more clearly represent the amplitude difference, the line plots of the flux density B_r at three inclinations, $\phi = 0^\circ$ and $\pm 20.16^\circ$ are shown in Figure 5-13. As compared in Figures 5-12 and 5-13, the DMC computed B_r seems to agree well with B_r data experimentally measured at Sensors 1 and 2 particularly at the stable equilibrium position of $\phi = 0$ where the difference in B_r is smallest. Some small phase differences occur in other positions could be caused by orientation/position errors of the sensors or rotor eccentricity. Unlike Sensors 1 and 2, a large difference between the computed and measured B_r was found by Sensor 3. The amplitude of experimental field registered by Sensor 3 is nearly double the theoretical field computed by the DMC model implying that Sensor 3 could be much closer to the rotor than the originally designed position. Although the flux density measured by Sensor 3 shows a large error, Sensors 1 and 2 cover the measured field of Sensor 3; it is reasonable to conclude that the experimentally measured fields agree well with the DMC simulation.



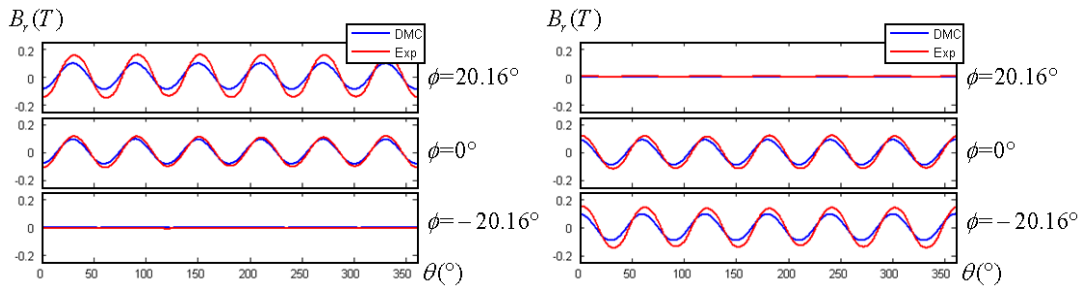
(a) B_r at sensor 1

(b) B_r at sensor 2



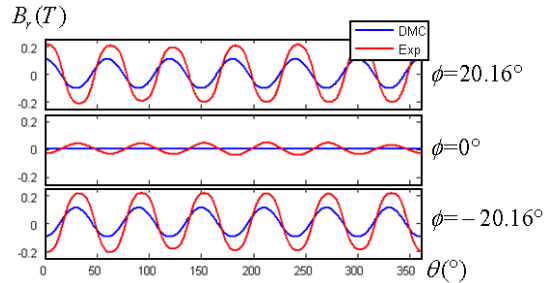
(c) B_r at sensor 3

Figure 5-12 Flux density comparison of rotor PMs



(a) B_r at sensor 1

(b) B_r at sensor 2



(c) B_r at sensor 3

Figure 5-13 Flux density comparison of the rotor PMs at $\phi = 0^\circ$ and $\pm 20.16^\circ$

5.2.3 WCR and EM torques

The WCR restoring and the PMSM actuating torque of the orientation stage are separately simulated using the DMC model and compared with published experimental results. Since the WCR involves no EM, the effects of PMs and irons are only a function of PM positions, the restoring torques are fully analyzed in terms of the rotor inclination angle ϕ . As compared in Figure 5-14, the DMC simulated torque well agrees to experimentally measured torque. Some errors at large inclinational angles can be caused by idealized material model overestimating the magnetization of the WCR iron. Also, during the experiment, undesired rotor motion can be occurred with high torque cases at large angles.

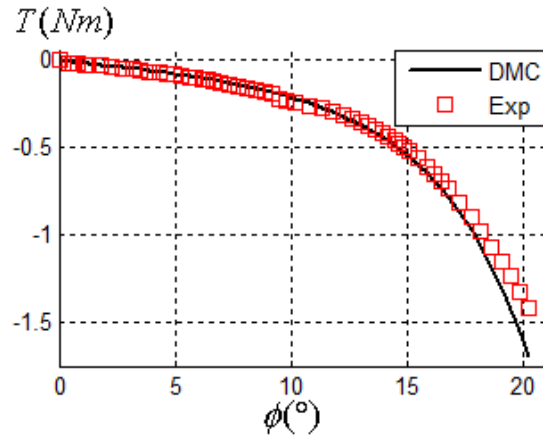
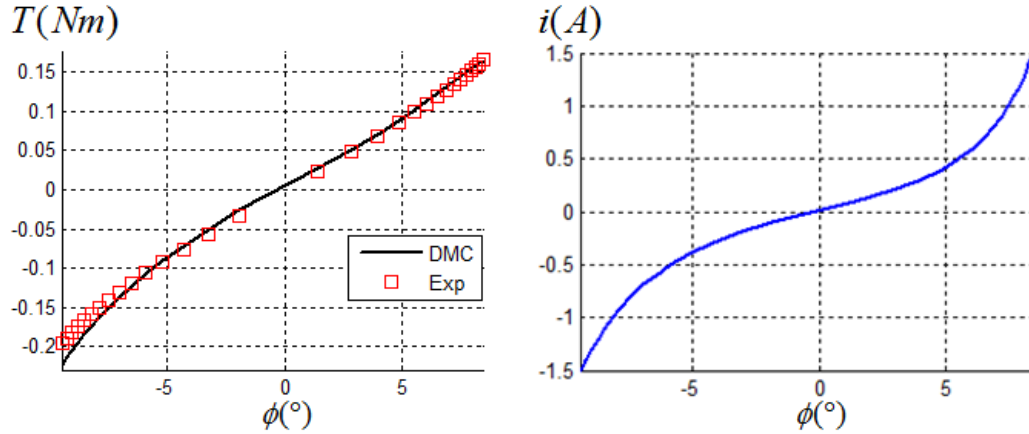


Figure 5-14 Torque comparison of WCR

For validating the PMSM actuating torque due to EMs, the DMC simulated torque is compared against experimental data in Figure 5-15(a) for the case where the current is applied to EM1 and EM13 in Figure 5-15(b). For the 800-turn EM, the current density $J(A/m^2)$ is given by $J = 0.7558 \times 10^7 i$. Since it was hard to overcome the

restoring torque of the WCR only with a pair of EMs for large angle experimentally, DMC torques have been simulated for available experimental range of the inclinational angles: $-9.4618^\circ \leq \phi \leq 8.4143^\circ$ where the EM pair moves inside the rotor volume at large negative angle, and moves out from the rotor at large positive angle. As compared in Figure 5-15(a), the results agree well each other, and also show that the torque at the negative angles is slightly larger than that of the positive angles since the EM pair is placed inside the rotor volume.



(a) EM torque

(b) EM current input

Figure 5-15 EM torque comparison of spherical motor

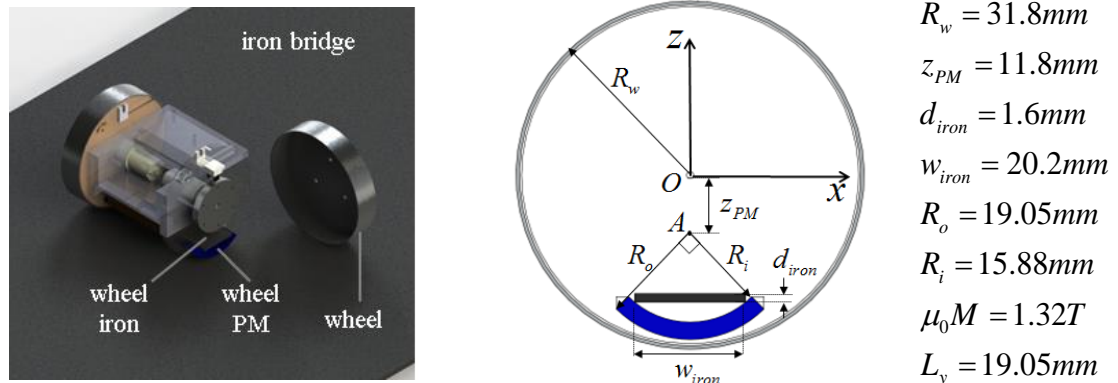
5.3 MAGNETIC WHEELS OF A FLEXIBLE MOBILE NODE (FMN)

The embedded PMs magnetically attract the wheels to the iron surfaces on which the FMN moves; the attraction could change drastically as the FMN navigates its orientation around various environmental iron geometries, and may subject to undesired vibration or hard to overcome sharp geometrical changes like iron corner. One way to handle these problems is to control the moving speed and actuating torque of the wheel motors. The interest here is to analyze the stabilizing torque at the contact point between the magnetic wheels and iron surface, and compares the simulation results with experimentally measured data.

5.3.1 Magnetic wheel design and torque experiment

Figure 5-16(a) shows the CAD model of an existing magnetic wheel located on an iron bridge surface. The application involves two magnet wheels connected by a flexible beam. In this thesis, the torque measurements of the front or rear wheels are separately studied. The detailed geometry and magnetic properties related to the wheel PM and iron are shown in Figure 5-16(b), where the residue flux density of the (N42 grade) arc-shaped-PM is $\mu_0 M = 1.32T$; and L_y is its length along the y-axis. The experimental setup to measure the stabilizing torque at the iron corner is shown in Figure 5-17. Using hanging weights, the magnetic wheel orientation and spring deformation at the equilibrium point are measured; and the torques between the wheel and iron surface can then be estimated from the 2D static force/moment equations: the x and z force equations and the y -axis momentum equation. With different weights, the corresponding torques,

positions and orientations of the magnet wheel are measured for several environmental encounters; plain surface, iron corner, and single iron-corner with one-side of the corner is non-magnetic.



(a) CAD model of the magnetic wheel (b) Wheel geometry and magnetic properties

Figure 5-16 Design of the magnetic wheel

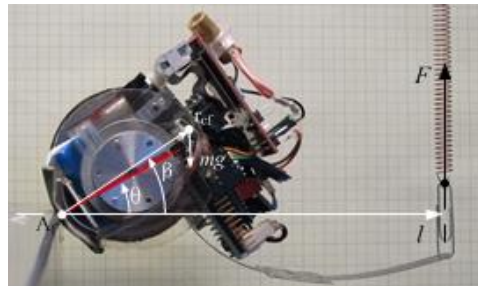


Figure 5-17 Torque measuring setup for magnetic wheel [69]

5.3.2 Torque simulation and validation

The DMC models are separately derived for the magnetic components of the magnetic wheel. The number of DMC n_c of the wheel PM and iron are set to 174 and 96; and the iron plate and corner are set to 990 and 1654. The DMC l_i and d_i / b_i are set to

4 and 3 for all components. To allow enough size to magnetic field propagation, the size of the iron bridge surface is set larger than $76.2\text{mm} \times 76.2\text{mm}$ with a 1.27mm thickness. The simulated torque of 1 wheel was doubled before comparing against experiment results with 2-wheeled magnet car.

In the analysis, the magnetizations of the wheel and bridge irons by the PM flux density must be solved simultaneously for a series of magnet car orientation. A large amount of computation would be needed depending on the number of simulating position and orientation of the magnet car. Instead of such a full analysis, the following steps are used in the analysis to avoid repetitive computations:

- 1) Arc shaped wheel PM is modeled with the DMC method
- 2) The DMC models of the wheel iron caused by the PM are solved
- 3) The bridge DMC model caused by PMs is solved for the wheel orientations
- 4) Calculate stabilizing torque for the wheel orientations

Since the wheel and bridge irons are separated by some distance at any orientations, the propagation of the magnetic fields between these irons are neglected enabling the independent analyses of the iron model in Steps 2) and 3). When analyzing the magnet car at many orientations, matrices (2.36) are built so that they can be repetitively used for all the orientations of interest. To enable this, the DMC locations of the PM for several orientations are applied when formulating the DMC iron matrices (2.36) and (2.37). Then, Step 3) is repeated under the condition that only specifying the external field of the moving arc PM. Figure 5-18 shows wheel positions used for iron matrices in the view of DMC assemblies. After solving for the irons, the restoring torques at the contact points can be simulated by (2.14).

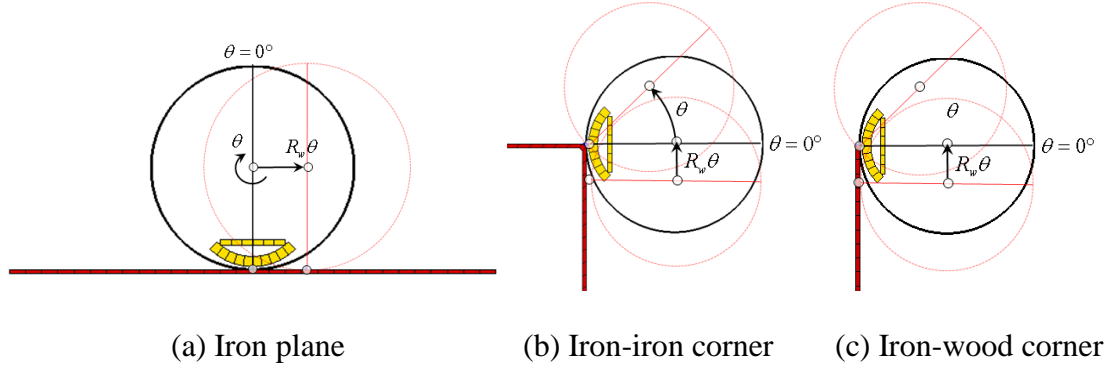
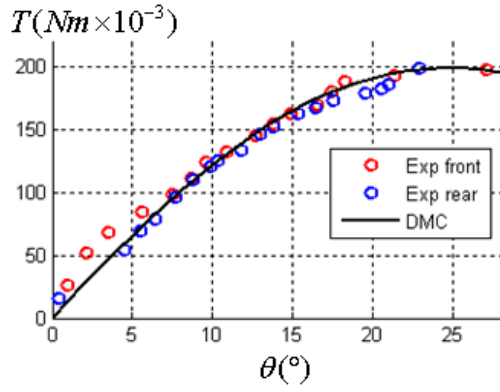


Figure 5-18 DMC assemblies for various wheel orientations

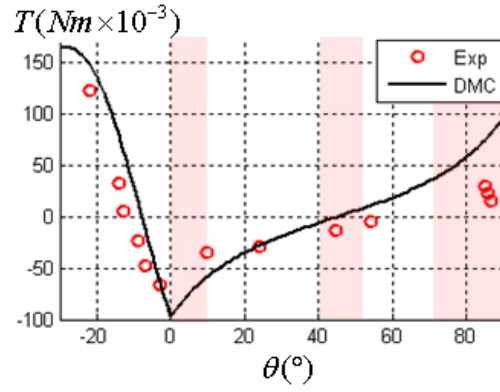
The DMC simulated stabilizing torques for the front and rear wheels are compared with experiment data in Figure 5-19(a); both well matches each other. The restoring torque of the magnet wheels on the iron plane grows as θ increases as the PM tends to restore its stable point $\theta = 0^\circ$ but starts to decrease around $\theta = 25^\circ$ when the separation between the PM and iron surface becomes large.

The measured and simulated torques around the iron-iron corner and iron-wood corner are compared in Figures 5-19(b) and (c) respectively; the overall trend agrees well with each other. Some discrepancies can be observed around $\theta = 0^\circ$ where the torque experiences a sharp change, and between $\theta = 40^\circ$ and $\theta = 50^\circ$ where the highly unstable magnetic system presents a challenge to measure the magnetic restoring experimentally by open-loop control of the magnetic wheel and is the primary cause of measurement errors as reported in [69]. For example, the theoretical torque at $\theta = 45^\circ$ for the case of the iron-iron corner should be zero due to the symmetry of the arc-shaped PM. Also, the rounded corner of the iron plate can caused the discrepancies of torque patterns between

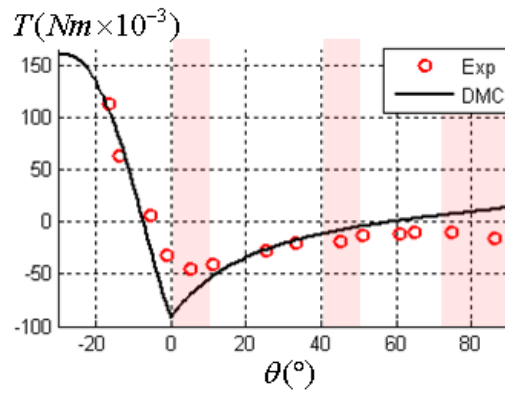
$\theta = 70^\circ$ and $\theta = 90^\circ$. The DMC models offer an effective means to simulate the torques for regions where accurate experimental measurements are difficult.



(a) Iron plane



(b) Iron-iron corner

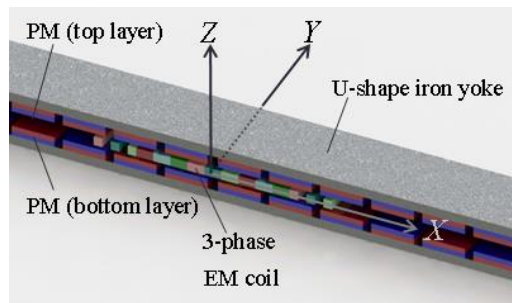


(c) Iron-wood corner

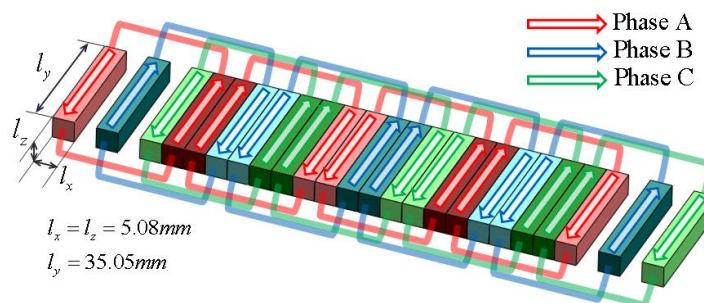
Figure 5-19 Torque comparison of the magnet wheel on an iron bridge

5.4 PM LINEAR SYNCHRONOUS MOTOR (PM-LSynM)

Figure 5-20(a) shows a CAD model of a commercial PM-LSynM with two layers of PMs (top and bottom, each with 26 PMs, or $n_{PM}=52$) and an ironless armature, where the thrust forces are generated on the current-carrying EMs in the presence of stator PM/iron magnetic fields. In the PM-LSynM, the stator has rectangular PMs mounted on the U-shape iron yoke; and the rotor (or forcer) consists of 3-phase ironless EM coil windings as shown in Figure 5-20(b). The DMC modeling method is applied to analyze the PM-LSynM, and identify the PM magnetization and coil positions using the measured air gap flux densities and experimentally obtained force data.



(a) CAD PM-LSynM



(b) 3-phase EM coil

Figure 5-20 CAD PM-LSynM

5.4.1 Identification of PM magnetization

Figure 5-21(a) and (b) shows a CAD model of a PM-LSynM stator with the dimensions of two layers of PMs, and also illustrates the sensor positions $(x, y_{e(k)}, \pm z_e)$ to measure z-directional air-gap flux densities $B_{e(k)+}$ and $B_{e(k)-}$ where $k=1, \dots, 7$ denotes 7 sensor positions on y-axis. The sensor positions and PM geometric parameters are list in Table 5-2.

The PM magnetization is identified by $B_{e(4)+}$ and $B_{e(4)-}$ which are measured nearby the center of PMs. Other measured data is used to evaluate the accuracy of the identified result with a mean square error (MSE):

$$\text{MSE} = \frac{1}{N_{sen}} \sum_{i=1}^{N_{sen}} E_{(k)i}^2 \quad (5.4)$$

where the error is defined by $E_{(k)i} = B_{DMC}(\mathbf{r}_{(k)i}) - B_{e(k)}(\mathbf{r}_{(k)i})$; $\mathbf{r}_{(k)i}$ denotes measured i^{th} position of a k^{th} sensor position measured at $N_{sen} = 4637$ positions; and B_{DMC} is a flux density simulated by a DMC model with the identified result. Figure 5-21(c) and (d) respectively shows $B_{e(4)+}$ and $B_{e(4)-}$ with a threshold value $B_{peak} = 0.34T$ to extract the magnetic field around the peak, \widehat{B}_{e+} and \widehat{B}_{e-} . Since phase differences caused any PM or sensor position error can cause erroneous fitting result, the extracted magnetic fields (\widehat{B}_{e+} and \widehat{B}_{e-} , each with 830 positions, or $n_{sen} = 1660$) are used during the PM identification:

$$\mathbf{b}_e(\mathbf{r}_e) = [\widehat{B}_{e+}(\mathbf{r}_1), \dots, \widehat{B}_{e+}(\mathbf{r}_{n_{sen}/2}), \widehat{B}_{e-}(\mathbf{r}_{n_{sen}/2+1}), \dots, \widehat{B}_{e-}(\mathbf{r}_{n_{sen}})]^T \quad (5.5)$$

where $\mathbf{r}_e = [\mathbf{r}_1, \dots, \mathbf{r}_{n_{sen}}]^T$ denotes the measuring positions of \widehat{B}_{e+} and \widehat{B}_{e-} .

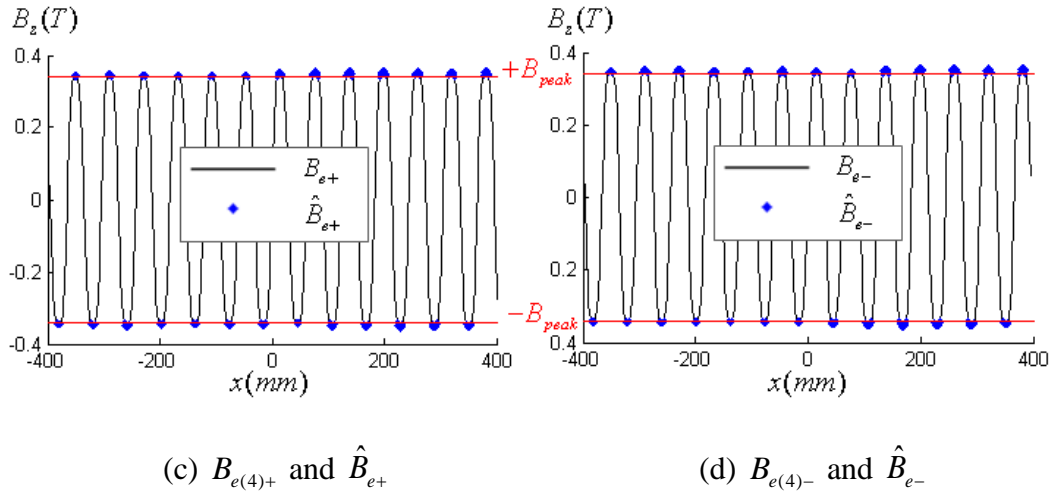
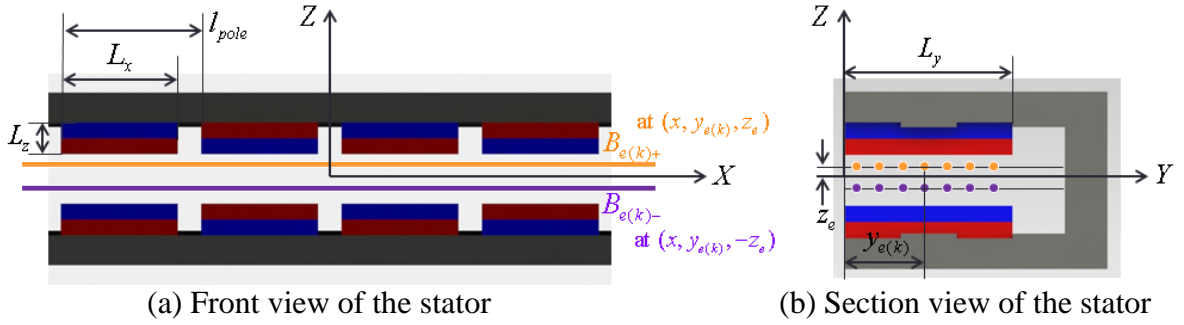


Figure 5-21 Air gap flux density measurement

Table 5-2 PM Geometry and sensor positions measuring air gap flux density

PM Geometry (mm)	sensor positions (mm)
$L_x = 25.4, L_y = 29.97,$ $L_z = 5.84, l_{pole} = 30.48$	$z_e = 2.32, y_{e(k)}$ for sensor index $k = 1, \dots, 7$ $\begin{cases} y_{e(1)} = 2.56, y_{e(2)} = 6.41, y_{e(3)} = 10.27, y_{e(4)} = 14.12, \\ y_{e(5)} = 17.98, y_{e(6)} = 21.83, y_{e(7)} = 25.69 \end{cases}$

A least-square fit of measured air-gap flux density is used to determine unknown PM magnetization $\mu_0 \mathbf{m} = [M_1, \dots, M_k, \dots, M_{n_{PM}}]^T$. When $\bar{B}_k(\mathbf{r}_i)$ denotes the z-directional DMC flux density of k^{th} PM with $\mu_0 M_k = 1T$ on a measuring point \mathbf{r}_i , the z-directional DMC flux density matrix for n_{PM} PMs and n_{sen} measuring point can be defined by

$$\bar{\mathbf{B}}_{PM} = [\bar{\mathbf{b}}_1, \dots, \bar{\mathbf{b}}_k, \dots, \bar{\mathbf{b}}_{n_{PM}}] \quad (5.6)$$

where $\bar{\mathbf{b}}_k = [\bar{B}_k(\mathbf{r}_1), \dots, \bar{B}_k(\mathbf{r}_i), \dots, \bar{B}_k(\mathbf{r}_{n_{sen}})]^T$. Using (5.5), \mathbf{b}_e (5.6) gives a linear relationship between measured data \mathbf{b}_e and unknown \mathbf{m} :

$$\bar{\mathbf{B}}_{PM}(\mu_0 \mathbf{m}) = \mathbf{b}_e \quad (5.7)$$

From (5.7), a linear least-square to determine \mathbf{m} can be solved by a Pseudo-inverse:

$$\mu_0 \mathbf{m} = (\bar{\mathbf{B}}_{PM}^T \bar{\mathbf{B}}_{PM})^{-1} \bar{\mathbf{B}}_{PM}^T \mathbf{b}_e \quad (5.8)$$

As a comparison model for the distributed magnetization $\mu_0 \mathbf{m}$, a linear least-square with an averaged magnetization $\mu_0 m_{avg}$ (in single variable) is determined by (5.9) using

$$\bar{\mathbf{b}}_{PM} = \sum_{k=1}^{n_{PM}} \bar{\mathbf{b}}_k :$$

$$\mu_0 m_{avg} = (\bar{\mathbf{b}}_{PM}^T \bar{\mathbf{b}}_{PM})^{-1} \bar{\mathbf{b}}_{PM}^T \mathbf{b}_e \quad (5.9)$$

The fitted result of \mathbf{m} for top and bottom layers is respectively shown in Figure 5-22(a) and (b) where the values of \mathbf{m} is distributed around the fitting result with single variable m_{avg} .. Using these fitted magnetizations, the flux densities are computed again by the DMC modeling method, and compared in Figure 5-23(a) and (b) with experiment data respective $B_{e(4)\pm}$ measured at $(x, y_{e(4)}, z_e)$ along x-axis; and the error $E_{(4)i}$ with respect to the measured data is plotted in Figure 5-23(c) and (d). While repetitive errors caused by small phase difference exist, the results in Figure 5-23 shows the flux density computed by \mathbf{m} and m_{avg} well matches each other. For all sensor data $k=1, \dots, 7$, flux densities are simulated by the identified PM magnetizations \mathbf{m} and m_{avg} , and tabulated MSE in Table 5-3 gives following results.

- MSE is kept in small values from sensor 2 to sensor 6, although the PM magnetizations are identified by measured data with sensor 4.
- The air-gap flux density of sensor 1 and 7 (respectively located around the sides of PMs) shows some errors; it can be caused by simplified shape (such as neglecting thin slots around PMs) of the iron yoke. Also, the geometry related errors (such as PM position error or bending of top and bottom iron frames by large attraction forces) can be additional reasons of the error.

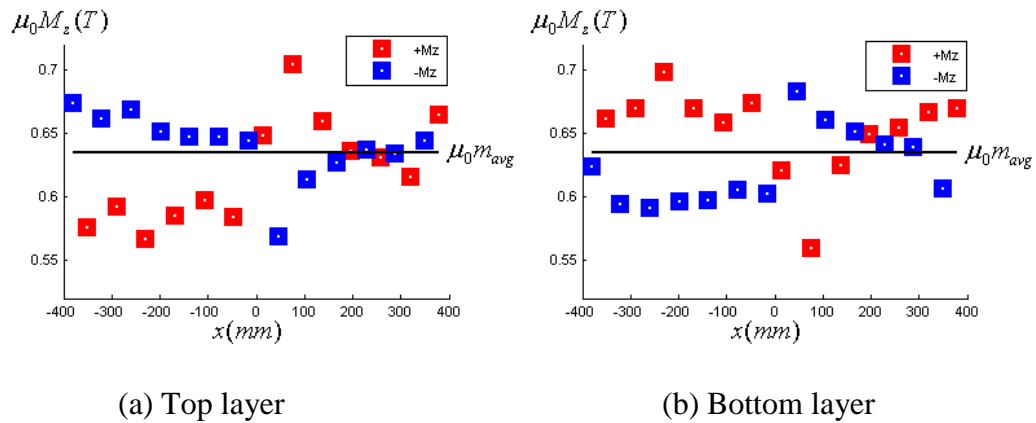
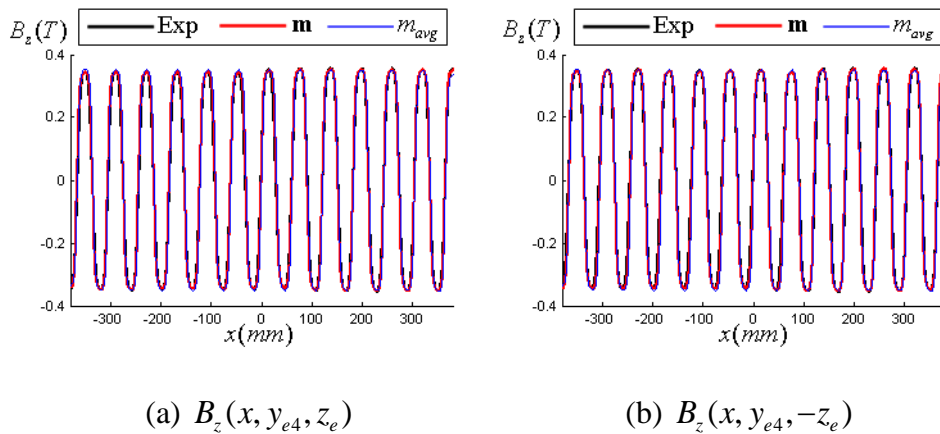
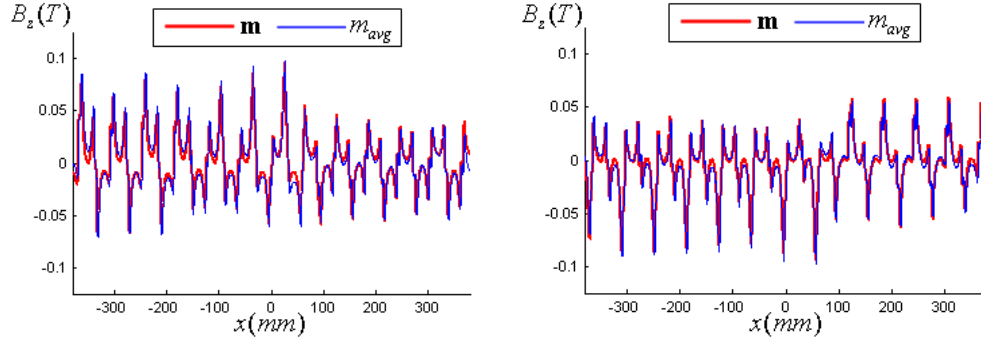


Figure 5-22 Identified magnetizations of PMs





(c) $B_z(x, y_{e4}, z_e)$ error

(d) $B_z(x, y_{e4}, -z_e)$ error

Figure 5-23 Flux density comparison with measured data

Table 5-3 MSE on the flux density of identified PMs

		z	Sensor index k						
			1	2	3	4	5	6	7
MSE	\mathbf{m}	z_e	8.3396	2.9332	2.7339	2.5055	3.0254	2.9546	6.2452
		$-z_e$	6.0148	3.3945	3.2287	2.8175	3.6150	3.7204	8.7206
	m_{avg}	z_e	9.0000	3.3321	3.1044	2.8368	3.4208	3.3537	6.8225
		$-z_e$	6.1325	3.5264	3.4086	2.9754	3.8345	3.9408	9.0304

5.4.2 Identification of EM coil positions

Relatively large force ripple on force experiment data has been observed while ideal rotor design by other simulation gives smooth force output. Such unexpected force ripple can be caused by coil distortion around the end of the rotor where some empty space exists. To investigate the influence of the coil distortion on the force output, actual coil positions are identified by minimizing the error E between the experimentally measured forces F_E and the DMC-based computed forces F :

$$\underset{\mathbf{x}_c}{\text{minimize}} E = \sum_{i=1}^{N_F} |F(x_i, \mathbf{x}_c) - F_E(x_i)|^2 \quad (5.10)$$

where F_E is measured at x_i for N_F rotor positions $i=1, \dots, N_F$; and x_c represents the effective coil positions that will be identified by a least square optimization. To prevent the coil from overlapping each other, the following physical constraints on the variable x_c are imposed:

$$x_c(i+1) - x_c(i) \geq l_x \text{ for } 1 \leq i \leq N_c - 1 \quad (5.11)$$

where $x_c(i)$ denotes i^{th} variable of x_c ; N_c is the number of coil windings to be identified; and l_x is the width of the coil winding along x-axis; and F can be directly evaluated by 3-phase input current with respect to x_i .

To identify the coil positions, $N_c = 24$, $N_F = 7001$ and thrust force actuated by 1A current input are used. Figure 5-24 compares identified coil positions with ideal design; it shows coils have been distorted to empty space around the end of moving part. The computed forces using the identified coil positions closely agree with experiment data as shown in Figure 5-25(a) confirming that the force patterns are much different from the computed forces for an ideal design. The force errors of ideal and identified coils are compared in Figure 5-25(b), and respective MSEs are evaluated by 0.4857 and 0.0438. From the results in Figure 5-25, the force ripple of experimental data is successfully repeated by identified coils.

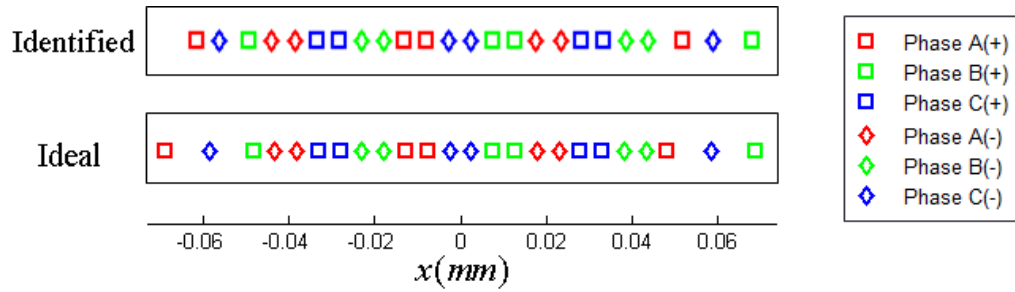


Figure 5-24 Identified coil positions

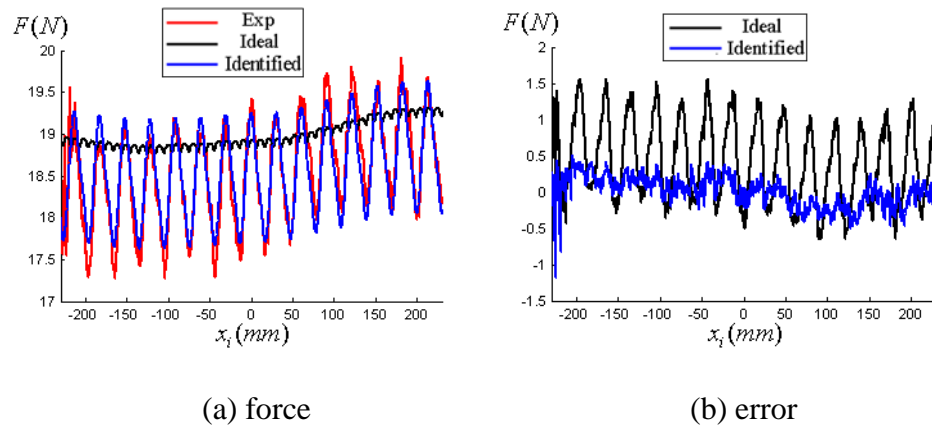


Figure 5-25 Force comparison of the PM-LSynM

5.5 SUMMARY

This chapter has validated the effects of DMC model on the analysis of various practical applications. As a continual research of the DSSM design, one of optimized designs is fabricated to demonstrate the effect of DMC based optimization. Also, existing PMSM orientation stage was analyzed to illustrate the effects of DMC model on analyzing M-DOF motors. For DSSM and spherical orientation stage, simulated results by DMC were validated against experimentally measured flux density and torque.

Besides analyzing electromagnetic actuators, DMC model was used to characterizing stabilizing torque of the magnetic wheel moving on unbounded iron surface. As each of electromagnetic components is modeled separately by DMC, such component-wise system could be effectively analyzed. Since simulated data well agreed with experimentally measured torque, DMC model can help reduce experimental steps on formulating system dynamic. Moreover, unknown system or design parameters could be identified by DMC model based on experimental data. The PM magnetizations and coil positions of PM-LSynM were identified by the minimizing the error between experimental data and DMC simulation. With identified parameters, DMC could offer the accurate model that well represents actual system response of the PM-LSynM.

CHAPTER 6

CONCLUSIONS AND FUTURE WORKS

6.1 CONCLUSIONS

In this thesis, a point-wise electromagnetic source model based on multi-level structured geometry has been presented to offer an efficient means for design analysis and optimization of PM electromechanical actuators from conventional single-axis actuators to M-DOF systems. The following contributions have been made in this thesis research:

- 1) *Magnetic field and force equations in closed form to analyze electromagnetic components and phenomena of electromagnetic actuators consisting of PMs, EMs, iron paths and eddy current.*

The DMC model has provided a direct mean to model electromagnetic components with electric and magnetizing currents on decomposed geometries. Along with closed-form magnetic field and force equations, the DMC models that are represented by a group of local sources have been applied to characterize the effects of PM, EM, iron and eddy current. Its fast and accurate analysis efficiently can facilitate 3D design and analysis of electromagnetic systems.

The advantage of the DMC model controlling computational accuracy and speed of the magnetic field and force has been fully explored for analyzing electromagnetic components and phenomena. The DMC model is validated by published experimental data and analytical solutions for various illustrative applications. For the analysis of

electromagnetic actuators in general 3D designs, the DMC model offers fast computational speed with reasonable accuracy comparing with FEM. Comparing with DMP, the DMC model can improve accuracy with slightly more computational effort. Since the DMC source can be directly determined by the electromagnetic material geometries and properties, computational efficient DMC model has been effectively utilized on formulating topology optimization of M-DOF electromagnetic actuators.

2) *Layout Optimization to determine the best shapes and repetitive patterns of EM and PM to maximize the torque-to-weight ratio of M-DOF electromagnetic actuators.*

Layout Optimization has been developed to determine optimal designs of electromagnetic actuators. Nonlinearity and local convergence problems during optimization of electromagnetic system are avoided by two sequential optimization steps : linear and integer programmings. Linear representations of magnetic field and force equations with respect to DMC volumes and surfaces are used to formulate linear topology optimization. This optimization has been successfully applied for the design of various actuators from conventional single-axis system to M-DOF actuators such as spherical motor and linear-rotary motor. The main contributions of the Layout Optimization can be summarized as follows:

- The Layout Optimization can be easily applied for the design of various applications without knowing the rotor orientation where maximum force/torque occurs. While existing topology optimization by FEM maximizes net flux density at specific rotor orientation to reduce computational cost, the

component-wise modeling method directly maximizes net force/torque average evaluated at various orientations.

- The Layout Optimization offers an efficient mean to determine the optimized design among optimized designs for a number of combinations of EM and PM poles. Rather than solving optimization with rigorous mathematical formulation (often resulted in too complex or unrealizable design), the Layout Optimization focuses on finding practical designs to maximize output performance in a compact design. Overall design cycle of the electromagnetic actuator can be shortend with the simple and systematic Layout Optimization and computationally efficient DMC model.

3) *Experimentally investigating of the effects of DMC model for electromagnetic actuator related applications*

Optimized small DSSM has been fabricated to experimentally investigate the effects of DMC model and its optimization on the torque to weight performance. Simulated results of the DMC based model well represented the optimized rotor design with a Halbach array, which are validated against the measured magnetic field and 3-phase torque output. Also, optimized large DSSM can be fabricated to achieve much higher torque with a thin and flat shape.

An existing 3-DOF PMSM orientation stage which has many PMs and EMs in a 3D space has been modeled by the DMC method. Simulated results were validated by comparing against available experimental data. While the DMC has analyzed the orientation stage as an illustration of M-DOF actuator, general 3D designs of electromagnetic actuators can be effectively analyzed by the DMC model.

Furthermore, component-wise modeling using the DMC method has been used to efficiently simulate the restoring torques of a magnetic wheel moving on unbounded iron surface. The simulated torque around an iron corner was validated against experimentally measured torque. Finally, the DMC model has been applied for identifying unknown design (PM magnetization) or geometry (coil position) parameters using experimental data demonstrating its potentials in many other applications.

6.2 FUTURE WORKS

This research has developed a DMC model in order to provide contributions described above. Further research directions and related a few key research topics are summarized as follows:

1) *Design optimization of various electromagnetic actuators*

While the DMC model has been developed for general 3D electromagnetic driving systems, it is mainly applied for improving existing designs. Using its 3D geometric formulation in closed-form, the DMC model can efficiently help improve performance of many other electromagnetic actuators ranging from conventional single-axis to newly introduced M-DOF designs. Beside such actuator designs, as described on magnet car analysis, component-wise modeling approach can be used to design a part of creative applications such as magnetic levitation bearing for M-DOF actuators and flapping mechanism for flying robot.

2) *Harmonic formulation for current induction*

The DMC model to simulate transient effects of current induction (or eddy current) can be extended to account for frequency response of electromagnetic actuators. Due to the main research interests on analyzing DC or synchronous motors, this research only formulated induction effects in time-domain to show the potential of time varying DMC model. With harmonic formulation for analyzing current induction, energy loss of continuous spinning motor caused by eddy current can be analyzed. Also, induction motor, one of the most popular types, can be efficiently modeled by DMC.

3) *EM and Iron optimization*

Once the layout of EM and PM is optimized by DMC, iron and EM shapes can be topologically optimized to further improve the output performance while minimizing energy loss and weight increases. Since either of moving or stationary part should be non-design space during topology optimization, iterative optimization process is recommended to optimize PM and EM shapes. After optimizing the PM and EM, a nonlinear topology optimization for iron can be formulated by nonlinear constitutive equations of the DMC iron. During the nonlinear optimization, local convergence can be easily occurred by concave property of material permeability μ_i in (A-11); μ_i can be linearized by $\mu_- + \mu_+ = 1$, and then $\mu_0 \mu_i = 2(\mu_- - \mu_+)$.

4) *Parameter identification*

Similar to parameter identification of ironless PMLSM, various inverse problems can be effectively solved by the DMC model; it can be used to calibrate actual magnet and sensor positions or identify unknown system parameters to develop a control or sensing model. Moreover, using error minimization between modeled result and experimental data, topology optimization can be formulated to reconstruct unknown

geometry of electromagnetic components. This will be also effective to other applications related to electromagnetic systems such as brain activity visualization.

APPENDIX A: BC'S OF MAGNETIC MATERIALS

Figure 2-1(c) shows a material boundary formed by two different materials with magnetic permeability μ_+ and μ_- . The continuity condition (2-1a) gives following boundary conditions for magnetic material:

$$B_{n+} = B_{n-} \quad (\text{A.1})$$

$$\frac{B_{t+}}{\mu_+} = \frac{B_{t-}}{\mu_-} \quad (\text{A.2})$$

where tangential continuity of magnetic field intensity is written by flux density using linear magnetic property in (2-2); $\mathbf{B}_\pm = B_{n\pm}\mathbf{n} + B_{t\pm}\mathbf{t}$ are net flux density on each side of boundary; \mathbf{n} and \mathbf{t} are unit surface normal vector \mathbf{n} and tangent vector \mathbf{t} respectively. In the case external magnetic field $\mathbf{B}^e = B_n^e\mathbf{n} + B_t^e\mathbf{t}$ exists on the material boundary, discontinuity of magnetic field intensity can be explained by surface current \mathbf{K}_m that only modifies tangential flux density by:

$$\mathbf{B}_m = \mp \bar{B}_t^e \mathbf{t} \quad (\text{A.3})$$

Substituting tangential net flux density $B_{t\pm} = B_t^e \mp \bar{B}_t^e$ into (A.2) gives the flux density caused by the surface current:

$$\bar{B}_t^e = \left(\frac{\mu_- - \mu_+}{\mu_- + \mu_+} \right) B_t^e \quad (\text{A.4})$$

and then, $B_{t\pm}$ also can be represented by

$$B_{t\pm} = \frac{2\mu_\pm}{(\mu_\mp + \mu_\pm)} B_t^e \quad (\text{A.5})$$

or

$$\mathbf{B}_{\pm} = B_{n\pm} \mathbf{n} + \frac{2\mu_{\pm}}{(\mu_{\mp} + \mu_{\pm})} B_t^e \mathbf{t} \quad (\text{A.6})$$

Using linear magnetic property in (2-2), \mathbf{M} can be expressed by \mathbf{H} :

$$\mathbf{M}_{\pm} = \frac{\mu_{\pm} - \mu_0}{\mu_0} \mathbf{H}_{\pm} \quad (\text{A.7})$$

or

$$\mathbf{M}_{\pm} = \frac{\mu_{\pm} - \mu_0}{\mu_{\pm} \mu_0} \mathbf{B}_{\pm} \quad (\text{A.8})$$

, and applying (A.6) into (A.8) gives a binormal component:

$$\mathbf{n} \times \mathbf{M}_{\pm} = \frac{2}{\mu_0} \frac{\mu_{\pm} - \mu_0}{\mu_{\mp} + \mu_{\pm}} (\mathbf{B}^e \bullet \mathbf{t}) (\mathbf{n} \times \mathbf{t}) \quad (\text{A.9})$$

Since surface current also can be defined by difference between magnetizations of the materials:

$$\mathbf{K}_m = \mathbf{n} \times (\mathbf{M}_+ - \mathbf{M}_-) \quad (\text{A.10})$$

After combining (A.9) and (A.10), surface current flowing at \mathbf{r}_i is described by as a function of tangential component of external field and material permeability

$$\mathbf{K}_i = -\mu_i (\mathbf{B}_{ri}^e \bullet \mathbf{t}_i) \mathbf{b}_i \quad (\text{A.11})$$

where $\mathbf{K}_i = \mathbf{K}_m(\mathbf{r}_i)$ and $\mathbf{B}_{ri}^e = \mathbf{B}^e(\mathbf{r}_i)$; $\mu_i = \frac{2}{\mu_0} \left(\frac{\mu_- - \mu_+}{\mu_- + \mu_+} \right)$ and $\mathbf{b}_i = \mathbf{n}_i \times \mathbf{t}_i$ are defined by

each value or vector at boundary point \mathbf{r}_i . (A.11) implies surface normal component of

\mathbf{K}_i become zero:

$$\mathbf{n}_i \bullet \mathbf{K}_i = 0 \quad (\text{A.12})$$

, its tangential components can be formulated in a matrix form by using coordinate transformation $\mathbf{T}_i = [\mathbf{t}_{i1} \ \mathbf{t}_{i2}]^T$ with orthonormal surface tangential vectors \mathbf{t}_{i1} and \mathbf{t}_{i2} :

$$\mathbf{T}_i [\mathbf{n}_i]_{\times} \mathbf{T}_i^T \mathbf{K}_{i*} = \mu_i \mathbf{T}_i \mathbf{B}_{ri} \quad (\text{A.13})$$

where $\mathbf{K}_{i*} = \mathbf{T}_i \mathbf{K}_i$ reduces unknowns components of surface current into 2.

APPENDIX B: PM DESIGN VARIABLE

The PM magnetization of (i)th volume in the decomposed rotor design spaces can be parameterized by $\mathbf{M}_{(i)}$ using its material density vector $\boldsymbol{\rho}_{(i)}$. For the formulation of the linear constraints later, design variable $\bar{\boldsymbol{\rho}}_{(i)}$ is defined by 6 positive material density variables in the local xyz coordinate system:

$$\bar{\boldsymbol{\rho}}_{(i)} = \begin{bmatrix} \bar{\boldsymbol{\rho}}_{(i)+} \\ \bar{\boldsymbol{\rho}}_{(i)-} \end{bmatrix} \quad (\text{B.1})$$

where $\bar{\boldsymbol{\rho}}_{(i)\pm} = [\rho_{(i)x\pm} \quad \rho_{(i)y\pm} \quad \rho_{(i)z\pm}]^T$ and $0 \leq \rho_{(i)x\pm}, \rho_{(i)y\pm}, \rho_{(i)z\pm} \leq 1$. Then, its material density vector $\boldsymbol{\rho}_{(i)}$ is given by

$$\boldsymbol{\rho}_{(i)} = \bar{\mathbf{I}}_{\rho} \bar{\boldsymbol{\rho}}_{(i)} \quad (\text{B.2})$$

where using 3×3 identity matrix \mathbf{I}_3 , 3×6 matrix $\bar{\mathbf{I}}_{\rho} = [\mathbf{I}_3, -\mathbf{I}_3]$ converts 6 density variables into 3 components vector. The PM magnetization vector $\mathbf{M}_{(i)}$ in the xyz local coordinate is described by the maximum magnetization of the rotor M_{\max} and density vector $\boldsymbol{\rho}_{(i)}$:

$$\mathbf{M}_{(i)} = M_{\max} \boldsymbol{\rho}_{(i)} \quad (\text{B.3})$$

or design variable $\bar{\boldsymbol{\rho}}_{(i)}$ in (B.2):

$$\mathbf{M}_{(i)} = M_{\max} \bar{\mathbf{I}}_{\rho} \bar{\boldsymbol{\rho}}_{(i)}. \quad (\text{B.4})$$

At an orientation p of the PM volume, Figure B-1 shows the coordinate transform of the $\mathbf{M}_{(i)}$ in the local xyz coordinate into $\mathbf{M}_{p(i)}$ in the global XYZ coordinate system at an orientation p of the PM volume by transformation matrix $\bar{\mathbf{G}}_{p(i)} = [\mathbf{e}_{p(i)x} \quad \mathbf{e}_{p(i)y} \quad \mathbf{e}_{p(i)z}]$; a matrix representation of $\mathbf{M}_{p(i)}$ in terms of the $\bar{\mathbf{p}}_{(i)}$ is given by

$$\mathbf{M}_{p(i)} = M_{\max} \bar{\mathbf{G}}_{(i)} \bar{\mathbf{I}}_{\rho} \bar{\mathbf{p}}_{(i)}. \quad (\text{B.5})$$

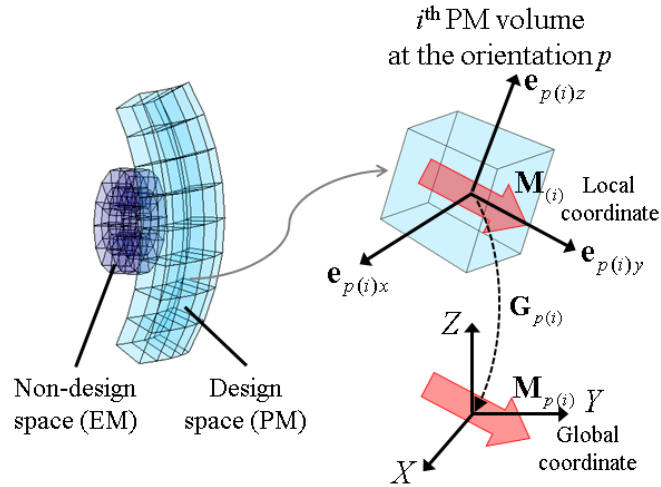


Figure B-1 Definition of a PM design variable

REFERENCES

- [1] K.-M. Lee and H. Son, "Distributed Multipole Model for Design of Permanent-Magnet-Based Actuators," *Magnetics, IEEE Transactions on*, vol. 43, pp. 3904-3913, 2007.
- [2] K.-M. Lee, H. Son, and J. Joni, "Concept Development and Design of a Spherical Wheel Motor (SWM)," in *Robotics and Automation, 2005. ICRA 2005. Proceedings of the 2005 IEEE International Conference on*, 2005, pp. 3652-3657.
- [3] H. Son and K.-M. Lee, "Distributed Multipole Models for Design and Control of PM Actuators and Sensors," *Mechatronics, IEEE/ASME Transactions on*, vol. 13, pp. 228-238, 2008.
- [4] L. Yan, I. M. Chen, C. K. Lim, G. Yang, W. Lin, and K.-M. Lee, "Design and analysis of a permanent magnet spherical actuator," *IEEE/ASME Transactions on Mechatronics*, vol. 13, pp. 239-248, 2008.
- [5] W. Wang, J. Wang, G. W. Jewell, and D. Howe, "Design and control of a novel spherical permanent magnet actuator with three degrees of freedom," *IEEE/ASME Transactions on Mechatronics*, vol. 8, pp. 457-468, 2003.
- [6] J. Wang, G. W. Jewell, and D. Howe, "A general framework for the analysis and design of tubular linear permanent magnet machines," *IEEE Transactions on Magnetics*, vol. 35, pp. 1986-2000, 1999.
- [7] O. C. Zienkiewicz, P. L. Arlett, and A. K. Bahrani, "Solution of three-dimensional field problems by the finite element method," *The Engineer*, vol. 224, p. 550, 1967.
- [8] A. K. Chargin and C. D. Henning, "Magnetic field and force by finite element techniques," *California Univ., Livermore. Lawrence Radiation Lab.* 1969.
- [9] B. H. McDonald and A. Wexler, "Finite-Element Solution of Unbounded Field Problems," *IEEE Transactions on Microwave Theory and Techniques*, vol. 20, pp. 841-847, 1972.
- [10] A. Wexler, "Some recent developments in field calculations," *IEEE Transactions on Magnetics*, vol. 15, pp. 1659-1664, 1979.
- [11] M. Lean and A. Wexler, "Accurate field computation with the boundary element method," *IEEE Transactions on Magnetics*, vol. 18, pp. 331-335, 1982.

- [12] J. H. Collins and P. Daly, "Calculations for Guided Electromagnetic Waves using Finite-difference Methods†," *International Journal of Electronics*, vol. 14, pp. 361-380, 1963.
- [13] Z. Cendes and D. Shenton, "Adaptive mesh refinement in the finite element computation of magnetic fields," *IEEE Transactions on Magnetics*, vol. 21, pp. 1811-1816, 1985.
- [14] M. J. Berger and P. Colella, "Local adaptive mesh refinement for shock hydrodynamics," *Journal of Computational Physics*, vol. 82, pp. 64-84, 1989.
- [15] V. Cingoski, N. Miyamoto, and H. Yamashita, "Element-free Galerkin method for electromagnetic field computations," *IEEE Transactions on Magnetics*, vol. 34, pp. 3236-3239, 1998.
- [16] Q. Li and K.-M. Lee, "An Adaptive Meshless Method for Magnetic Field Computation," *IEEE Transactions on Magnetics*, vol. 42, pp. 1996-2003, 2006.
- [17] E. D. T. De Lacheisserie, D. Gignoux, and M. Schlenker, *Magnetism: Fundamentals* vol. 1: Springer Verlag, 2005.
- [18] D. J. Craik, "Magnetostatics of axially symmetric structures," *Journal of Physics D: Applied Physics*, vol. 7, p. 1566, 1974.
- [19] S. Nedelcu and J. H. P. Watson, "Magnetic dipole model of a permanent magnet based device," *Journal of Physics D: Applied Physics*, vol. 34, p. 2622, 2001.
- [20] P. De Visschere, "An exact two-dimensional model for a periodic circular array of head-to-head permanent magnets," *Journal of Physics D: Applied Physics*, vol. 38, p. 355, 2005.
- [21] T. Kabashima, A. Kawahara, and T. Goto, "Force calculation using magnetizing currents," *IEEE Transactions on Magnetics*, vol. 24, pp. 451-454, 1988.
- [22] G. Henneberger, P. K. Sattler, and D. Shen, "Nature of the equivalent magnetizing current for the force calculation," *IEEE Transactions on Magnetics*, vol. 28, pp. 1068-1071, 1992.
- [23] H. S. Lopez, F. Liu, M. Poole, and S. Crozier, "Equivalent Magnetization Current Method Applied to the Design of Gradient Coils for Magnetic Resonance Imaging," *IEEE Transactions on Magnetics*, vol. 45, pp. 767-775, 2009.
- [24] L. Greengard and V. Rokhlin, "A fast algorithm for particle simulations* 1," *Journal of Computational Physics*, vol. 73, pp. 325-348, 1987.

- [25] V. Rokhlin, "Rapid solution of integral equations of scattering theory in two dimensions," *Journal of Computational Physics*, vol. 86, pp. 414-439, 1990.
- [26] E. Darve, "The fast multipole method: numerical implementation," *Journal of Computational Physics*, vol. 160, pp. 195-240, 2000.
- [27] K.-M. Lee, K. Bai, and J. Lim, "Dipole Models for Forward/Inverse Torque Computation of a Spherical Motor," *IEEE/ASME Transactions on Mechatronics*, vol. 14, pp. 46-54, 2009.
- [28] H. Son, K. Bai, J. Lim, and K.-M. Lee, "Design of multi-DOF electromagnetic actuators using distributed multipole models and image method," *International Journal of Applied Electromagnetics and Mechanics*, vol. 34, pp. 195-210, 2010.
- [29] R. Erlandsson and L. Olsson, "A three axis micropositioner for ultrahigh vacuum use based on the inertial slider principle," *Review of Scientific Instruments*, vol. 67, pp. 1472-1474, 1996.
- [30] S. H. Chang, C. K. Tseng, and H. C. Chien, "An ultra-precision XY&thetas_z piezo-micropositioner. I. Design and analysis," *IEEE Transactions on Ultrasonics, Ferroelectrics and Frequency Control*, vol. 46, pp. 897-905, 1999.
- [31] S. Toyama, S. Hatae, and M. Nonaka, "Development of multi-degree of freedom spherical ultrasonic motor," in *Fifth International Conference on Advanced Robotics, 'Robots in Unstructured Environments', 91 ICAR.* , 1991, pp. 55-60 vol.1.
- [32] T. Amano, T. Ishii, K. Nakamura, and S. Ueha, "An ultrasonic actuator with multidegree of freedom using bending and longitudinal vibrations of a single stator," in *Proceedings of IEEE Ultrasonics Symposium*, 1998, pp. 667-670 vol.1.
- [33] T. Mashimo and S. Toyama, "Rotary-linear piezoelectric actuator using a single stator," *IEEE Transactions on Ultrasonics, Ferroelectrics and Frequency Control*, vol. 56, pp. 114-120, 2009.
- [34] T. Mashimo, S. Toyama, and H. Ishida, "Design and implementation of spherical ultrasonic motor," *IEEE Transactions on Ultrasonics, Ferroelectrics and Frequency Control*, vol. 56, pp. 2514-2521, 2009.
- [35] L. Bo, M. Aoyagi, H. Tamura, and T. Takano, "Development of a novel rotor-embedded-type multidegree-of-freedom spherical ultrasonic motor," in *Mechatronics and Automation (ICMA)*, 2011 International Conference on, 2011, pp. 795-800.
- [36] D. L. Trumper, "Magnetic suspension techniques for precision motion control," *Massachusetts Institute of Technology*, 1990.

- [37] W. J. Kim, D. L. Trumper, and J. H. Lang, "Modeling and vector control of planar magnetic levitator," *IEEE Transactions on Industry Applications*, vol. 34, pp. 1254-1262, 1998.
- [38] I. J. C. Compter, "Electro-dynamic planar motor," *Precision Engineering*, vol. 28, pp. 171-180, 2004.
- [39] J. W. Jansen, C. M. M. van Lierop, E. A. Lomonova, and A. J. A. Vandenput, "Magnetically levitated planar actuator with moving magnets," *IEEE Transactions on Industry Applications*, vol. 44, pp. 1108-1115, 2008.
- [40] G. Krebs, A. Tounzi, B. Pauwels, D. Willemot, and F. Piriou, "Modeling of A Linear and Rotary Permanent Magnet Actuator," *IEEE Transactions on Magnetics*, vol. 44, pp. 4357-4360, 2008.
- [41] P. Bolognesi, O. Bruno, F. Papini, V. Biagini, and L. Taponecco, "A low-complexity rotary-linear motor useable for actuation of active wheels," in *International Symposium on Power Electronics Electrical Drives Automation and Motion (SPEEDAM) 2010*, pp. 331-338.
- [42] F. C. Williams, E. R. Laithwaite, and L. S. Piggott, "Brushless variable-speed induction motors," *Proceedings of the IEE-Part A: Power Engineering*, vol. 104, pp. 102-118, 1957.
- [43] K. Davey, G. Vachtsevanos, and R. Powers, "The analysis of fields and torques in spherical induction motors," *IEEE Transactions on Magnetics*, vol. 23, pp. 273-282, 1987.
- [44] A. Foggia, E. Olivier, and F. Chappuis, "New three degrees of freedom electromagnetic actuator," in *Conference record—IAS annual meeting, Vol. 35*, New York, 1988, pp. 137-141 vol. 1.
- [45] R. L. Hollis, S. E. Salcudean, and A. P. Allan, "A six-degree-of-freedom magnetically levitated variable compliance fine-motion wrist: design, modeling, and control," *IEEE Transactions on Robotics and Automation*, vol. 7, pp. 320-332, 1991.
- [46] K.-M. Lee, G. Vachtsevanos, and C. Kwan, "Development of a spherical stepper wrist motor," in *Proceedings of IEEE International Conference on Robotics and Automation*, 1988, pp. 267-272 vol.1.
- [47] K.-M. Lee and C.-K. Kwan, "Design concept development of a spherical stepper for robotic applications," *IEEE Transactions on Robotics and Automation*, vol. 7, pp. 175-181, 1991.

- [48] J. Wang, G. W. Jewell, and D. Howe, "Modelling of a novel spherical permanent magnet actuator," in Proceedings of IEEE International Conference on Robotics and Automation, 1997, pp. 1190-1195 vol.2.
- [49] J. Wang, K. Mitchell, G. W. Jewell, and D. Howe, "Multi-degree-of-freedom spherical permanent magnet motors," in Proceedings of IEEE International Conference on Robotics and Automation, 2001, pp. 1798-1805 vol.2.
- [50] L. Yan, I. M. Chen, C. K. Lim, G. Yang, W. Lin, and K.-M. Lee, "Experimental Investigation on the Magnetic Field of a Permanent Magnet Spherical Actuator," in Proceedings of IEEE/ASME International Conference on Advanced Intelligent Mechatronics, 2005, pp. 347-352.
- [51] K. I. Laskaris and A. G. Kladas, "Permanent-Magnet Shape Optimization Effects on Synchronous Motor Performance," IEEE Transactions on Industrial Electronics, vol. 58, pp. 3776-3783, 2011.
- [52] Y. Perriard, P. Ragot, and M. Markovic, "Brushless DC Motor Optimization Process - Choice between Standard or Straight Tooth Shape," in Conference Record of the 2006 IEEE Industry Applications. 41st IAS Annual Meeting, 2006, pp. 1898-1904.
- [53] J. L. G. Janssen, J. J. H. Paulides, E. A. Lomonova, and A. J. A. Vandenput, "Cogging Force Reduction in Tubular Permanent Magnet Actuators," in Electric Machines & Drives Conference, 2007. IEMDC '07. IEEE International, 2007, pp. 266-271.
- [54] D. N. Dyck, D. A. Lowther, and E. M. Freeman, "A method of computing the sensitivity of electromagnetic quantities to changes in materials and sources," IEEE Transactions on Magnetics, vol. 30, pp. 3415-3418, 1994.
- [55] D. N. Dyck and D. A. Lowther, "Automated design of magnetic devices by optimizing material distribution," IEEE Transactions on Magnetics, vol. 32, pp. 1188-1193, 1996.
- [56] T. Labbe and B. Dehez, "Convexity-Oriented Mapping Method for the Topology Optimization of Electromagnetic Devices Composed of Iron and Coils," IEEE Transactions on Magnetics, vol. 46, pp. 1177-1185, 2010.
- [57] T. Labbe and B. Dehez, "Convexity-Oriented Method for the Topology Optimization of Ferromagnetic Moving Parts in Electromagnetic Actuators Using Magnetic Energy," IEEE Transactions on Magnetics, vol. 46, pp. 4016-4022, 2010.
- [58] Y. Okamoto, M. Ohtake, and N. Takahashi, "Magnetic shield design of perpendicular magnetic recording head by using topology optimization technique," IEEE Transactions on Magnetics, vol. 41, pp. 1788-1791, 2005.

- [59] Y. Okamoto, K. Akiyama, and N. Takahashi, "3-D topology optimization of single-pole-type head by using design sensitivity analysis," *IEEE Transactions on Magnetics*, vol. 42, pp. 1087-1090, 2006.
- [60] S.-I. Park, S. Min, S. Yamasaki, S. Nishiwaki, and J. Yoo, "Magnetic Actuator Design Using Level Set Based Topology Optimization," *IEEE Transactions on Magnetics*, vol. 44, pp. 4037-4040, 2008.
- [61] S. Lim, T. Yamada, S. Min, and S. Nishiwaki, "Topology Optimization of a Magnetic Actuator Based on a Level Set and Phase-Field Approach," *IEEE Transactions on Magnetics*, vol. 47, pp. 1318-1321, 2011.
- [62] H. A. Haus and J. R. Melcher, *Electromagnetic fields and energy*: Prentice Hall Englewood Cliffs, New Jersey, 1989.
- [63] N. Ida and J. P. A. Bastos. Forces in Permanent Magnets Team Workshop Problem 23.
- [64] H. Karl, J. Fetzer, S. Kurz, G. Lehner, and W. M. Rucker. Description of TEAM Workshop Problem 28: An Electrodynamics Levitation Device.
- [65] K. J. M. Inc. The Original K&J Magnet Calculator.
www.kjmagnetics.com/calculator.asp.
- [66] K. Bai and K.-M. Lee, "Direct Field-feedback Control of a Ball-joint-like Permanent-magnet Spherical Motor," *IEEE/ASME Trans. on Mechatronics* DOI: 10.1109/TMECH.2013.2264565, Published 12 June 2013 (12 pages).
- [67] K. Sitapati and R. Krishnan, "Performance comparisons of radial and axial field, permanent-magnet, brushless machines," *Industry Applications*, *IEEE Transactions on*, vol. 37, pp. 1219-1226, 2001.
- [68] M. Aydin, S. Huang, and T. A. Lipo, "Design, Analysis, and Control of a Hybrid Field-Controlled Axial-Flux Permanent-Magnet Motor," *Industrial Electronics*, *IEEE Transactions on*, vol. 57, pp. 78-87, 2010.
- [69] J. Ji, K.-M. Lee, and D. Wang, "Real-time Computational Model for Visualizing Compliant Beam Motion of a Flexible Mobile-sensing Node" submitted to AIM2014.
- [70] K.-M. Lee and S. Arjunan, "A Three-DOF Micro-motion In-Parallel Actuated Manipulator," *IEEE Trans. on Robotics and Automation*. vol. 7, no. 5, pp. 634-641, October 1991.